MOLECULAR SIGNALING AND EPIGENETIC MECHANISMS FOR OSTEOBLAST PROGENITOR MAINTENANCE DURING BONE REGENERATION AND DEVELOPMENT

by

GABRIEL ALEXANDER YETTE

A DISSERTATION

Presented to the Department of Biology
and the Graduate School of the University of Oregon
in partial fulfillment of the requirements
for the degree of
Doctor of Philosophy

December 2019

DISSERTATION APPROVAL PAGE

Student: Gabriel Alexander Yette

Title: Molecular Signaling and Epigenetic Mechanisms for Osteoblast Progenitor Maintenance During Bone Regeneration and Development

This dissertation has been accepted and approved in partial fulfillment of the requirements for the Doctor of Philosophy degree in the Department of Biology by:

Dr. Eric Selker	Chairperson
Dr. Kryn Stankunas	Advisor
Dr. Christopher Doe	Core Member
Dr. John Postlethwait	Core Member
Dr. Bradley Nolen	Institutional Representative

and

Kate Mondloch	Interim Vice Provost and Dean of the Graduate School

Original approval signatures are on file with the University of Oregon Graduate School.

Degree awarded December 2019

DISSERTATION ABSTRACT

Gabriel Alexander Yette

Doctor of Philosophy

Department of Biology

December 2019

Title: Molecular Signaling and Epigenetic Mechanisms for Osteoblast Progenitor
Maintenance During Bone Regeneration and Development

Severe bone ailments and fractures often surpass the innate repair capabilities of humans, frequently necessitating painful, costly and imperfect surgical interventions. Understanding mechanisms that promote bone repair and remodeling would enable innovative therapeutic approaches. Zebrafish have the innate ability to robustly and repeatedly regenerate bones by re-activating developmental pathways in mature cells. Understanding how zebrafish achieve this feat could provide clues how to unlock similar restorative properties in humans. Key questions remain including how the fin always regains its pre-injured shape and how mature cells reprogram gene expression profiles to return to and then maintain progenitor states to enable regeneration.

Wnt ligands keep developmental pathways active including by maintaining bone

cell progenitor states until regeneration ends. Inhibiting the Wnt pathway rapidly and irreversibly halts regeneration, hinting that Wnt cessation could naturally signal the end of regeneration. We identified a Wnt source of specialized cells we term the regenerative niche at the distal end of the regenerating fin. The niche gradually depletes during regeneration, likely explaining how regeneration slows and then stops. With this information, we generated a mathematical model predicting regenerating fin length dependent on initial niche size and perdurance.

Chromatin landscapes including histone modifications influence gene expression during development. It is becoming increasingly evident they also play crucial roles during regeneration. An initial publication ten years ago implicated dynamic tri-methylation of lysine 27 of histone H3 (H3K27me3), a modification associated with gene repression, during regeneration. H3K27me3 is deposited by the Polycomb Repressive Complex 2 (PRC2) and removed by Kdm6 demethylases. More recent studies found PRC2 is required for reprograming cardiomyocytes during heart regeneration. However, PRC2 function during bone regeneration has not been investigated. We made CRISPR mutants of *ezh2* and *ezh1,* the methyltransferase components of PRC2, and used a newly identified *ezh2* hypomorph allele to investigate PRC2 during bone development and

regeneration. We found PRC2 promotes osteoblast progenitor maintenance, skeletal patterning and cell fate decisions. Pilot studies described herein suggest PRC2 may fulfill similar roles during regeneration.

Our findings provide valuable insights how cell organizing centers, cell allocation and cell state establishment and maintenance contribute to organ composition, size, and shape.

CURRICULUM VITAE

NAME OF AUTHOR: Gabriel Alexander Yette

GRADUATE AND UNDERGRADUATE SCHOOLS ATTENDED:

University of Oregon, Eugene
Colorado College, Colorado Springs

DEGREES AWARDED:

Doctor of Philosophy, Biology, 2019, University of Oregon
Bachelor of Arts, Biology, 2009, Colorado College

AREAS OF SPECIAL INTEREST:

Molecular, Cell, and Developmental Biology

Epigenetics

Genetics

Gene Regulation

Organogenesis and Regeneration

PROFESSIONAL EXPERIENCE:

Professional Research Assistant, University of Colorado-Anschutz Medical Campus, November 2010 – August 2013

GRANTS, AWARDS, AND HONORS:

Ruth L. Kirschstein National Research Service Award (NRSA) Fellowship (F31), National Institute of Health, 2017-2019

Women in Graduate Science Ally Award, University of Oregon, 2019

Pete von Hippel Graduate Scholar Award, Institute of Molecular Biology, University of Oregon, 2018

Donald E. Wimber Travel Award, University of Oregon, 2018

Peter O’Day Fellowship, University of Oregon, 2017

Developmental Biology Training Grant, University of Oregon, 2015-2017

Best Poster Award, Institute of Molecular Biology, University of Oregon, 2016

Travel Award, Institute of Molecular Biology, University of Oregon, 2015

Genetics Training Grant, University of Oregon, 2014-2015

PUBLICATIONS:

Stewart, S.*, **Yette, G. A.***, Henner, A. L., Bleu, H. K., Braunstein, J. A., Chehab, J. W., … Stankunas, K. (2019). Skeletal geometry and niche transitions restore organ size and shape during zebrafish fin regeneration. *bioRxiv*, 606970 *Equal contributions

Stewart, S., Le Bleu, H.K., **Yette, G.A**., Henner, A.L., Braunstein J.A., and Stankunas, K. (2019). *longfin* causes cis-ectopic expression of the *kcnh2a* ether-a-go-go K+ channel to autonomously prolong fin outgrowth. *bioRxiv*, 790329

Zhao, J., Giles, B. M., Taylor, R. L., **Yette, G. A.**, Lough, K. M., Ng, H. L., ... & Boackle, S. A. (2016). Preferential association of a functional variant in complement receptor 2 with antibodies to double-stranded DNA. Ann Rheum Dis. 75:242-52. PMCID: PMC4717392.

Yette, G.A., Stewart, S., and Stankunas, K. Ezh2 promotes osteoblast generation, expansion and skeletal patterning during zebrafish development. In preparation.

ACKNOWLEDGMENTS

I would like to thank my Ph.D. advisor, Dr. Kryn Stankunas for his guidance, advice, and his support. He gave me confidence and pushed me to be critical of my own work and to be a better scientist. I will miss our discussions. I would like to thank Dr. Scott Stewart for his mentorship as well. He is knowledgeable in a breadth of subjects and was a valuable resource. He and Kryn complemented each other well and provided me with the best possible training. Thank you to my Dissertation Committee (Drs. Eric Selker, John Postlethwait, Chris Doe, and Brad Nolen) and Dr. Chuck Kimmel and Dr. Jamie Nichols for your input, guidance, and support. I would also like to acknowledge the other graduate students in my cohort. Thank you for suffering through the first year of graduate school with me. Past Stankunas lab grad students, Drs. Brynn Akerberg, Kate Karfilis, Fern Bosada, Alex Akerberg and Ben Armstrong- Thank you for showing me what it takes to finish graduate school and sharing in all the good times over the years. Current Stankunas lab grad students, Amy Robbins and Heather Le Bleu- I had fun sharing the lab with you and I hope I was helpful. Astra Henner, thank you for being ever present and a model community member. Joshua Braunstein and Diana Nguyen, it was a lot of fun to see you develop as people and scientists. I look forward to seeing what all you will accomplish.

I need to thank my parents, Rebecca and Harold, and my sisters, Emily and Lillian, for instilling lifelong lessons and their continued love and support… and humbling me when necessary. I would not be who I am or where I am today without you. Thank you to my wife, Melissa Mares, for supporting me these past 8 years of life. You are amazing. Marley, you are the best companion animal that I could have hoped for.

Lastly, I would like to thank the rec sports teams I played on (Specific Heat, Narnia Tattoo Barbecue, Hot Rod, Kickaroos and Hits for Brains) and Crossfit Intensify for clearing my mind of grad school concerns. Also, thank you zebrafish.

The research presented in Chapters II, Chapter III and Chapter IV was supported by an institute funded positions of a National Institute of Health (NIH) T32 training grants (G.A.Y.), an NIH Ruth L. Kirschstein National Research Service Award (F31AR071283, G.A.Y.), and additional NIH support (1R01GM127761 (K.S. and S.S.) and 5R03AR067522 (S.S.))

Dedicated to my parents, Rebecca and Harold Yette. Thank you

TABLE OF CONTENTS

Chapter Page

Chapter Page

LIST OF FIGURES

Figure Page

Figure Page

SUPPLEMENTAL MATERIAL

Figure Page

LIST OF TABLES

CHAPTER I

INTRODUCTION

Bone ailments due to age, genetic perturbations, environment or damage are costly and debilitating. Humans repair minor bone damage fairly well, but more severe cases require surgical intervention followed by months to years of rehabilitating. Even then, bones can remain disfigured, less sturdy than before and leave patients in lifelong pain and discomfort. Imbalances of bone resorption and replacement lead to weak, brittle bones, such is the case with osteoporosis. On the other hand, osteopetrosis causes abnormally dense and brittle bones. Osteopetrosis can also have secondary effects such as decreased red blood cell production due to bone marrow cavities filling with excess bone. These ailments would greatly benefit from targeted treatments developed based on a greater understanding how bone is developed, repaired and remodeled.

Zebrafish have the extraordinary ability to regenerate multiple tissues including their appendage homologous fins (Gemberling, Bailey, Hyde, & Poss, 2013; Nakamura, Gehrke, Lemberg, Szymaszek, & Shubin, 2016). Zebrafish possess evolutionarily conserved bone development pathways amenable to genetic and chemical genetic perturbation. Furthermore, transparent developing larvae and adult fins allow for easy observation of bone remodeling events. Taken together, zebrafish is an ideal model organism for investigating bone growth and regeneration.

Zebrafish fins remarkably regenerate to the original shape and size even after multiple amputations (Azevedo, Grotek, Jacinto, Weidinger, & Saúde, 2011). Lineage tracing experiments showed new caudal fin tissue derives from partial de-differentiation of individual cell types remaining at the amputation site (Knopf et al., 2011; Sousa et al., 2011; Stewart & Stankunas, 2012; Tu & Johnson, 2011). For example, damage causes mature bone-producing osteoblasts to de-differentiate by turning off mature genes and re-activating developmental genes to become progenitor osteoblasts. De-differentiated osteoblasts are maintained in a proliferative progenitor state by Wnt ligands (Stewart, Gomez, Armstrong, Henner, & Stankunas, 2014; Stoick-Cooper et al., 2007; Wehner et al., 2014). A coordinated balance of Wnt and BMP signaling promotes progenitor and differentiated osteoblast states to reform the lost tissue (Stewart et al., 2014). Strikingly, when Wnt signaling is inhibited during regeneration, osteoblast progenitors progress to a mature state and regeneration ceases (Stewart et al., 2014). This highlights the importance of Wnt signaling for bone regeneration, and potentially linking the cessation of regeneration to progressive Wnt ligand depletion. Yet questions remain about: 1) the Wnt source, 2) how the fin “knows” when to stop regenerating to recapture the appropriate shape and size and 3) how osteoblasts change their gene expression programs to transition between differentiated and progenitor states.

Osteoblasts must change their genetic expression profile to de-differentiate, proliferate and re-differentiate back into bone-producing osteoblasts. A potential mode for transcriptional change is dynamic changes of histone modifications and chromatin landscapes. One such modification, tri-methylation of lysine 27 of histone H3 (H3K27me3) is associated with gene repression. H3K27me3 was previously implicated during fin regeneration as evident by injury-induced upregulation of its demethylase, Kdm6bb (Stewart, Tsun, & Belmonte, 2009). Kdm6bb removes H3K27me3 to activate silenced genes (Cloos, Christensen, Agger, & Helin, 2008). Conversely, H3K27me3 is deposited by Polycomb Repressive Complex 2 (PRC2) through its methyltransferase components Ezh1 or Ezh2 (Raphaël Margueron & Reinberg, 2011). A recent study investigating zebrafish heart regeneration showed H3K27me3 deposition was important for reprograming cardiomyocytes to facilitate regeneration (Ben-Yair et al., 2019). In addition, neonatal mice, which also have the capacity to regenerate their hearts, failed to recuperate lost tissue when PRC2 function was disrupted (Ai et al., 2017). Yet, PRC2 and more specifically, Ezh1 and Ezh2, have not been thoroughly investigated during caudal fin bone regeneration.

The material presented in Chapter II describes a molecular marker for a Wnt-producing niche during regeneration. We used this marker to monitor niche generation and depletion throughout regeneration. These observations led us to a new model with mathematical support explaining how regenerating appendages reach the same shape and size as they were before incurring damage. Chapter III summarizes roles of PRC2 during cell specification, organogenesis, axial skeleton patterning, and osteoblast progenitor maintenance. We generated *ezh2* and *ezh1* mutants using CRISPR/Cas9 and characterized phenotypes in animals with all possible genetic combinations. Our studies refute published work describing *ezh1* roles during zebrafish development. We also clarified the status of an *ezh2* hypomorph allele and used it to investigate roles of maternal Ezh2 during early developmental stages and skeletal patterning. Finally, Chapter III shows PRC2 promotes progenitor characteristics in osteoblasts during development. Chapter IV outlines pioneering work investigating PRC2 during bone regeneration. The findings in this chapter suggest that PRC2/H3K27me3 enables robust fin regeneration by maintaining cell fates and states.

CHAPTER II

SKELETAL GEOMETRY AND NICHE TRANSITIONS RESTORE ORGAN SIZE AND SHAPE DURING ZEBRAFISH FIN REGENERATION

JOURNAL STYLE INFORMATION

Scott Stewart, Gabriel A. Yette, Heather K. Le Bleu, Astra L. Henner, Joshua A. Braunstein, Jad W. Chehab, Michael J. Harms and Kryn Stankunas. In Review. Copyright 2019

AUTHOR CONTRIBUTIONS

S. S., G. A. Y., H. K. L. and K. S. designed experiments. S.S., G. A. Y., H. K. L., A. L. H., J. A. B., and J. C. performed experiments. K. S. and M. J. H. led the mathematical modeling. K. S. and S. S. prepared and wrote the manuscript with input from G. A. Y., H. K. L., M. J. H., and A. L. H.

INTRODUCTION

Regenerating organs restore their original size and shape after injury. Vertebrate appendage regeneration, including that of teleost fish fins, provides a striking example of this phenomenon. Major fin amputations, tiny resections, and cuts of diverse geometry all produce the same outcome – a restored fin matching the original's form and in scale with the animal's body. Spallanzani, Broussonet, and T. H. Morgan pioneered studies of this longstanding mystery of regeneration in the 18th and 19th centuries (Broussonet, 1786; Morgan, 1900). For example, Morgan used oblique caudal fin resections to show that regeneration rates initially correlate with the amount of tissue lost and then progressively slow, ultimately stopping growth when the original size is regained (Morgan, 1900).

Prevailing models, now largely from zebrafish studies, posit that fin tissue adjacent to damage sites interpret Cartesian coordinate-like positional information to trigger the appropriate rate and extent of re-growth (Nachtrab, Kikuchi, Tornini, & Poss, 2013; Rabinowitz et al., 2017; Rolland-Lagan, Paquette, Tweedle, & Akimenko, 2012; Tornini et al., 2016; Wolpert, 2016). This concept supposes an extensive array of positional identities, some epigenetic mechanism for cells to store such identities, and, perhaps most puzzling, for the positional information to be restored during the regeneration process. Ultimately, however, the rate and extent of outgrowth is dictated by production of growth factors, including FGF (Y. Lee, Grill, Sanchez, Murphy-Ryan, & Poss, 2005; Poss et al., 2000; Shibata et al., 2016) and Wnt (Stewart et al., 2014; Stoick-Cooper et al., 2007; Wehner et al., 2014), with the net effect of promoting cellular proliferation. Therefore, understanding growth factor production dynamics provides a logical entry to uncover fin size and shape restoration mechanisms.

Progressive fin regenerative outgrowth depends on spatially segregated growth factor production within an organized blastema. The blastema comprises heterogeneous cell types and forms soon after amputation by de-differentiation of mature cells and their migration into a cavity defined by the enveloping wound epidermis (Wehner & Weidinger, 2015). The blastema then arranges by both cell type and cell state, with distal progenitor and proximal differentiating zones. De-differentiated progenitor osteoblasts (pObs) migrate to blastema peripheries and hierarchically arrange with most progenitor state cells distally enriched (Stewart et al., 2014). Differentiating osteoblasts derived from the pOb pool locate more proximally and continue maturing to progressively extend re-forming bony rays. The central core of the blastema is largely comprised of "activated" mesenchymal cells that spill out from injury-exposed intra-ray space (Tornini et al., 2016; Tornini, Thompson, Allen, & Poss, 2017). These mesenchymal cells are the likely source of a distal, specialized "orchestrating center" (Wehner et al., 2014) that generates a pro-growth environment, including by producing mitogenic FGF (Y. Lee et al., 2005; Poss et al., 2000; Shibata et al., 2016) and pro-progenitor Wnt (Y. Lee et al., 2009; Stewart et al., 2014; Stoick-Cooper et al., 2007; Wehner et al., 2014). An even further distal, small pool of distinct blastema cells may serve as a largely quiescent reservoir (Nechiporuk & Keating, 2002). Distal blastema progenitor-supporting activity is balanced by proximal pro-differentiation signals, including BMP and Wnt-opposing Dkk1 produced by pObs that transitioned from a progenitor to differentiating state (Stewart et al., 2014).

RESULTS

Wnt signals indirectly promote cell proliferation (Wehner et al., 2014), in part by maintaining pObs (Stewart et al., 2014), to drive outgrowth until the fin is fully restored. Wnts such as *wnt5a*, *wnt5b*, and *wnt10a* are produced in the regenerating fin (Y. Lee et al., 2009; Stewart et al., 2014; Stoick-Cooper et al., 2007; Wehner et al., 2014) including by distal blastema cells. We hypothesized differential Wnt production determines the rate and ultimately extent of regeneration. Revisiting Morgan's experiments (Morgan, 1900), we obliquely amputated adult zebrafish fins from the distal tip of the dorsal side to a proximal location ventrally (see Fig. S2.1 for fin amputation planes and anatomical definitions). We then variably inhibited Wnt secretion by graded dosing of low concentrations of Wnt-C59 (Proffitt et al., 2013; Stewart et al., 2014). Partial perturbation of Wnt signaling prevented dorsal but not ventral tissue regeneration (Fig. 2.1A-E). Similarly, central tissue was more sensitive than peripheral tissue to Wnt inhibition following perpendicular resections (Fig. S2.2). We infer differential Wnt production underlies reacquisition of the stereotypical shape of a zebrafish fin. Concordantly, levels of *wnt5a*, a representative distal blastema-expressed Wnt (Y. Lee et al., 2009; Stewart et al., 2014; Stoick-Cooper et al., 2007; Wehner et al., 2014), correlated with the demand for regenerative growth along the proximal-distal axis four days after oblique fin amputations (Fig. 2.1F, G).

Wnt signaling "strength" could be encoded either by the amount of Wnt produced per distal blastema cell or the number of Wnt-producing cells. Regardless, we reasoned that understanding the properties of this unique population was key to deciphering size control mechanisms. Hereafter, we term these "niche cells" for brevity and because they generate the pro-progenitor and pro-growth environment that enables tissue expansion (Morrison & Spradling, 2008). We used RNA-Seq of 4 days post amputation (dpa) distal vs. proximal fin regenerates, as demarcated by the distal epidermal marker Tg(*shha:EGFP)* (Ertzer et al., 2007), to identify niche-characterizing factors (Fig. S2.3). Among transcription factors, the *dachshund* (*dach*) family members (Mardon, Solomon, & Rubin, 1994; W. Shen & Mardon, 1997) *dacha* (5.9-fold) and *dachc* (6.0-fold) were notably distally enriched (Fig. S2.3). We also used the RNA-Seq dataset to confirm the

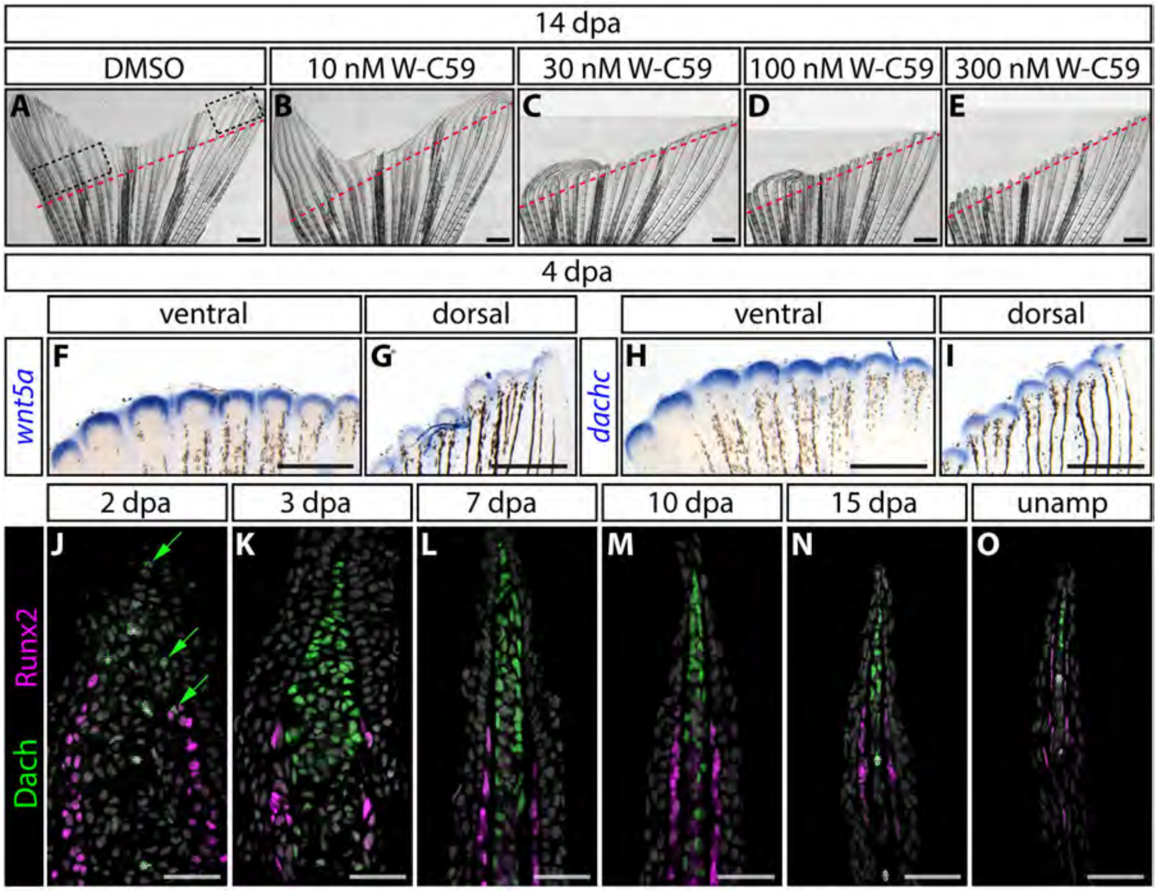

Figure 2.1. Dachshund transcription factors define a progressively depleting pool of distal niche cells in regenerating fins. (**A-E**) Sensitivity to Wnt inhibition inversely correlates with demand for regenerative growth. Diagonally fin-amputated zebrafish exposed to increasing concentrations of Wnt-C59 Porcupine inhibitor and imaged at 14 days post amputation (dpa). Red dashed lines show the amputation plane. Scale bars are 1 mm. (**F-I**) The size of distal *wnt5a* and *dachc* expression domains positively correlate with regenerative demand following diagonal amputations. Images compare whole mount RNA in situ hybridization signal intensities between ventral (proximally amputated) and dorsal (distally amputated) sites along the diagonal resection plane, approximated by dashed boxes in (A). Scale bars are 500 µm. (**J-O**) Dachshund (Dach) expression defines "niche" cells in the distal blastema, distinct from adjacent Runx2-expressing progenitor osteoblasts. Dach$^+$ cells are first observed at 2 dpa, peak in number around 3 dpa, and then progressively decrease to a small residual pool that is also present in unamputated fins. Images show antibody-stained regenerating fin sections at the indicated times post-amputation. Dach and Runx2 are green and magenta, respectively. Hoechst-stained nuclei are grey. Asterisks denote red blood cells. Scale bars are 25 µm.

distal enrichment of several Wnts, with particularly high levels of *wnt5a* and *wnt5b* (Fig. S2.3). *dachc* mimicked *wnt5a* in having notably higher expression levels in 4 dpa proximal tissue of diagonally amputated regenerating fins (Fig. 2.1H, I).

Wnt signaling "strength" could be encoded either by the amount of Wnt produced per distal blastema cell or the number of Wnt-producing cells. Regardless, we reasoned that understanding the properties of this unique population was key to deciphering size control mechanisms. Hereafter, we term these "niche cells" for brevity and because they generate the pro-progenitor and pro-growth environment that enables tissue expansion (Morrison & Spradling, 2008). We used RNA-Seq of 4 days post amputation (dpa) distal vs. proximal fin regenerates, as demarcated by the distal epidermal marker Tg(*shha:EGFP)* (Ertzer et al., 2007), to identify niche-characterizing factors (Fig. S2.3). Among transcription factors, the *dachshund* (*dach*) family members (Mardon et al., 1994; W. Shen & Mardon, 1997) *dacha* (5.9-fold) and *dachc* (6.0-fold) were notably distally enriched (Fig. S2.3). We also used the RNA-Seq dataset to confirm the distal enrichment of several Wnts, with particularly high levels of *wnt5a* and *wnt5b* (Fig. S2.3). *dachc* mimicked *wnt5a* in having notably higher expression levels in 4 dpa proximal tissue of diagonally amputated regenerating fins (Fig. 2.1H, I).

We used antibody staining to conclusively identify caudal fin cells that express Dacha/c (hereafter referred to as Dach) over the course of fin regeneration (Fig. 2.1J-O). Dach-expressing cells were rarely observed before 3 dpa (Fig. 2.1J). At 3 dpa, Dach became robustly expressed in distal cells adjacent to, but distinct from, Runx2^{+} pre-osteoblasts (Fig. 2.1K). Dach$^+$ niche cells then steadily reduced over the course of regeneration to a small residual population also found in distal tissue of unamputated fins (Fig. 2.1L-O). We conclude Dach transcription factors mark Wnt-producing niche cells throughout the course of regeneration. The three-day delay prior to the appearance of Dach$^+$ niche corresponds with the view that fin regeneration proceeds by an acute injury repair phase followed by a prolonged period of progressive outgrowth (Wehner & Weidinger, 2015). Finally, differential numbers of niche cells produced upon injury and then maintained through regeneration likely accounts for our observation that variable Wnt strength correlates with extent of fin outgrowth.

Wnt/β-catenin signaling is active in niche cells where it indirectly promotes further proximal mesenchyme proliferation (Wehner et al., 2014). However, a potential role for Wnt in maintaining the niche pool itself is unexplored. Using the new Dach marker, we found that pan-Wnt inhibition initiated at 4 dpa using Wnt-C59 depleted niche cells (Fig. S2.4). Wnt inhibition prevented outgrowth but did not disrupt osteoblast differentiation, joint formation, or skeletal maturation (Fig. S2.4), reinforcing our previous insight that Wnt/β-catenin promotes bone progenitor maintenance upstream of and in opposition to differentiation (Stewart et al., 2014). Wnt, whether canonical or non-canonical, appears to have an analogous autocrine role – maintaining the niche population in a state whereby it can drive continued regeneration.

The loss of niche cells upon Wnt inhibition allowed us to test if artificial depletion of the niche pool mimics normal termination of regeneration – as supported by our observation that Dach$^+$ niche cells progressively decrease over regeneration. Wnt inhibition irreversibly blocked fin regeneration, with only rare outgrowth seen long after drug removal (Fig. S2.4). In contrast, re-amputating Wnt-inhibited fins re-initiated full regeneration. Small molecule inhibition of FGF receptor signaling prevented outgrowth to the same degree as Wnt inhibition (Fig. S2.4). However, as FGF inhibition did not deplete Dach$^+$ niche cells (Fig. S2.4), regeneration resumed following drug washout, matching previous observations (Y. Lee et al., 2005). Therefore, mitogenic FGF, which appears niche-expressed (Y. Lee et al., 2005; Poss et al., 2000; Shibata et al., 2016) and is Wnt-dependent (Wehner et al., 2014), acts downstream of Wnt's niche maintenance role. We propose niche cell numbers set dynamic levels of both signaling proteins and therefore the outgrowth rate. Regeneration ceases when the niche pool, and correspondingly Wnt and FGF production, depletes below an effective level. By this model, understanding instructive growth control mechanisms requires revealing niche cell origins and fates.

Regenerated fin tissues are derived from progenitor cells formed by partial de-differentiation of mature cells extant at the injury site (Wehner & Weidinger, 2015). We sought to determine which pre-existing cell type(s) generates Dach$^+$ niche cells. An obvious candidate was intra-ray mesenchyme, including joint-associated fibroblasts, that are activated some distance proximal to the amputation site and express *tryptophan hydroxylase 1b* (*tph1b*) (Tornini et al., 2016). These cells, which contribute to the distal blastema, are a source of replacement ray mesenchyme (Tornini et al., 2016, 2017). We used a mosaic lineage tracing system (Stewart & Stankunas, 2012) to permanently label intra-ray mesenchyme of individual rays in uninjured fins by transgenic mCherry expression (Fig. 2.2A-D). We then amputated these fins and double stained 4 dpa sections containing labeled rays and derived regenerating tissue with Dach and mCherry antibodies. Distal but not proximal mCherry-expressing blastema cells co-expressed Dach. Further, Dach^{+} niche cells largely co-expressed *Tg(tph1b:mCherry)* (Fig. 2.2E, F). Finally, we found the fin regenerate-expressed Msx transcription factor (Smith et al., 2008) marks both proximal blastema cells and distal Dach-expressing cells (Fig. 2.2G). We conclude Dach^{+} niche cells derive from intra-ray mesenchyme that initially populates the distal portion of the blastema.

The mesenchymal cell state marker Snail (Lamouille, Xu, & Derynck, 2014) was expressed in un-injured intra-ray and proximal regenerate mesenchymal cells (Fig. 2.2H, I). In contrast, Snail was absent from Dach^{+} niche cells except for a small population of transitioning double Dach^{+}/Snail^{+} cells (Fig. 2.2I). Concordantly, *snai2* transcripts were abundant in blastema mesenchyme but undetectable in distal-most tissue (Fig. S2.5). Dach-positive cells incorporated EdU even with a brief 4-hour pulse prior to tissue collection, showing the niche population includes actively proliferating cells (Fig. S2.5). These observations support a cyclical model whereby fin amputation induces a delayed transition of Snail^{+} intra-ray mesenchyme to a Dach^{+} niche state (Fig. 2.2J, K; Fig. S2.6). The Dach-expressing niche cells proliferate but, on net, progressively deplete through their conversion back to Snail^{+} mesenchyme that re-populates regenerated bony rays.

The origin of niche cells from intra-ray mesenchyme led us to consider that skeletal geometry might instruct how much niche is formed upon amputation. By this model, resecting a larger bony ray, with a relatively high volumetric capacity for mesenchyme, would produce a larger initial niche population and therefore more regeneration. In support, the size of fin ray bone segments noticeably tapers along the proximal-to-distal axis (Fig. 2.3A-E). Further, longer peripheral rays are wider at their base than shorter central rays. 3-D micro-CT analysis confirmed this assessment and underscored that the internal geometry of the rays approximates cylinders (Fig. S2.7; Supplemental Video 2.1). Therefore, we considered the activated stretch of a ray extending proximally from an injury site (Knopf et al., 2011; Tornini et al., 2016) as a cylinder of fixed length but variable width.

Figure 2.2 (next page). Niche cells are generated from state-transitioning intra-ray mesenchyme. (A-D) Genetic mosaic analysis demonstrates that the Wnt-producing niche derives from intra-ray mesenchyme. Example of a genetic mosaic fin with a single ray containing mCherry-labeled mesenchyme (in magenta) prior to amputation (A) and 4 dpa (B). The amputation plane is indicated with a dashed yellow line. (C, D) A section of the same ray at 4 dpa stained with anti-Dach (grey in single channel image in C, green in D) and anti-mCherry antibodies (red). Red arrows mark mCherry$^+$ but Dach$^-$ blastema cells and yellow arrows highlight Dach$^+$/mCherry$^+$ niche cells. **(E, F)** Tg(tph1b:mCherry) expression highlights the regenerating intra-ray mesenchyme/niche lineage. Immunostaining of a 4 dpa Tg(tph1b:mCherry) fin section shows Dach (green) and tph1b (red) expressing niche cells (yellow arrows). Red arrows mark further proximal Dach$^-$/mCherry$^+$ blastema cells. **(G-I)** Mesenchymal-to-niche cell transitions at 4 dpa defined by Dach, Msx, and Snail transcription factors. (G) Like tph1b:mCherry, Msx expression (red) labels the lineage whether in a differentiated mesenchyme (red arrows) or Dach-expressing (green) niche (yellow arrows) state. (H, I) Snail expression (red nuclei shown with red arrows) marks intra-ray mesenchyme proximal to the amputation site and blastema cells except distal Dach$^+$ niche cells (green nuclei highlighted by green arrows). A small number of Snail$^+$/Dach$^+$ cells (yellow nuclei indicated by yellow arrows) identify cells transitioning between mesenchyme and niche states. Scale bars in all panels are 25 μm. Asterisks denote red blood cells. **(J)**. Model of cell state transitions between intra-ray mesenchyme and niche cells during regeneration. Snail$^+$ mesenchyme cells normally populate the intra-ray space. After amputation, Snail$^+$ cells dedifferentiate into Dach$^+$ niche cells. As ray outgrowth proceeds, niche cells redifferentiate to contribute Snail$^+$ intra-ray mesenchyme. **(K)** Control of regeneration by a Wnt-producing dynamic niche pool. Runx2$^+$ osteoblasts (in pink) are maintained by Wnt (represented by cyan nuclei) secreted by the distal Dach$^+$/Wnt$^+$ niche (green cells with cyan nuclei), which transition (yellow cells) back to Snail$^+$ mesenchyme (red cells) as regeneration progresses.

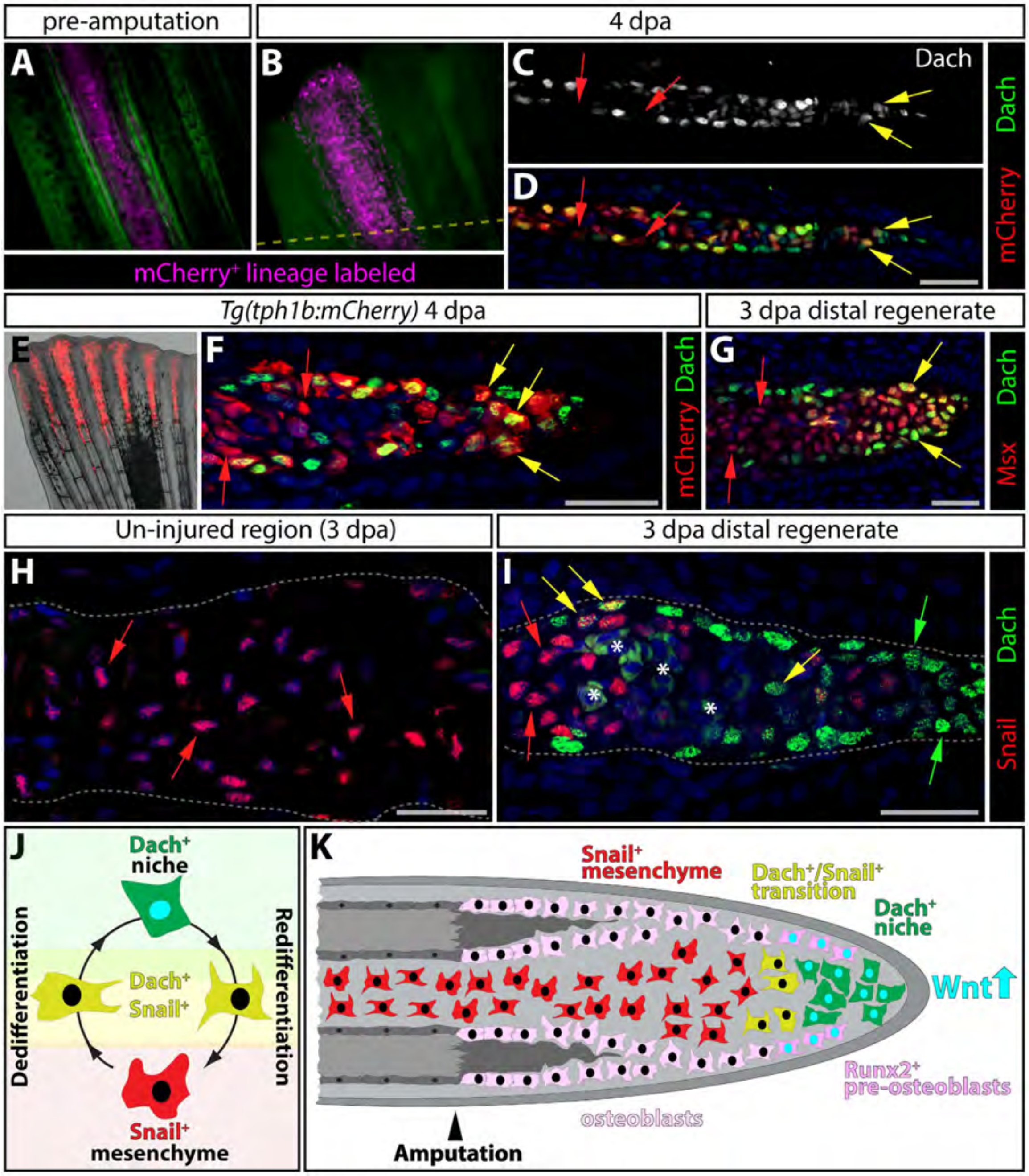
pre-amputation
4 dpa
A
B
C
Dach
D
Dach
mCherry
mCherry⁺ lineage labeled
Tg(tph1b:mCherry) 4 dpa
3 dpa distal regenerate
E
F
mCherry Dach
G
Dach
Msx
Un-injured region (3 dpa)
3 dpa distal regenerate
H
I
Dach
Snail
J
Dach⁺ niche
Dach⁺ Snail⁺
Snail⁺ mesenchyme
Dedifferentiation
Redifferentiation
K
Snail⁺ mesenchyme
Dach⁺/Snail⁺ transition
Dach⁺ niche
Wnt
Runx2⁺ pre-osteoblasts
osteoblasts
Amputation

As such, a ray's mesenchyme-holding capacity, injury-induced niche size, and finally fin outgrowth should correlate with ray widths at injury positions. We measured the width of the central sixteen rays at a fixed proximal-distal position and then plotted the radius^2 values as adjacent bars. The bars' distribution approximated that of ray lengths, largely matching the overall shape of a zebrafish fin (Fig. 2.3A)

This model predicts niche amount should vary by proximal-distal amputation position, correlating with the tapering bony rays. Whole mount in situ hybridization for *dachc* transcripts at 3 dpa, the time of niche formation, revealed that proximal amputations produced large *dachc*-expressing niche pools while distal cuts generated progressively smaller niches (Fig. 2.3F-H). Further, *dachc* expression across the dorsal-to-ventral fin axis correlated with regenerative demand upon perpendicular resections (Fig. S2.8) – as with diagonal amputations (Fig. 2.1H, I). Peripheral regions that re-form the longest rays expressed high levels of *dachc*. In contrast, central tissue that generates short rays to restore the original V-shaped fin produced small *dachc*-marked niches.

We used mathematical modeling to further explore if skeletal geometry coupled with progressive niche depletion could account for robust size restoration during fin regeneration. We first assumed outgrowth rate is proportional to the current number of distal niche cells. We considered the volume of intra-ray mesenchyme activated proximally to an amputation site (Tornini et al., 2016) determines the size of the starting niche pool. As validated earlier, ray radius^2 then serves as a proxy for the number of initial niche cells. A niche that collectively re-differentiates faster than it proliferates over the course of regeneration establishes a “countdown timer”. The number of initial niche cells sets the timer, with outgrowth ending when the niche population depletes below some effective level. As such, bony ray size at the amputation site ultimately instructs regenerated ray length.

Figure 2.3 (next page). Skeletal geometry-dependent niche generation with progressive niche depletion models regenerated ray length. (A) A ray’s cross-sectional area (therefore, volume) exposed upon amputation (modeled by the square of the radius, r^2, pink) anticipates the length (l, light blue) it will regenerate. Plotted normalized measurements for the sixteen central rays show a tight correlation between ray lengths and ray volumes, from/at a hypothetical proximal amputation position (green line). Error bars are one standard deviation (n = 4). (**B-E**) Scale-matched zoom images of the ray segments boxed in the stitched whole fin image in (A), showing differential girth depending on bone position. Pink lines mark ray diameters. **(F-H)** *dachc* whole mount in situ hybridizations on 72 hpa regenerating fins amputated at distal (F), intermediate (G), or proximal (H) positions. As anticipated by the model, *dachc* expression, representing the amount of niche generated, correlates with regenerative demand. Scale bars are 500 µm. **(I)** A mathematical model equation represents the length of a given ray at the end of regeneration ($l(t_{end})$) as a function of the radius of the ray at the amputation position. Three scaling parameters (k_l, α, and β) must be tuned precisely to restore the original length, but no molecular positional information is required. The plot shows how the formula theoretically restores normalized ray lengths using actual measured radius values at the hypothetical amputation point (green line). **(J)** Scatter plot showing a linear relationship between ray volume and ray length from any measured position along the proximal-distal (P-D) fin axis. Each point represents 5 or 6 measured points from each of rays 3, 4, 15, 16 from four animals. Matching data point colors/shapes indicates a given ray units are arbitrary. **(K)** The mathematical model predicts regenerated length (normalized = 1) regardless of amputation position (normalized units). Each data point shows the theoretical length derived from a given ray’s radius measurements at a single P-D position. The colored vertical lines represent anticipated growth from the amputation position (therefore, starting from the black diagonal line).

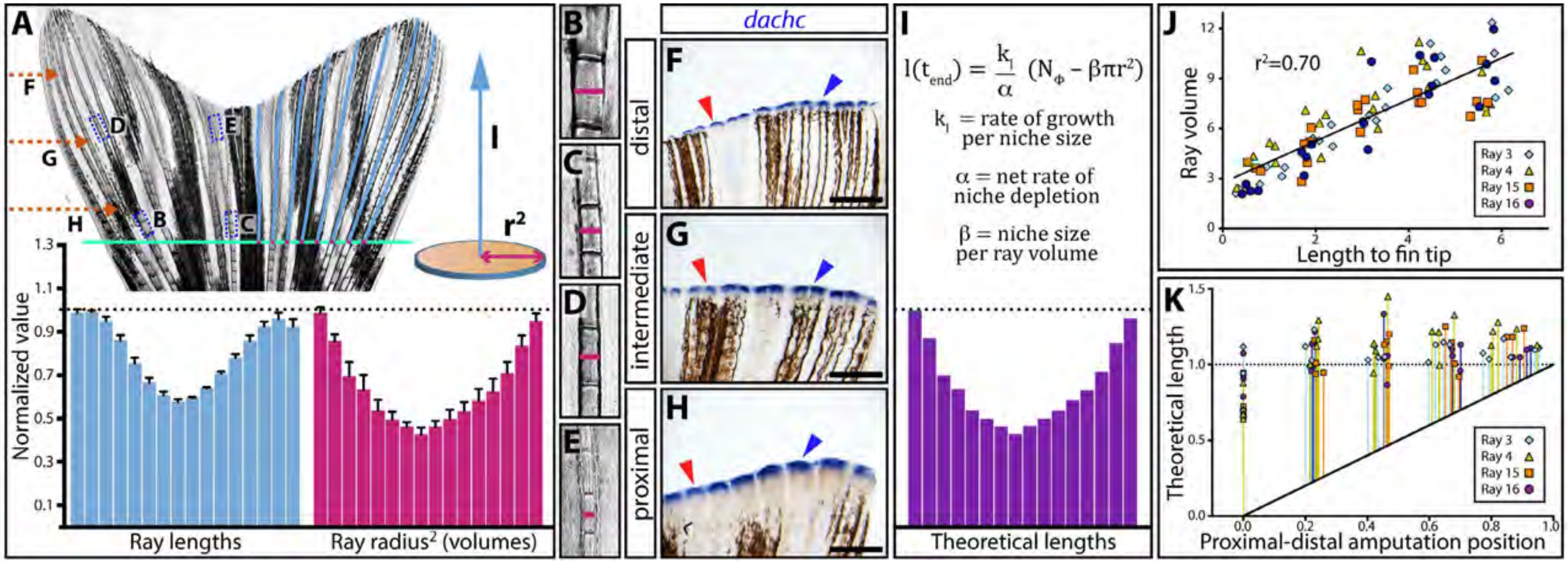
A
F
G
H
D
E
B
C
l
r²
1.3
1.1
0.9
0.7
0.5
0.3
0.1
Normalized value
Ray lengths
Ray radius² (volumes)
B
C
D
E
dachc
distal
intermediate
proximal
F
G
H
I
l(t_end) = k_l/α (N_Φ − βπr²)
k_l = rate of growth per niche size
α = net rate of niche depletion
β = niche size per ray volume
Theoretical lengths
J
r²=0.70
Ray volume
12
9
6
3
0
0
2
4
6
Length to fin tip
Ray 3
Ray 4
Ray 15
Ray 16
K
Theoretical length
1.5
1.0
0.5
0.0
0.0
0.2
0.4
0.6
0.8
1.0
Proximal-distal amputation position
Ray 3
Ray 4
Ray 15
Ray 16

We solved differential equations to derive a final equation describing regenerated ray length as a function of ray radius at the amputation position and three "scaling parameters":

$$l(t_{end}) = \frac{k_l}{\alpha}(N_{\Phi} - \beta\pi r^2)$$

where k_l is the rate of length growth per niche cell, α is the difference in niche cell growth rate versus rate of differentiation back to intra-ray mesenchymal cells, N_{Φ} is the number of niche cells below which growth stops, and β is the number of niche cells released per injury-activated ray volume. Mathematically exploring the formula reinforced the conclusion that α must be negative to provide net niche depletion. Solving expected regenerated ray lengths using measured ray radii and optimized constants produced a distribution largely corresponding with actual measured lengths (Fig. 2.3I) – naturally matching normalized radius^2 distributions. A largely linear relationship between ray radius^2 and remaining ray length from the measurement position held across the proximal-distal fin axis (Fig. 2.3J, R-squared = 0.7). Likewise, existent ray lengths from a hypothetical injury point matched theoretical regenerated lengths derived from radius measurements and our growth equation (Fig. 2.3K).

Several zebrafish mutants develop and regenerate long fins, including dominant *longfin*^{t2} (van Eeden et al., 1996), well known as one of two mutations characterizing the *Tüpfel longfin* (*TL*) strain (Haffter et al., 1996) (Fig. 2.4A, B). *longfin*^{t2} ray volumes estimated by normalized radius^2 measurements predicted overall fin shape but greatly under-anticipated ray lengths (Fig. 2.4C). Therefore, the skeleton was not proportionally re-scaled during development and instead suggesting *longfin*^{t2} disrupts an outgrowth regulatory mechanism. We used our mathematical model to predict the growth-determining scaling parameter disrupted in *longfin*^{t2} fish. The cell proliferation rate (k_l) could be larger (e.g. increased mitogen production or mitogen sensitivity), β could be larger, establishing a larger niche pool upon injury, or α could be "less negative", leading to niche perdurance. Changing k_l or β vs. α had distinct theoretical effects when plotting expected regenerative growth over time and growth rate over time (Fig. 2.4D, E). Following amputation, *longfin*^{t2} fish showed prolonged regenerative growth rather than increased initial growth or peak growth rate (Fig. 2.4F, G; Fig. S2.9), suggesting they have a persistent niche (less negative α) rather than enhanced niche generation (β) or increased cellular growth rate (k_l).

We examined *dachc* expression in *longfin*^{t2} heterozygotes following fin resection to see if niche dynamics were disrupted as anticipated by our modeling (Fig. 2.4H-Q). *longfin*^{t2} fish initially formed a normal-sized niche. However, unlike wildtype clutchmates, their *dachc*-expressing niche only slowly depleted, implicating a less negative α constant. Increasing α while inputting *longfin*^{t2} ray radii measurements largely predicted actual *longfin*^{t2} regenerated ray lengths (Fig. S2.10). These results support the robustness of the model and show that *longfin*^{t2} disrupts the niche depletion system.

DISCUSSION

We conclude ray volumes (set by their widths) are "transposed" into regenerated ray lengths, and hence fin form, via the amount of intra-ray mesenchyme exposed upon ray resection. The mesenchyme transitions into a concordantly sized outgrowth-promoting niche pool that then steadily depletes, ultimately returning the regenerated fin to its original size and shape. In 1929, Samuel Nabrit similarly concluded: "… *in [fin] regeneration the rate of growth and consequently the form is controlled locally by the cross-sectional area of the fin rays exposed*" (Nabrit, 1929). Therefore, Nabrit's predicted growth promoting "fin ray end substance" likely is the injury-released intra-ray mesenchyme itself. Positional information stored in tapering ray skeletal geometry is self-restoring since a depleting niche progressively directs slower outgrowth and narrower

---

Figure 2.4 (next page). *longfin* fish regenerate exceptionally long fins due to a broken niche countdown timer, supporting a transpositional scaling model of self-restoring fin geometry. (A, B) Stitched differential interference contrast images show the dramatically overgrown caudal fins of *longfin*$^{t2/+}$ fish. Ray length and radius measurements taken at/from a proximal position denoted by colored dashed lines (brown/yellow=*longfin*$^{t2/+}$, light blue/pink=wildtype). Scale bars are 2 mm. **(C)** Normalized caudal fin ray lengths (left) and volumes (from *radius*^{2} measurements, right) for clutchmate wildtype and *longfin*$^{t2/+}$ fish. **(D)** Theoretical regeneration growth and **(E)** growth rate curves derived from the transpositional scaling equation have distinct shapes depending if niche response (k_l) or niche generation (β) vs. niche perdurance (α) parameters are increased. The actual growth **(F)** and growth rate **(G)** of regenerating *longfin*$^{t2/+}$ caudal fins match expectations if niche perdurance (α) – the "countdown timer" – is disrupted. The initial and maximum growth rate is unaltered but the growth rate progressively decreases at a much slower rate. Curves show actual data fit to the modeling equations (r-squared goodness of fit values are shown). All data points ($\geq$ 12 fish per time) are shown in (F); points in (G) are mean values. (**H-Q**) Whole mount in situ hybridization for the *dachc* niche marker through a time course post-caudal fin amputation for wildtype and *longfin*$^{t2/+}$ fish. *longfin*$^{t2/+}$ fish generate a normal-sized niche after fin resection but the cells fail to deplete in a timely manner. Scale bars are 200 μm. **(R)** A "Transpositional Scaling" model can explain how positional information stored in skeletal geometry combined with a state transitioning and depleting niche population directs a fin to regenerate back to its original size and shape. A wider amputated ray produces more niche cells from its intra-ray mesenchyme (A tapered, segmented ray is shown on the left, with intra-ray volume graded from orange (more) to green (less)). Niche cells deplete at a constant rate through their re-differentiation to mesenchyme (starting and then diminishing niche pools represented by same orange-to-green gradation as well as circle sizes on the right fin graphic). The diminishing niches maintain progressively smaller bone progenitor pools, regenerating tapered rays and inherently restoring skeletal geometry primed for future injury responses.

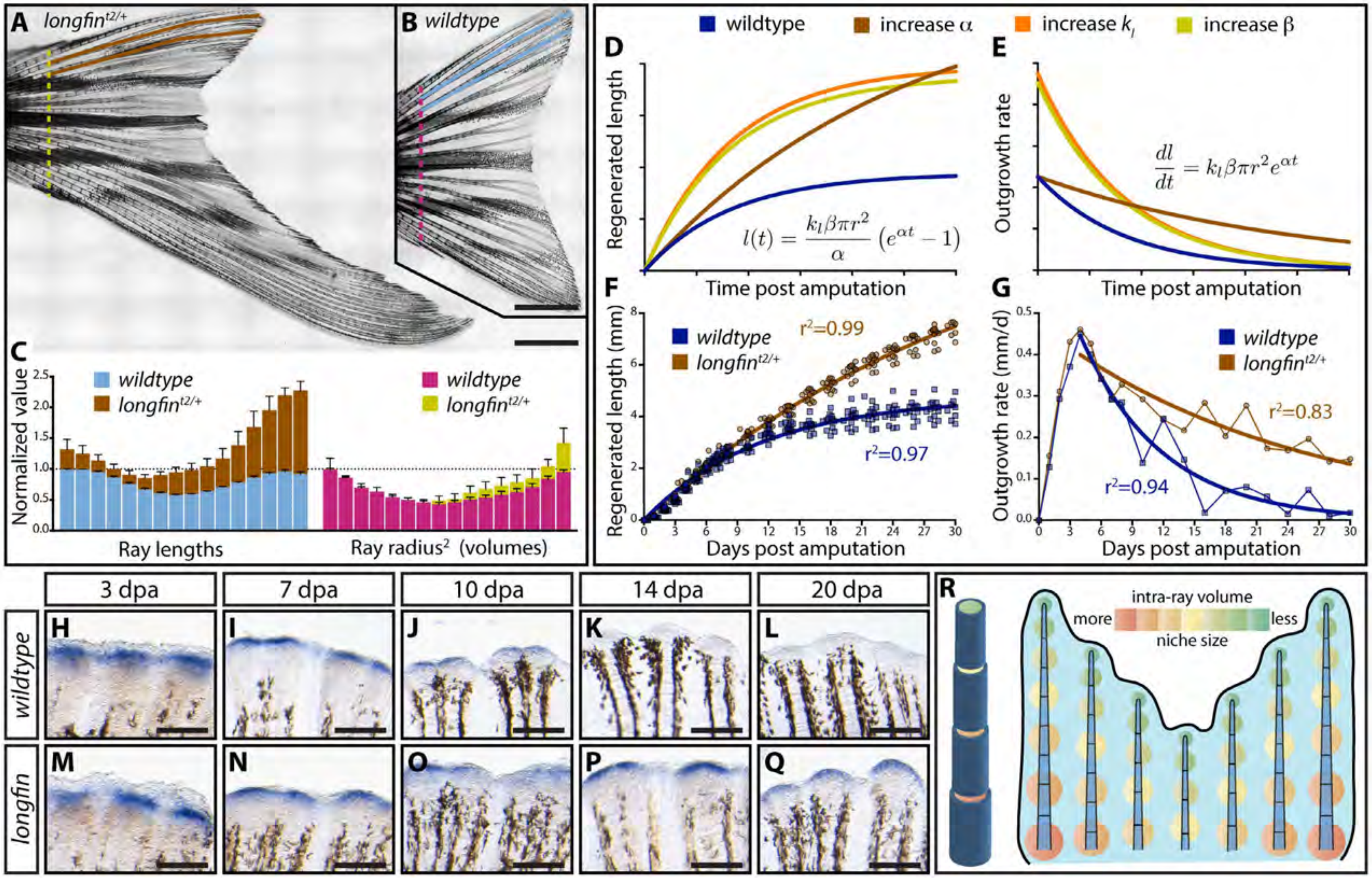
A longfin t2/+
B wildtype
C
Normalized value
0.0
0.5
1.0
1.5
2.0
2.5
wildtype
longfin t2/+
wildtype
longfin t2/+
Ray lengths
Ray radius² (volumes)
wildtype
increase α
increase k_l
increase β
D
Regenerated length
$l(t) = \frac{k_l \beta \pi r^2}{\alpha}(e^{\alpha t} - 1)$
Time post amputation
E
Outgrowth rate
$\frac{dl}{dt} = k_l \beta \pi r^2 e^{\alpha t}$
Time post amputation
F
Regenerated length (mm)
wildtype
longfin t2/+
r²=0.99
r²=0.97
Days post amputation
G
Outgrowth rate (mm/d)
wildtype
longfin t2/+
r²=0.83
r²=0.94
Days post amputation
3 dpa
7 dpa
10 dpa
14 dpa
20 dpa
wildtype
longfin
H
I
J
K
L
M
N
O
P
Q
R
intra-ray volume
more
less
niche size

bones due to its diminishing progenitor-maintenance capacity. We use the term "transpositional scaling" to describe this model for organ size determination – a new answer to an age-old question of appendage regeneration.

Vertebrate appendage regeneration, including that in zebrafish fins, is used as compelling evidence for pattern formation by Cartesian coordinate-defined cellular positional identities (Wolpert, 2016). However, our transpositional scaling model does not require fin cells retain any such molecular information. Similarly, the hypothesized "pre-pattern" established early in a regenerating blastema that directs regional outgrowth (Nachtrab et al., 2013; Rabinowitz et al., 2017; Rolland-Lagan et al., 2012; Tornini et al., 2016) can be explained by skeletal geometry-defined niche cell numbers alone. The state transition mechanisms that generate the niche and drive its progressive depletion are then identical throughout the fin but produce differential, predictable output depending on the starting condition defined by ray volumes.

Our conclusion linking *longfin*^{t2} to disrupted niche depletion shows how a mutant can have profound effects on fin morphology by altering the α scaling parameter defined by our mathematical model. As such, we provide a framework to understand evolutionary origins of appendage size and shape variation. In the accompanying manuscript, we identify *cis* ectopic expression of the voltage-gated potassium channel *kcnh2a* in mesenchyme/niche lineage as the long sought cause of *longfin*^{t2} (Stewart et al., 2019). These studies link ion signaling or bioelectricity, widely connected to organ size control and regeneration (McLaughlin & Levin, 2018), to gene regulatory pathways regulating cell state transitions that slow then terminate fin outgrowth.

Could "transpositional scaling" models apply in other circumstances where an organ is restored to form and scale? The hemi-ray bones in zebrafish fins appose to approximate cylinders, conveniently enabling consideration of the geometric storage of a growth-promoting cell lineage. Urodele amphibian limb regeneration is another striking model of size and pattern restoration. Matching our idea, an older model proposes that initial blastema mass rather than origin determines which proximal-distal limb skeletal elements regenerate (de Both, 1970). However, urodele limb cartilage/bones are solid and therefore position-defining geometric reservoirs of a hypothetical niche lineage would have to lie around rather than inside skeletal structures. Intriguingly, urodele limb positional information is stored in connective tissue mesenchyme surrounding bones, albeit reportedly by molecular memories (Kragl et al., 2009; McCusker, Diaz-Castillo, Sosnik, Q. Phan, & Gardiner, 2016; Nacu et al., 2013). Regardless, progenitor cell supporting-niche populations are a common component of organ growth, homeostasis, and regeneration (Chacón-Martínez, Koester, & Wickström, 2018; Yamashita & Tumbar, 2014). Our simple model, inherently dependent on regulatory networks with the positional information stored in tissue geometry rather than molecular information, establishes a compelling paradigm to explore in many contexts.

MATERIALS AND METHODS

Zebrafish

Wildtype AB (University of Oregon Zebrafish Facility), *longfin*^{t2} (Haffter et al., 1996; Maderspacher & Nüsslein-Volhard, 2003; van Eeden et al., 1996), *Tg(-*

2.4shha:gfp:ABC) (Ertzer et al., 2007), *Tg(tph1b:mCherry)* (Tornini et al., 2016), *Tg(dusp6:CreERT)* (Stewart & Stankunas, 2012), and *Tg(eab:FlEx)* (Boniface, Lu, Victoroff, Zhu, & Chen, 2009) zebrafish lines were used. Zebrafish were housed in the University of Oregon Aquatic Animal Care Services facility at 28-29°C. The University of Oregon Institutional Animal Care and Use Committee oversaw animal use.

Transgenic mosaic fin lineage tracing

Zebrafish embryos carrying the *Tg(dusp6:CreERT)* and *Tg(eab:FlEx)* lines were treated with low doses of tamoxifen, reared to adulthood, screened for mosaic labeling, caudal fin-amputated, and analyzed by whole mount imaging and antibody staining of sectioned tissue as described previously (Stewart & Stankunas, 2012).

Small molecule studies of fin regeneration

The Porcupine inhibitor Wnt-C59 (Proffitt et al., 2013), which blocks Wnt secretion, and the FGF receptor tyrosine kinase inhibitor PD173074 (Mohammadi et al., 1998) were dissolved and diluted in DMSO. Caudal fins were amputated at a fixed proximal-distal position or common oblique plane (illustrated in Fig. S2.1). Fin-resected fish were then immediately placed in drug-containing aquarium water. Animals were transferred to fresh drug-containing water every 48 hours. The final concentration of DMSO in fish water was 0.01% for all conditions.

For niche depletion experiments with delayed small molecule addition (Fig. S2.4), fin-resected AB wildtype fish first were allowed to regenerate for 4 days. The animals then were treated with DMSO (0.01%, n = 10), Wnt-C59 (500 nM, n = 10), or PD173074 (5 μM, n = 10) for another 4 days. Animals were fed and changed to fresh drug-containing water after 48 hours. At 8 days post-amputation (dpa), animals were returned to plain fish water. In some cases, fins were subjected to a second amputation proximal to the original amputation site at 12 dpa. Animals were followed for up to 60 dpa, when each fish was imaged using a Leica M165 FC stereomicroscope. Representative fish for each condition were visualized using high resolution stitched imaging (Nikon Eclipse Ti widefield microscope and NIS-Elements software) before drug treatment, immediately after drug treatment, and at the experiment's conclusion. Regeneration was quantified by scoring the number of fully regenerated individual rays. This complete experiment was repeated three times with the same outcomes.

RNA-Seq

Caudal fins of adult *Tg(-2.4shha:gfp:ABC)* zebrafish were resected. At 4 dpa, dissected regenerated tissue at and beyond the distal GFP-marked epidermal domains was collected as "distal regenerate" samples. The remaining proximal regenerated tissue also was harvested. Tissue pooled from four animals constituted matched replicate samples. Tissue was immediately placed in TRIzol reagent (Thermo Fisher) and homogenized. RNA was isolated following the manufacturer's instructions with minor alterations. The RNA was precipitated overnight at -80ºC and then pelleted at 15,000 rpm for 30 minutes at 4ºC. Pellets were washed twice with 70% ethanol, dried for 10 minutes at room temperature, and resuspended in RNase-free water (Thermo Fisher).

RNA-Seq libraries were prepared from 1 μg of isolated RNA using a Kapa Biosystems Stranded mRNA-Seq kit. Bar-coded libraries were pooled and sequenced using a NextSeq 500 (Illumina). Illumina reads were aligned to the zebrafish genome (GRCz11) using TopHat2 (Kim et al., 2013). Gene-assigned aligned reads were counted using HTseq (Anders, Pyl, & Huber, 2015). DEseq (Anders & Huber, 2010) was used to determine differential expression of 1147 genes annotated to have “transcription regulator activity” (GO:0140110) by AmiGO 2 (Ashburner et al., 2000; Blake et al., 2013; Carbon et al., 2009). Genes below the 40% quantile for total counts were filtered out to improve the statistical analysis of relatively highly expressed genes.

Immunostaining and in situ hybridization

Immunostaining was performed on paraffin sections as described (Stewart et al., 2014). Antibodies used were: Runx2 (Santa Cruz Biotechnology, 27-K, 1:500-1000 dilution); Dach (Proteintech Group, 1:2000); Msx (Developmental Studies Hybridoma Bank, tissue culture supernatant, 1:15-20); Snail (Developmental Studies Hybridoma Bank, ascites, 1:100); mCherry (Takara Bio or Novus Biologicals, 1:100). For Snail/Dach double immunostaining, Dach antibodies were used at 1:1000 and sodium dodecyl sulfate (SDS) was added to 0.005% during the primary antibody incubation step. Immunostained sections were imaged using either Olympus FV1000 or Zeiss LSM 880 laser scanning confocal microscopes.

Whole mount in situ hybridization using DIG-labeled probes followed established procedures (Stewart et al., 2014). The *wnt5a* probe was described previously (Stewart et al., 2014). Templates for *dacha* and *dachc* probes were amplified by PCR from regenerating fin cDNA using the indicated primers, where the reverse primer contains a T7 promoter sequence (in caps) for in vitro transcription using DIG labeling mixtures (Roche) and T7 RNA polymerase:

dacha forward: 5’-atggccgtatctgcaactcctccggtgc-3’

dacha reverse: 5’-TAATACGACTCACTATAGGGtcagtacatgatggggggtttggagtagg-3’

dachc forward: 5’-atggcccacgcgcctccga-3’

dachc reverse: 5’-TAATACGACTCACTATAGGGtcagtacatcattgtggactttagaaagagcctt-3’

The *snai2* probe template was generated by PCR amplifying its coding sequence from regenerating fin cDNA using the following primers followed by ligation to the pCRII vector (Thermo Fisher).

snai2 forward: 5’-atgcctcgttcattcctagtaaagaagc-3’

snai2 reverse: 5’-tcagtgtgcgatgcaacagccag-3’

The resulting plasmid was linearized and a DIG-labeled probe synthesized by in vitro transcription using SP6 RNA polymerase.

5-ethynyl-2’-deoxyuridine (EdU) incorporation and staining

10 μg of EdU in saline was intraperitoneally injected into wildtype fish 92 hours post caudal fin amputation. Fin tissue was collected 4 hours later, fixed, and processed for paraffin sectioning. EdU detection used a Click-iT kit (Thermo Fisher) combined with immunostaining as described above using Dach antibodies.

X-ray micro computed-tomography imaging

An adult wildtype zebrafish was sacrificed and fixed in 4% PFA for 24 hours. The specimen was stabilized within a 15 ml conical tube and its caudal fin scanned using a VivaCT 80 (SCANCO Medical) with 55 kVp X-ray source energy, 145 μA current, 6.5 μm pixel size and 1000 ms per projection integration time. Slice images were reconstructed to a 1590x1590 pixel matrix using an automated cone beam convolution backprojection algorithm. The resulting 2-D images were output for 3-D reconstruction using Imaris 9.3 software (Bitplane).

Morphometrics and mathematical modeling

Rays were considered as simple cylinders to facilitate modeling regenerative fin outgrowth as a function of skeletal geometry. A given bony ray segment's volumetric capacity for injury-activated, niche-forming intra-ray mesenchyme (Tornini et al., 2016), then could be estimated by first measuring the ray's width (= diameter) at a hypothetical amputation site. For modeling purposes, the square of the ray's radius was used as a proxy as normalized areas and volumes (for cylinders of a fixed length) are mathematically identical.

Caudal fins of five-month-old *longfin*$^{t2/+}$ and wildtype clutchmate fish were imaged using differential interference contrast microscopy and multi-field stitching (Nikon Eclipse Ti and NIS-Elements) for morphometrics. Fish were euthanized by tricaine bath overdose and mounted in 0.75% low melt agarose / PBS on microscope slides. The fins were gently fanned out using a horse hair brush to fully extend the tissue and separate rays. The initial proximal-distal positions for ray measurements were determined by first identifying the end of the innermost truncated rays (peripheral “mini-rays” that, unlike the standard 18 caudal rays, do not extend the full distance of the fin, shown in Fig. S2.1). A line was drawn across the fin that intersected points two ray bone segments preceding the end of the mini-rays on the fin’s dorsal and ventral sides. The width of each ray was measured where it intersected this transverse line.

Similarly, polylines (using anchored points to allow for shifts in ray orientation) starting from the same proximal-distal position were drawn along each ray and then directly in between branches of a given “mother ray” until reaching the fin tip. The lengths of these lines defined how much each ray would have to regenerate to restore the fin’s original size. Lengths were normalized to the longest wildtype ray. Repeated measures taken every three bone segments along the proximal-distal axis for rays 3, 4, 15, 16 used the same procedure, with lengths representing the distance from the diameter measurement position to the end of the ray.

We derived a mathematical model for “Transposition Scaling” that predicts the extent of regenerative outgrowth as a function of skeletal geometry – the bony ray’s capacity for niche-originating mesenchyme. First, we considered the number of niche cells released at a cut site as:

$$N_0 \equiv \beta \pi r^2$$

where r is the radius of the ray at the cut site and β is the average number of niche cells released per unit area. Niche cells can then proliferate (given by k_g) or convert to a differentiated, mesenchymal state (given by k_q). The change in the number of niche cells per unit time is:

$$\frac{dN}{dt} = \left(k_g - k_q\right)N(t)$$

The difference in these rates can be summarized by $\alpha \equiv (k_g - k_q)$. Using the boundary condition that $N(0) = N_0$, the solution to this first-order differential equation is:

$$N(t) = \beta\pi r^2 e^{\alpha t}$$

We model bony ray growth rate as directly proportional to the number of niche cells, controlled by k_l:

$$\frac{dl}{dt} = k_l N(t) = k_l \beta\pi r^2 e^{\alpha t}$$

Using the boundary condition that $l(0) = 0$, the solution to this differential equation is:

$$l(t) = \frac{k_l \beta\pi r^2}{\alpha}(e^{\alpha t} - 1)$$

To link the number of cells released to the final ray length, we assume that skeletal growth stops when the number of cells reaches N_Φ, the minimum number of cells required to support growth. This happens at t_{end}:

$$N_\Phi = \beta\pi r^2 e^{\alpha t_{end}}$$

We then solve for t_{end}:

$$t_{end} = \frac{ln\left(\frac{N_\Phi}{\beta\pi r^2}\right)}{\alpha}$$

and substitute into our model for $l(t)$:

$$l(t_{end}) = \frac{k_l \beta\pi r^2}{\alpha}\left(e^{\alpha \frac{ln\left(\frac{N_\Phi}{\beta\pi r^2}\right)}{\alpha}} - 1\right)$$

$$l(t_{end}) = \frac{k_l \beta \pi r^2}{\alpha}\left(\frac{N_{\Phi}}{\beta \pi r^2} - 1\right)$$

This gives the final relationship:

$$l(t_{end}) = \frac{k_l}{\alpha}(N_{\Phi} - \beta \pi r^2)$$

where k_l is the length growth rate per niche cell, α is the difference between the niche cell growth rate and their conversion back to intra-ray mesenchymal cells, N_{Φ} is the minimum number of cells required to support growth, and β reflects how many niche cells are released per bony ray cross-sectional area.

Fin regeneration outgrowth measurements

Caudal fins from clutchmate *longfin*$^{+/+}$ *and longfin*$^{t2/+}$ animals were amputated at the same position along the proximal-distal axis (Fig. S2.1) and allowed to regenerate for 30 days. Outgrowth measurements were taken every 24 hours from 1-8 dpa and every 48 hours from 10-30 dpa. The length of the third ray (Fig. S2.1) from the amputation site to the fin's tip was measured from images acquired with a Leica M205 FA stereomicroscope. Stitched fin images of zebrafish euthanized with tricaine and mounted in 0.75% low melting agarose were captured using a Nikon Eclipse Ti widefield microscope and NIS-Elements software. Data points were fit to user-defined transpositional scaling equations (see Mathematical modeling) by nonlinear regression using GraphPad Prism. The α, β, and k_l parameters were allowed to vary to generate best-fit curves. β and k_l were nearly identical between the wildtype and *longfin*$^{t2/+}$ data sets. In contrast, α was 3.0x higher for *longfin*$^{t2/+}$, similar to the α difference (2.1x) derived from the geometrical (rather than growth rate) analysis.

BRIDGE TO CHAPTER III

In Chapter II, we identified a molecular marker for a Wnt producing population residing at the distal end of the regenerating fin. This population is in the intra-ray mesenchyme lineage. Intra-ray mesenchymal cells lose Snail expression and gain Dach expression as they become the Wnt producing regenerative niche that supports progenitor cells. The niche depletes when Dach$^+$ cells progressively revert back to Snail$^+$ cells. We found that the initial number of niche cells and rate of depletion act as a timing mechanism instructing when regeneration should end. Essentially, as long as progenitor cells are present, regeneration can persist. In Chapter III, I will detail how Polycomb Repressive Complex 2 and H3K27me3 maintain progenitor osteoblasts and influence cell decisions at later steps of development.

CHAPTER III

ZEBRAFISH POLYCOMB REPRESSIVE COMPLEX 2 MAINTAINS CELL STATES FOR ROBUST ORGANOGENESIS WHILE MINIMALLY PROMOTING CELL FATE SPECIFICATION

JOURNAL STYLE INFORMATION

Gabriel A. Yette, Scott Stewart, Kryn Stankunas. In Preparation. (Copyright 2019)

AUTHOR CONTRIBUTIONS

G.A.Y., S.S and K.S. designed experiments; G.A.Y. performed experiments; G.A.Y. and K. S. prepared and wrote the manuscript.

INTRODUCTION

Polycomb Repressive Complex 2 (PRC2) directs histone H3 lysine 27 (H3K27me3) methylation associated with Polycomb group (PcG)-mediated transcriptional repression. PcG was originally characterized in *Drosophila* for its conserved role maintaining Hox expression patterns and therefore segment identity (Lewis, 1978; Whitcomb, Basu, Allis, & Bernstein, 2007). Vertebrate studies, largely using mice, show PRC2 has diverse roles in body plan establishment, cell fate specification, identity maintenance, and growth control during organogenesis and homeostasis (Laugesen & Helin, 2014; Scelfo, Piunti, & Pasini, 2015). However, a unifying model how PRC2 integrates into developmental regulatory networks remain elusive. Zebrafish provide a second powerful model organism to explore core vertebrate PRC2 functions. Genetic perturbation of zebrafish Ezh2, the predominant PRC2 methyltransferase, suggest less essential roles for PRC2 in early body patterning than expected from mouse studies (San et al., 2016). However, a potentially redundant role for the alternative PRC2 methyltransferase Ezh1 is unexplored. Likewise, PRC2 roles in zebrafish organ development and maintenance, including skeletogenesis, and how those compare to those in mammals are largely unknown.

Vertebrate PRC2 comprises four core proteins, with subunits Ezh1 or Ezh2 providing H3K27 methyltransferase capability. PRC2 deposits all mono, di, or tri-methylation H3K27 marks with H3K27me3 strongly associated with PRC2-repressed genes. PRC2/H3K27me3 cooperates with PRC1 and its histone H2A mono-ubiquitin lysine 119 catalyzed marks to promote stable repression. H3K27me3 genomic landscapes vary between cells of different identities and states, largely correlating with gene repression and therefore implying PRC2 activity drives gene regulation (Scelfo et al., 2015; Yu, Lee, Oksuz, Stafford, & Reinberg, 2019). Alternatively, H3K27me3 dynamics could be driven by targeted removal by TF-dependent recruitment of Kdm6 H3K27me3 demethylases. Considering these mechanistic possibilities in developmental contexts would enable a holistic understanding how PRC2 integrates into regulatory networks including whether it instructs vs. reinforces transcriptional state.

Mammalian PRC2 studies link its function to early cell fate specification. Many fate-determining genes in embryonic stem (ES) cells exhibit a “bivalent state” of both H3K27me3 and its opposing H3K4me3 mark deposited by Trithorax group/COMPASS complexes (Bernstein et al., 2006). Upon lineage commitment, the antagonistic marks resolve in favor of either stable repression (H3K27me3) or activation (H3K4me3). Accordingly, ES cells largely fail in vitro differentiation in the absence of PRC2 (Chamberlain, Yee, & Magnuson, 2008; Ferrari et al., 2014; Lavarone, Barbieri, & Pasini, 2019; Pasini, Bracken, Hansen, Capillo, & Helin, 2007). Ezh2-null mice, and mutants in other PRC2 components, show early embryonic lethality around gastrulation, consistent with PRC2 contributing to the earliest cell specification decisions (Faust, Schumacher, Holdener, & Magnuson, 1995; O'Carroll et al., 2001; Pasini, Bracken, Jensen, Lazzerini Denchi, & Helin, 2004) .

Vertebrate PRC2 is also essential for organogenesis after the initial body plan and organ-specific cell lineages are defined. In particular, conditional loss of PRC2 using cell-type specific Cre/loxP-mediated knockouts link PRC2 function to maintaining tissue-specific progenitor pools and/or robust cell identities in disparate organs (Chiacchiera, Rossi, Jammula, Zanotti, & Pasini, 2016; Delgado-Olguín et al., 2012; Dudakovic et al., 2015; Ezhkova et al., 2011; Koppens et al., 2016; Snitow et al., 2015). However, varying conclusions from in vivo and cultured cell experiments may be clarified and expanded by comparative evaluation of conserved PRC2 functions in another vertebrate model. For example, in skeletal development, a focus herein, mouse *Ezh2* studies variably link PRC2/H3K27me3 to specification and expansion of osteoblast precursor population, osteoblast progenitor maintenance and proliferation, and differentiation into mature, bone-producing osteoblast state (Dudakovic et al., 2015; Ferguson, Devarajan, & Atit, 2018; Lui et al., 2016; Mirzamohammadi et al., 2016; Schwarz et al., 2014).

Zebrafish provide a compelling second vertebrate model to explore conceptual and mechanistic roles of PRC2. H3K27me3 marks are first detected at the time of zygotic genome activation (3 hpf) preceding gastrulation (Lindeman, Reiner, Mathavan, Aleström, & Collas, 2010; Murphy, Wu, James, Wike, & Cairns, 2018; Vastenhouw et al., 2010; Zhang et al., 2014). Homozygous *ezh2* zygotic zebrafish mutants survive to around 12 days post fertilization (hpf) before succumbing to organogenesis defects of the gut and presumably other systems (Dupret et al., 2017; San et al., 2018). Maternal *ezh2* is dispensable for early zebrafish embryogenesis (San et al., 2016). However, maternal zygotic *ezh2* mutants die around two days post fertilization with defects in eye, brain, heart and gut development. Nevertheless, they still establish a normal body plan despite greatly reduced bulk H3K27me3 (San et al., 2016).

ezh1 homozygous mutant zebrafish are viable and fertile, as are mouse *Ezh1* mutants (Ezhkova et al., 2011; Völkel et al., 2019). However, Ezh1, which shows context-dependent redundancy with Ezh2 in mice (Ai et al., 2017; Bae et al., 2015; Ezhkova et al., 2011; Koppens et al., 2016; Lui et al., 2016; Mirzamohammadi et al., 2016; X. Shen et al., 2008), may partially fulfill the PRC2 methyltransferase role during early zebrafish development. While Ezh1 is a less potent H3K27me3 enzyme (Raphael Margueron et al., 2008), embryonic stem cell studies suggest Ezh1 and Ezh2 have partially overlapping functions. Loss of Ezh2 alone largely removes global H3K27me3 (Lavarone et al., 2019; X. Shen et al., 2008). However, the remaining Ezh1-PRC2 can deposit H3K27me3 at nucleating sites (without spreading) and H3K27me1/H3K27m2 more broadly (Lavarone et al., 2019). Deletion of both Ezh1 and Ezh2 now removes all H3K27me marks with an increased number of derepressed genes (Lavarone et al., 2019).

Here, we generate and fully characterize likely null alleles of *ezh1* and *ezh2* to explore their combined roles in zebrafish early development and organogenesis, with a focus on the skeletal system. We find that Ezh2 (of either maternal or zygotic origin) and not Ezh1 (which is neither expressed normally nor compensates for Ezh2 loss) almost entirely contributes the bulk H3K27me3 and PRC2 function immediately following ZGA and through embryogenesis. These results underscore that vertebrate PRC2 is not essential for gastrulation or body plan establishment. We show PRC2 maintains dermal bone pre-osteoblasts including their proliferative state to form craniofacial elements of the correct size and shape. We correct misconceptions about a hypomorphic *ezh2* allele and use it for an allelic series unveiling homeotic phenotypes and diverse maternal/zygotic-dependent organogenesis defects upon PRC2 disruption. Collectively, our studies reinforce expectations vertebrate PRC2 has many developmental contributions. However, its major functions supporting body plan elaboration including early organogenesis are transiently concentrated immediately after zygotic genome activation with no phenotypically discernible roles at earlier phases of embryogenesis. PRC2 roles during later phases of organ development may focus on maintaining progenitor populations for organ size establishment or homeostasis.

RESULTS

Ezh2 and not Ezh1 fulfills most PRC2 roles during early embryogenesis

We explored if and how zebrafish *ezh1* and *ezh2* function divergently or redundantly, including by compensatory mechanisms. We examined *ezh1* and *ezh2* expression from one-hour post fertilization (hpf) through 5 days post fertilization (dpf) by qRT-PCR (Fig. 3.1A) and whole mount RNA *in situ* hybridization (Fig. 3.1B-G). *ezh2* was highly expressed during early stages of development compared to *ezh1*, which was undetectable until 24 hpf (Fig. 3.1A-F). *ezh2* transcripts progressively decreased while those of *ezh1* increased from 24 hpf to 120 hpf (Fig. 3.1A, D, G). We mined the Expression Atlas zebrafish RNA-Seq developmental time course data (White et al., 2017) and found a similar transition from *ezh2* to *ezh1* relative predominance (Fig. S3.1A). Importantly, and consistent with other studies, we did not detect maternal *ezh1* mRNA (Chrispijn, Andralojc, Castenmiller, & Kamminga, 2018; San et al., 2018, 2016; Sun et al., 2008; White et al., 2017), which conflicts with one report of maternally deposited *ezh1* transcripts (Völkel et al., 2019). Regardless, overlapping *ezh1* and *ezh2* expression during zebrafish development suggests Ezh1 and Ezh2 could collectively contribute to embryonic/larval PRC2. If so, loss of both PRC2 methyltransferases should enhance deleterious effects of a single mutation.

We generated *ezh1* and *ezh2* mutants by CRISPR/Cas9-targeting within or downstream of the coding region for the essential N-terminal WD40 binding domain of *ezh1* and *ezh2*, respectively (Fig. 3.1H). We isolated *ezh1* allele, *ezh1*^{b1394}, missing two bases and *ezh2* allele, *ezh2*^{b1392}, with 7 bases deleted (henceforth referred to as *ezh1*$^{-}$ and *ezh2*$^{-}$, respectively) (Fig. S3.1B, C). Both mutations produced frameshifts predicting early termination after residue 130 and residue 99 of Ezh1 and Ezh2, respectively, well before the catalytic SET domain, anticipating null alleles (Fig. 3.1H). By qRT-PCR, *ezh1*$^{-/-}$ and *ezh2*$^{-/-}$ embryos showed 40% and 25% transcript levels for the respective targeted gene than wildtype clutchmates (Fig. 3.1I-J). Decreased expression likely represented nonsense-mediated decay (NMD) of each mutant transcript, supporting that both are strong loss-of-function alleles. Further, we did not detect any Ezh2 protein in 6 dpf *ezh2*$^{-/-}$ larval extracts, reinforcing it is a null allele (Fig. 3.1K). Recent reports indicate that zebrafish mutant alleles can trigger "transcriptional adaptation", whereby NMD-produced fragments trigger upregulation of related genes that then replace lost gene function (El-Brolosy et al., 2019; El-Brolosy & Stainier, 2017; Rossi et al., 2015; Williams, Hsu, Rossi, & Artinger, 2018). However, neither our *ezh1* nor *ezh2* alleles produced compensatory expression of the corollary transcript (Fig. S3.1D, E). We conclude both alleles likely provide a clean

---

Figure 3.1 (next page). Ezh2 and not Ezh1 fulfills PRC2's relatively limited role during zebrafish embryogenesis. (A) Line graph showing relative transcript levels acquired by qRT-PCR of *ezh2* (blue) and *ezh1* (green) in wildtype embryos/larvae from 1-hour post fertilization (hpf) to 120 hpf. Transcript levels normalized to *ezh1* transcripts at 24 hpf after being normalized to *rpl8* (reference gene). (B-G) In situ hybridization for *ezh2* (B-D) and *ezh1*(E-G) at 1 hpf, 24 hpf, and 120 hpf. Scale bar = 250 µm. (H) Schematic of Ezh1/Ezh2 (756 aa, 760 aa, respectively) with green and blue asterisks denoting location of CRISPR/Cas9 mediated mutation in *ezh1* and *ezh2,* respectively. Overlaid lines show predicted translated peptides from mutated *ezh1*(green, 130 aa), and *ezh2* (blue, 99 aa). Translated peptide is identical to wildtype protein up to asterisks. Remaining peptide is mutant until early termination. (I-J) Scatter plots comparing (I) *ezh1* transcripts between wildtype and *ezh1* homozygous mutant clutchmates at three dpf and (J) *ezh2* transcripts between mutant and wildtype two-day old siblings determined by qRT-PCR. Statistical significance determined by Student's two-tailed *t*-test. *** = P-value <0.005, **** = P-value <0.0001 (K) Immunoblot of whole cell lysates from pooled 6 days post fertilization (dpf) clutchmates using antibodies against Ezh2, H3K27me3, and pan-histone H3. While there is marked decrease in H3K27me3 in *ezh2* mutants, a surprising amount of H3K27me3 remains in *ezh2*$^{-/-}$*; ezh1*$^{-/-}$ samples. (L-O) Whole mount differential interference contrast (DIC) microscopy images of *ezh2; ezh1* wildtypes and mutants at 6 dpf siblings. Red arrowhead indicating under-inflated swim bladder. Scale bar = 500 µm

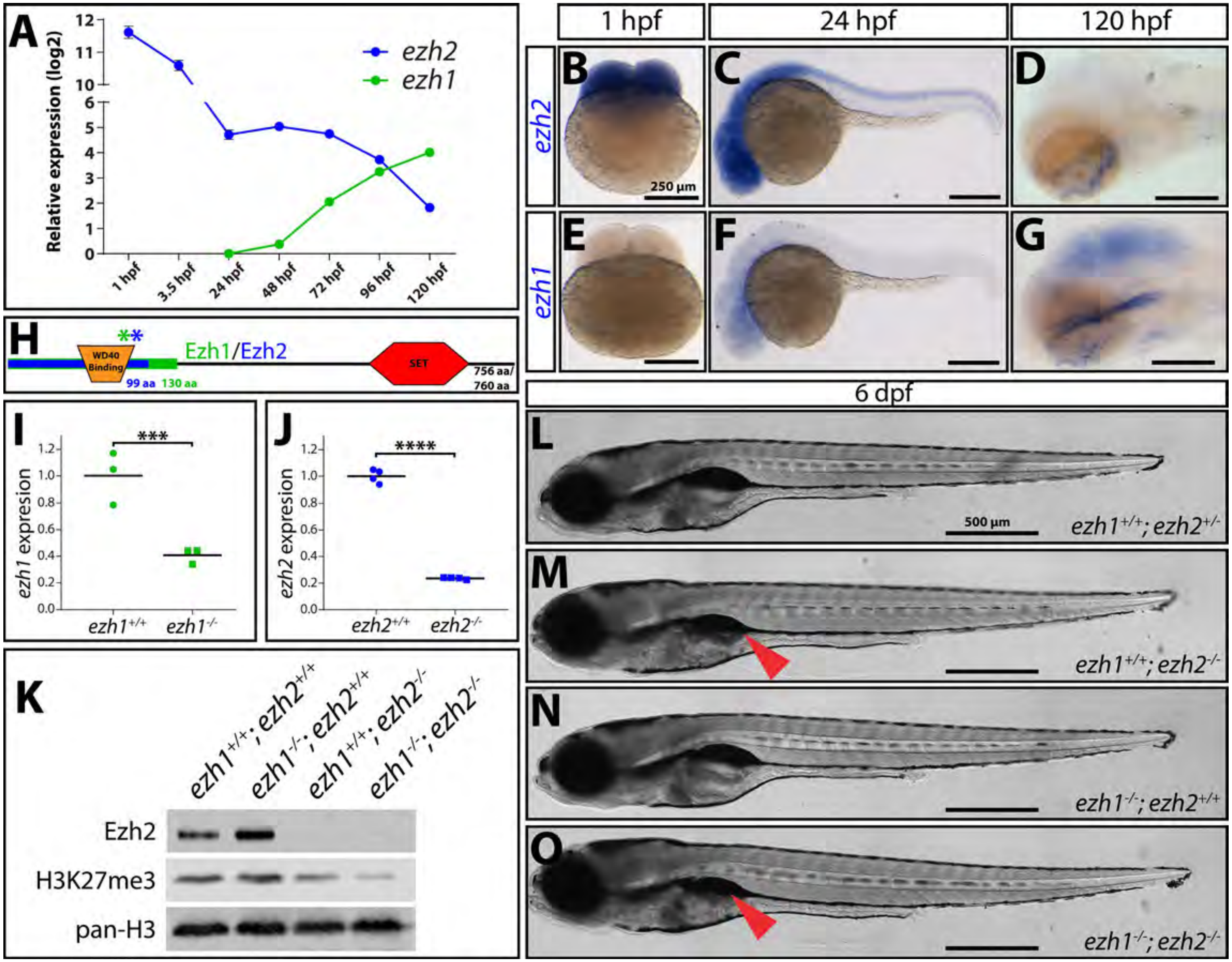
A
Relative expression (log2)
12
11
10
6
5
4
3
2
1
0
1 hpf
3.5 hpf
24 hpf
48 hpf
72 hpf
96 hpf
120 hpf
ezh2
ezh1
1 hpf
24 hpf
120 hpf
ezh2
ezh1
B
C
D
E
F
G
250 µm
H
WD40 Binding
99 aa
130 aa
Ezh1/Ezh2
SET
756 aa/
760 aa
I
ezh1 expresion
***
ezh1+/+
ezh1-/-
J
ezh2 expresion
****
ezh2+/+
ezh2-/-
1.2
1.0
0.8
0.6
0.4
0.2
0.0
K
ezh1+/+; ezh2+/+
ezh1-/-; ezh2+/+
ezh1+/+; ezh2-/-
ezh1-/-; ezh2-/-
Ezh2
H3K27me3
pan-H3
6 dpf
L
500 µm
ezh1+/+; ezh2+/-
M
ezh1+/+; ezh2-/-
N
ezh1-/-; ezh2+/+
O
ezh1-/-; ezh2-/-

loss-of-function of the respective gene and therefore double homozygous mutants would eliminate PRC2 function and H3K27me3 methylation.

We explored the relative contributions of Ezh1 and Ezh2 to embryogenesis and H3K27me3 levels by intercrossing *ezh1*$^{+/-}$*; ezh2*$^{+/-}$ fish and examining progeny of all genetic combinations. Loss of Ezh1 had no effect on bulk H3K27me3 in 6 dpf larvae (Fig. 3.1K). Consistently, and matching a previous study (Völkel et al., 2019), *ezh1*$^{-/-}$ 6 dpf larvae were indistinguishable from wildtype clutchmates and developed into viable and fertile adults (Fig. 3.1L, N). Unlike *ezh1* mutants, *ezh2*$^{-/-}$ 6 dpf larvae had markedly decreased H3K27me3 (Fig. 3.1K). Matching other *ezh2* null alleles, *ezh2*$^{-/-}$ larvae died between 7 and 14 dpf (Dupret et al., 2017; San et al., 2018, 2016). In addition, *ezh2*$^{-/-}$ 6 dpf larvae had underinflated swim bladders (Fig. 3.1M,O), a phenotype not reported but apparent in published images of homozygotes for other *ezh2* alleles (Dupret et al., 2017; San et al., 2018).

We examined *ezh1; ezh2* double homozygous mutants to define combined Ezh1 and Ezh2 developmental roles. Western blots showed *ezh1*$^{-/-}$*; ezh2*$^{-/-}$ 6 dpf larvae had further reduced bulk H3K27me3 compared to loss of *ezh2* alone (Fig. 3.1K). This confirmed the loss-of-function nature of the *ezh1* allele while demonstrating bulk H3K27me3 at 6 dpf represented the combined activity of Ezh1- and Ezh2-containing PRC2 complexes. However, *ezh1*$^{-/-}$*; ezh2*$^{-/-}$ larvae still retained some H3K27me3 (Fig. 3.1K). Given the zebrafish genome includes no other H3K27me3 methyltransferase and maternal or zygotic Ezh2 can fulfill PRC2 function before 2 dpf, we infer the residual H3K27me3 likely reflects H3K27me3 deposited by maternal Ezh2 in thereafter slowly dividing or quiescent cells.

We assessed cell type-specific H3K27me3 dependency on Ezh1- and Ezh2-containing PRC2 by immunostaining sectioned wildtype, *ezh1*, *ezh2,* and *ezh1/ezh2* homozygous mutant 6 dpf larvae for H3K27me3. H3K27me3 levels were slightly lower in cardiomyocytes and chondrocytes and more markedly reduced, but not absent, in eye, intestine, and nervous tissue making up the hindbrain/spinal cord of *ezh1*$^{-/-}$ larvae (Fig. S3.2, Fig. S3.3). In contrast, H3K27me3 levels in skeletal muscle cells were comparable to wildtype animals. H3K27me3 was undetectable in cardiomyocytes, eye, chondrocytes and gut tissues of *ezh2* zygotic-null animals (Fig. S3.2). However, H3K27me3 remained present at low levels in skeletal muscle cells and nervous tissue of *ezh2*$^{-/-}$ larvae (Fig. S3.3). H3K27me3 was nearly absent in skeletal muscle and nervous tissue of *ezh1*$^{-/-}$*; ezh2*$^{-/-}$ larvae. In both tissues, however, H3K27me3 was retained in sub-populations at low levels similar to those in *ezh2*$^{-/-}$ larvae. We conclude that zygotic Ezh2/PRC2 non-redundantly initiates H3K27me3 in cardiomyocytes, ganglion cells and cells of the inner and outer nuclear layers of the eye, chondrocytes, and intestinal cells of larval zebrafish. Nonetheless, Ezh1/PRC2 helps maintain full H3K27me3 levels nucleated by Ezh2/PRC2 in each of these cell types given bulk H3K27me3 is reduced in *ezh1* single mutants. In skeletal muscle, Ezh2 promotes most H3K27me3 with relatively minor Ezh1 contributions in some cells. In most cells of the hindbrain/spinal cord, H3K27me3 largely depends on zygotic Ezh2, with minor contribution from Ezh1. However, in certain sub-populations of both skeletal muscle and hindbrain, H3K27me3 largely deposited by maternal Ezh2/PRC2 is maintained through 6 dpf. Their minimal H3K27me3 turnover and/or dilution suggests these are quiescent cells, such as satellite cells or radial glia, set aside early in development.

ezh1$^{-/-}$*; ezh2*$^{-/-}$ larvae were outwardly indistinguishable from *ezh1*$^{+/+}$*; ezh2*$^{-/-}$ clutchmates despite the former's further reduced H3K27me3 levels (Fig. 3.1L, M). We crossed *ezh1*$^{-/-}$*; ezh2*$^{+/-}$ females to *ezh1*$^{+/-}$*; ezh2*$^{+/-}$ males to rule out any maternal Ezh1 contribution overlooked by expression studies. Larval and adult (where viable) phenotypes of all given genotypes exactly matched those generated from an *ezh1*$^{+/-}$*; ezh2*$^{+/-}$ incross (Fig. S3.1F-I). These results underscore that Ezh1 does not have a notable maternal role. We additionally conclude that Ezh2 provides all phenotypically-discernible PRC2 methyltransferase activity up to 6 dpf. Further, these H3K27me3 deposition roles are concentrated during a short window of development following zygotic genome activation when *either* maternal or zygotic Ezh2 pools can fulfill PRC2's overt roles. Ezh1's roles after its expression increases post-embryogenesis either are masked by low levels of redundant Ezh2 or are minimal in a laboratory-controlled environment.

PRC2 promotes craniofacial dermal bone shape and size by maintaining progenitor cell characteristics

Conditional PRC2 mouse studies implicate H3K27me3 dynamics in osteogenesis and skeletal formation (Dudakovic et al., 2015; Ferguson et al., 2018; Lui et al., 2016; Mirzamohammadi et al., 2016; Schwarz et al., 2014). In zebrafish, we found H3K27me3 demethylases Kdm6ba and Kdm6bb promote expansion of the basihyal craniofacial cartilage (Akerberg, Henner, Stewart, & Stankunas, 2017). Otherwise, PRC2 in the zebrafish skeletal system has not been well characterized. We first examined development of the craniofacial skeleton, which comprises endochondral and intramembranous dermal bones, in zygotic mutants of *ezh1* and/or *ezh2*. We used alcian blue and alizarin red to stain cartilage and calcified bone, respectively, of 6 dpf larvae (Fig. 3.2B-E). Flat mounts of pharyngeal arch 1 and pharyngeal arch 2 skeletal elements showed that osteoblast-derived dermal bones (the opercle and branchiostegal rays (BSR) 2 and 3) were small and malformed while chondrocyte-derived elements (cartilage) remained unchanged in *ezh2*-null larvae (Fig. 3.2C). As expected, *ezh1*$^{-/-}$ larvae had normal osteoblast- and chondrocyte-derived elements (Fig. 3.2D). We also quantified BSR3 length and found loss of *ezh2* but not *ezh1* alone significantly reduced BSR3 length (Fig. 3.2F). *ezh1*$^{-/-}$*; ezh2*$^{-/-}$ and *ezh1*$^{+/+}$*; ezh2*$^{-/-}$ larvae were grossly indistinguishable (Fig. 3.2C, 3.2E). Yet, combined *ezh1*/*ezh2* deficiency modestly further decreased BSR3 length relative to *ezh2*$^{-/-}$ larvae (Fig. 3.2F). We conclude Ezh2 is the primary zygotically- expressed H3K27me3 methyltransferase during craniofacial dermal bone formation with Ezh1 serving a minor, partially redundant role.

We pursued the cause of small, malformed pharyngeal arch 2 derived dermal bones in *ezh2*$^{-/-}$ larvae. Reduced bone could result from incomplete maturation of osteoblasts, a dearth of cranial neural crest cell-derived osteoblast specification and/or migration, or loss of a proliferative pre-osteoblast pool while the bones enlarge. Mouse embryonic stem cells and embryonic fibroblasts exhibit defective differentiation in the

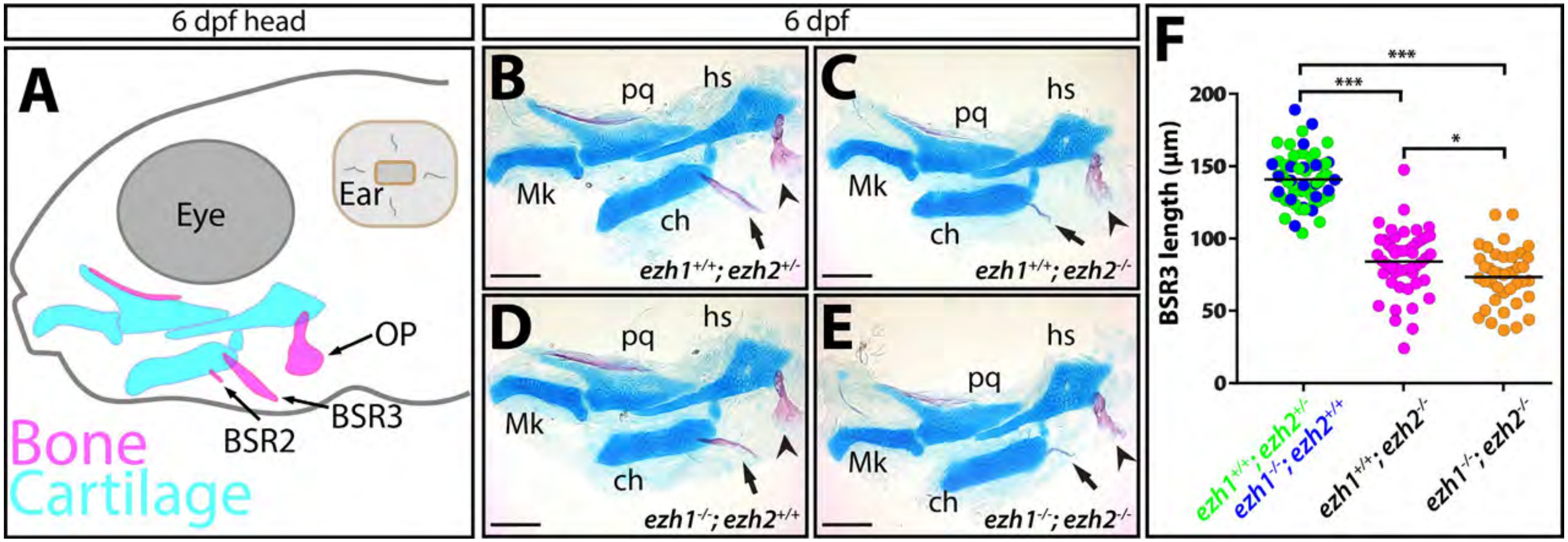

Figure 3.2. Ezh2 promotes craniofacial dermal bone formation. (A) Schematic of 6 dpf zebrafish head. Cartilaginous skeletal elements are in cyan and calcified bone is in magenta. Abbreviations: OP, opercle; BSR, branchiostegal ray. (B-E) Flat mount images of 6 dpf pharyngeal arch 1 and pharyngeal arch 2 derived skeletal elements stained with alizarin red (red) and alcian blue (blue). Arrowhead points to OP, arrow indicates BSR3. Scale bar = 100 µm. (F) Scatter plot comparing BSR3 lengths. Statistical significance determined by Student's two-tailed *t*-test. * = P-value <0.05, *** = P-value <0.001. Abbreviations: Mk, Meckel's cartilage; pq, palatoquadrate; hs, hyosymplectic; ch, ceratohyal.

absence of PRC2 (Chamberlain et al., 2008; Lavarone et al., 2019; Pasini et al., 2007). In addition, Runx2^{+} osteoblasts of the mouse calvarium fail to fully differentiate in conditional *Ezh2* mutants (Ferguson et al., 2018). If "mature" osteoblasts of *ezh2*$^{-/-}$ larvae failed to fully differentiate and produce calcified bone, we would expect to see osteoblasts presenting mature markers but no calcified matrix. We alizarin stained 6 dpf *ezh2*$^{-/-}$ larvae and wildtype clutchmates carrying the mature osteoblast reporter, *Tg(sp7:eGFP)* (DeLaurier et al., 2010). While *ezh2*-homozygous mutants had a smaller field of *sp7:eGFP*-expressing osteoblasts, those present produced calcified bone equally well as osteoblasts of *ezh2*$^{+/-}$ siblings (Fig. 3.3A, B). We conclude Ezh2 is not required for bone differentiation per se and instead promotes earlier steps in osteogenesis that generate sufficient osteoblast pools.

F**igure 3.3 (Next page). Ezh2-defecient osteoblasts are functional and do not exhibit defects in maturation.** (A-B) Live confocal imaging of *ezh2*$^{-/-}$ and wildtype 6 dpf *Tg(sp7:eGFP)* (green) fish stained with alizarin red (magenta). Red arrowhead points to BSRs, yellow arrowhead points to OP, red asterisk highlights missing BSR2 of *ezh2*$^{-/-}$ larvae. (C-D) Confocal images of *Tg(fli1a:GFP)* homozygous *ezh2* mutant and wildtype clutchmate at 28.5 hpf immunostained with antibodies against GFP (green). Insert is magnification of pharyngeal arch 2 (pa2), which is the source of cells that will become osteoblasts that form the op and BSRs. (E) Scatter plot showing equal number of pa2 cells in wildtype and *ezh2*$^{-/-}$ clutchmates at 28.5 hpf. (F-G'') Still images taken from time lapse confocal imaging of the developing opercle in *Tg(sp7:eGFP)* wildtype (F-F'') and Ezh2-deficient (G-G'') embryos. Red arrowhead points to first GFP^{+} osteoblasts. Osteoblast field outlined in yellow. (H) Scatter plot showing unchanged onset of osteoblast maturation, as assayed by GFP expression, between *ezh2* homozygous mutants and wildtype clutchmates. (I-L) Confocal immunofluorescent images of sp7:eGFP^{+} (green) and runx2:E2CRIMSON^{+} (magenta) osteoblasts of BSR3 (yellow dashed outline) and BSR2 in wildtype and *ezh2*-null 144 hpf clutchmates stained with anti-GFP and anti-DsRed antibodies. (M) Scatterplot comparing total number of BSR3 osteoblasts at 144hpf in wildtype and *ezh2*$^{-/-}$ larvae. (N) Bar graph showing similar proportions of osteoblast subtypes at 144 hpf between *ezh2* mutants and wildtype clutchmates. Error bars show one standard deviation. Statistical significance (E, H, M, N) determined by Student's two-tailed *t*-test. *** = P-value <0.005. Scale bars are 50 µm unless otherwise notated.

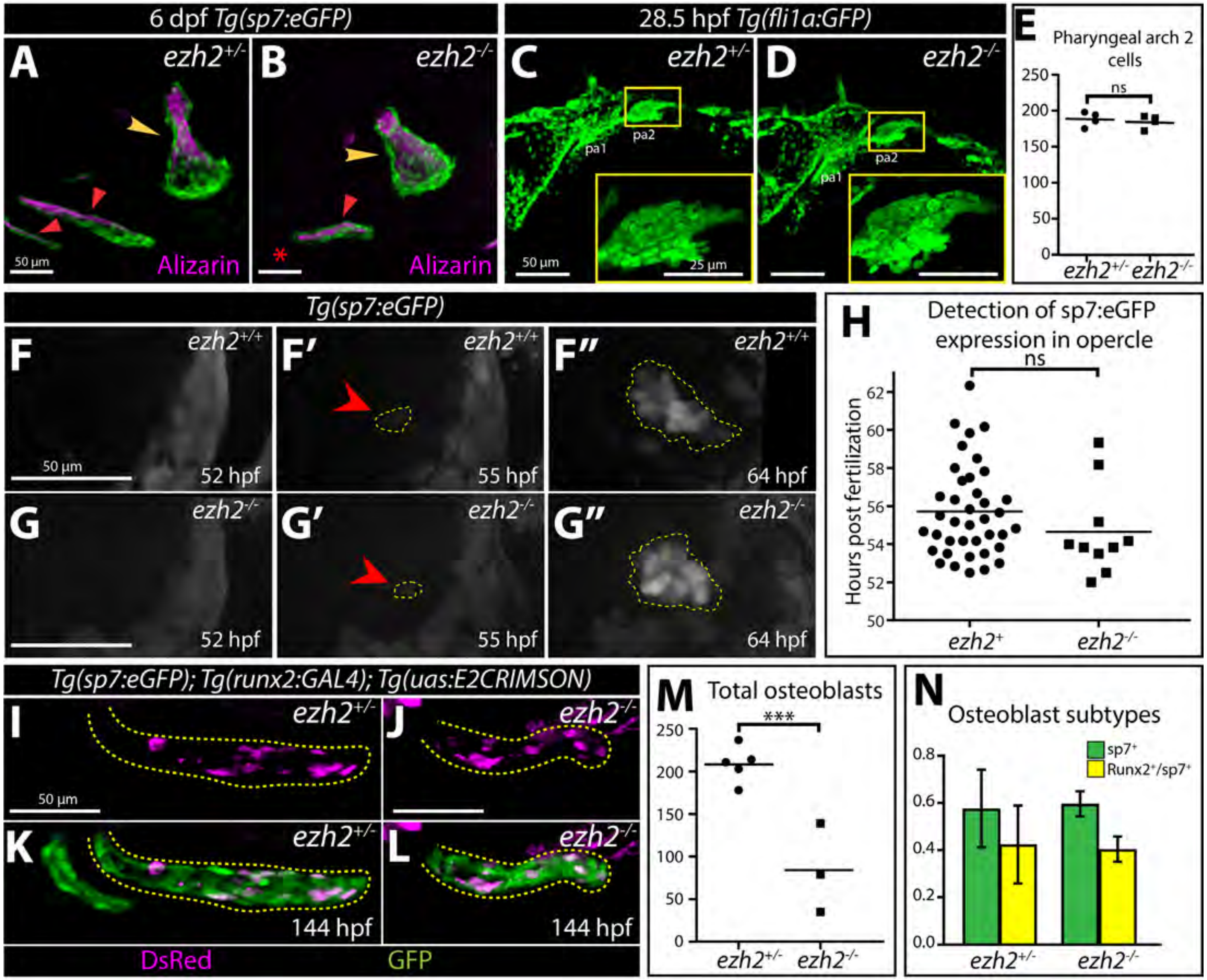
6 dpf Tg(sp7:eGFP)
A
ezh2+/-
B
ezh2-/-
50 µm
Alizarin
Alizarin
*
28.5 hpf Tg(fli1a:GFP)
C
ezh2+/-
D
ezh2-/-
pa1
pa2
pa1
pa2
50 µm
25 µm
E
Pharyngeal arch 2 cells
ns
250
200
150
100
50
0
ezh2+/-
ezh2-/-
Tg(sp7:eGFP)
F
ezh2+/+
52 hpf
50 µm
F′
ezh2+/+
55 hpf
F″
ezh2+/+
64 hpf
G
ezh2-/-
52 hpf
G′
ezh2-/-
55 hpf
G″
ezh2-/-
64 hpf
H
Detection of sp7:eGFP expression in opercle
ns
Hours post fertilization
62
60
58
56
54
52
50
ezh2+
ezh2-/-
Tg(sp7:eGFP); Tg(runx2:GAL4); Tg(uas:E2CRIMSON)
I
ezh2+/-
50 µm
J
ezh2-/-
K
ezh2+/-
144 hpf
L
ezh2-/-
144 hpf
DsRed
GFP
M
Total osteoblasts
***
250
200
150
100
50
0
ezh2+/-
ezh2-/-
N
Osteoblast subtypes
sp7+
Runx2+/sp7+
0.8
0.6
0.4
0.2
0.0
ezh2+/-
ezh2-/-

We next explored if the deficient dermal bone in the absence of *ezh2* originated from inadequate formation of the precursor progenitor osteoblast field. Dermal bone osteoblasts are derived from pharyngeal arch 2 (pa2) cranial neural crest cells (CNCCs) (Crump, Swartz, Eberhart, & Kimmel, 2006; Crump, Swartz, & Kimmel, 2004; Laue et al., 2008). *Ezh2* NCC conditional mutant mice fail to develop craniofacial bones, possibly because H3K27me3/H3K4me2 bivalent marked genes established in pre-migratory CNCCs provide key positional identity (Minoux et al., 2017). Aberrant positional identity of pre-migratory cells could disrupt their migration, ultimately resulting in defects in derived craniofacial structures. Further, *Xenopus* CNCCs migrated less with Ezh2 inhibition (Tien et al., 2015). We monitored zebrafish CNCCs using *Tg(fli1a:gfp)* (Lawson & Weinstein, 2002) to assess changes in pa2. *ezh2*$^{-/-}$ embryos had a normal sized, shaped and CNCC-populated pa2 field at 28.5 dpf (Fig. 3.3C-E). Therefore, zygotic Ezh2 promotes expansion rather than generation of osteoblast-fated pa2 CNCCs.

The net expansion of a progenitor pool depends on proliferation opposed by depletion through differentiation. Mammalian cell culture studies using adipose derived mesenchymal stem cells and MC3T3 cells showed enhanced osteoblast differentiation when EZH2/Ezh2 is inhibited (Dudakovic et al., 2016, 2015). We evaluated the effects of *ezh2* loss-of-function on pObs *in vitro* using the Ezh2-specific small molecule inhibitor EPZ-6438 (Tazemetostat) (Knutson et al., 2013) and AB9 cells. AB9 immortalized cells are derived from zebrafish fins (Paw & Zon, 1999) that we newly characterized as Runx2-expressing pObs (Fig. S3.4A-B). EPZ-6438 effectively inhibited zebrafish Ezh2 as shown by loss of bulk H3K27me3 in treated AB9 cells (Fig. S3.4D). Ezh2-inhibited AB9 cells produced elevated alkaline phosphatase when cultured in both complete and incomplete differentiation media (Fig. S3.4E-H) suggesting PRC2 has a conserved role restraining osteoblast maturation.

Our finding that Ezh2 opposes osteoblast maturation *in vitro* suggested that *ezh2*$^{-/-}$ embryos might show premature differentiation of osteoblasts *in vivo*. To test this, we used live time-lapse imaging of *sp7:eGFP* embryos from 52 to 72 hpf to monitor the onset of *sp7* expression in opercle osteoblasts (Fig. 3.3F-G, Supp movie 3.1). *ezh2*$^{-/-}$ and control clutchmates first showed sp7-positive cells around 55 hours post fertilization at the dorsal point of the opercle (Fig. 3.3F-H). However, the osteoblast field of Ezh2-deficient animals did not expand as extensively (Fig. 3.3F'', G'', Supp. Movie 3.1, Supp. Movie 3.2). Between two and three dpf, the field of wildtype sp7^{+} osteoblasts at the dorsal point of the opercle extended ventrally. Osteoblasts at the ventral end of the OP normally expand along the anteroposterior axis between 4 and 5 dpf (Brinkley et al., 2016; Eames et al., 2013). However, between two and three dpf some *ezh2*-null osteoblasts appeared stuck at the dorsal end of the opercle, first expanding along the anteroposterior axis, thereby thickening the dorsal point of the OP, before stretching ventrally (Fig. 3.3G'', Supp. Movie 3.1). We examined if *ezh2*$^{-/-}$ larvae had similar osteoblast migration abnormalities during BSR3 development. Between three and four dpf, BSR3-forming osteoblasts begin to express sp7 near the ceratohyal and then extend posteriorly. In *ezh2*$^{-/-}$ larvae, the BSR3 osteoblast field resembled that of the opercle by remaining fairly stagnant and failing to fully extend (Supp. Movie 3.2). Therefore, while Ezh2-devoid osteoblasts did not precociously express sp7, their deficient collective motility could represent a loss of progenitor characteristics. We conclude that zygotic Ezh2 is dispensable for osteoblast specification and maturation but is required for pre-osteoblast migration and expansion.

Loss of zygotic Ezh2 did not affect pharyngeal arch 2 populations at one dpf, onset of sp7 expression at two days post fertilization, or osteoblast calcification abilities. Osteoblast migration defects seen at two and three dpf likely contributed to shortened bones, but they do not explain the decrease in total osteoblasts at 6 dpf. Therefore, we explored two possibilities for *ezh2*$^{-/-}$ intramembranous bone deficiency: Runx2^{+} pre-osteoblasts were lost at a greater rate and/or osteoblast were less proliferative. We first examined proportions of osteoblast subtypes by monitoring *Tg(runx2:GAL4); Tg(uas:E2CRIMSON)* and *Tg(sp7:eGFP)* expression in BSR3 at 6 dpf. We found, while *ezh2*-null mutants had fewer total osteoblasts, they had similar proportions of osteoblast subpopulations as wildtype clutchmates (Fig. 3.3 I-N). Next, we examined if a failure to sustain pOb proliferation could underlie the reduced osteoblasts and thereby contribute to the *ezh2*$^{-/-}$ small bone phenotype. We treated *Tg(sp7:eGFP); ezh2*$^{-/-}$ and clutchmate larvae with EdU from 96 hpf to 98 hpf to assess osteoblast proliferation (Fig. 3.4A-D). In both mutant and control clutchmates, EdU incorporated more readily in osteoblasts at the medial to posterior aspect of BSR3. However, *ezh2*$^{-/-}$ larvae had half as many EdU-positive osteoblasts as their wildtype siblings (Fig. 3.4E). Since we did not see fewer cranial neural crest cells, premature differentiation or increased rate in osteoblast maturation, we conclude decreased proliferation is the likely cause of fewer osteoblasts and smaller dermal bones of *ezh2* mutants.

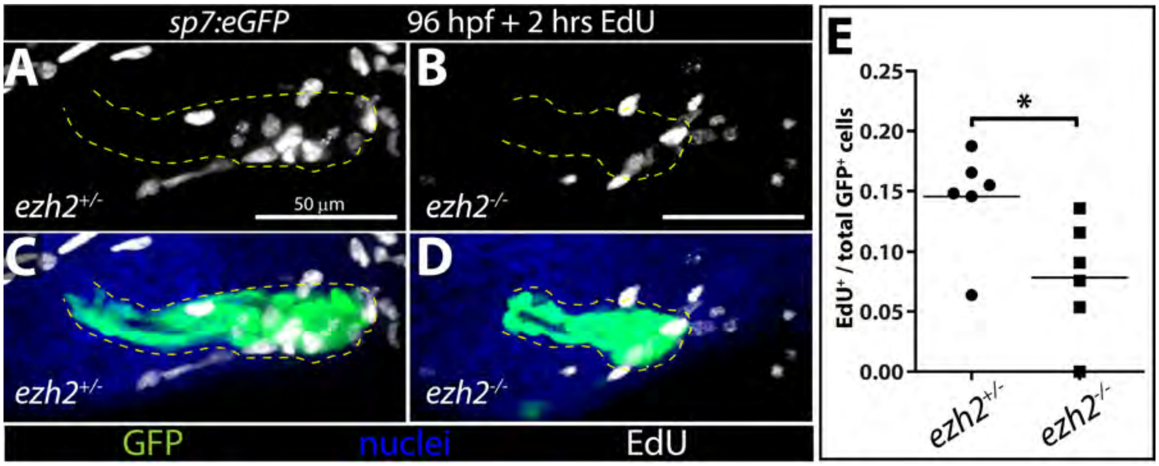

Figure 3.4. Ezh2 promotes osteoblast proliferation. (A-D) Max projection confocal images of whole mount *Tg(sp7:eGFP)*; *ezh2* wildtype (A and C) and homozygous mutant (B and D) larvae at 98 hpf stained for EdU incorporation (grey, proliferation) and GFP (green, osteoblasts). BSR3 osteoblasts are outlined in yellow. (E) Scatterplot showing percentage of EdU positive BSR3 osteoblasts (A-D, outlined in yellow) of 98 hpf control and *ezh2*$^{-/-}$ larvae treated with EdU for 2 hours. P- value is from a two-tailed Student's *t*-test. * = P-value < 0.05.

ezh2^{sa1199} is a hypomorphic allele uncovering vertebrate PRC2 homeotic functions and enabling post-larval stage studies

PcG mutants in flies, mice, and plants exhibit homeotic transformations whereby a body structure assumes the identity of an analogous but posteriorly-displaced structure due to Hox gene misexpression (Whitcomb et al., 2007). For example, in *Drosophila,* mutations of *esc* (Eed in vertebrates) can develop legs in place of antennae (Glicksman & Brower, 1988; Slifer, 1942). Yet, in zebrafish this phenomenon has not been reported, presumably due to early lethality of PcG mutants (Dupret et al., 2017; San et al., 2018, 2016; van der Velden, Wang, van Lohuizen, & Haramis, 2012) or dispensability of individual PcG genes from redundancy (Dupret, Völkel, Le Bourhis, & Angrand, 2016; Völkel et al., 2019). We isolated the *ezh2*^{sa1199} allele through extensive outcrossing to rid the background of unknown linked mutations that led to lethality around three dpf, as independently reported (San et al., 2019). We were surprised to find that fish homozygous for *ezh2*^{sa1199} allele, previously described as a null (Zhong, Ye, Chen, Wang, & Wang, 2018), did not present malformed BSRs or opercles at 6 dpf (Fig. 3.5A-B). The *ezh2*^{sa1199} lesion is a nonsense point mutation at codon 18 that should produce no or non-functional protein. However, we noticed a potential internal translation start site (TSS) near the lesion site at Ezh2 Met24 (Fig. S3.5A). If translation initiated from this alternative TSS, we would predict a truncated, yet, functional protein with an intact WD40 binding domain and catalytic SET domain. We predicted the majority of translation from *ezh2*^{sa1199} initiated at Met1, given the nearly perfect Kozak sequence (Fig. S3.5A), and terminated at the early stop at codon 18. We further predicted that some translation would initiate at Met24 resulting in a slightly smaller, and less abundant protein. By immunoblotting, we found Ezh2 from *ezh2*$^{sa1199/sa1199}$ fish was of lower molecular weight and produced at reduced levels (Fig. 3.5C). Concordantly, *ezh2*$^{sa1199/sa1199}$ fish showed greatly reduced H3K27me3 (Fig. 3.5C). Additionally, qRT-PCR showed elevated *ezh2* transcripts in fish containing *ezh2*^{sa1199}, indicating that transcripts derived from this allele are not subject to nonsense mediated decay and rather are stabilized or transcribed at a higher rate than the wildtype allele (Fig. S3.5H). Further, *ezh2*$^{sa1199/sa1199}$ fish survived to adulthood at near expected ratios (Fig. 3.5D), albeit with developmental defects including a notable “open mouth” phenotype and fewer bony rays in the anal and pelvic fins (Fig. 3.5E-G, Supp Fig. S3.5B-C). Taken together, these data indicate that *ezh2*^{sa1199} is a hypomorph capable of supporting early development.

While we observed slight changes in appendage morphology in *ezh2*$^{sa1199/sa1199}$ adults, we did not see overt homeotic transformations described in other organisms bearing

PRC2 mutations. Appreciating *ezh2*^{sa1199} as a hypomorph, we produced an allelic series to look for more severe body layout defects in *ezh2*$^{sa1199/-}$ adults. By alizarin red staining, *ezh2*$^{sa1199/-}$ fish had fewer bony rays in their pelvic and anal fins, similar to *ezh2*$^{sa1199/sa1199}$ adults, and caudal fin (Fig. S3.3F-G). 30% of *ezh2*$^{sa1199/-}$ fish lacked pelvic fins and pelvic girdle altogether. Further, *ezh2* transheterozygous fish were missing a rib with the most proximal pre-caudal vertebra assuming a more caudal-like identity (Fig. 3.5H-I). Similar transformations in vertebrae identity are observed in mice with mutations in PRC1 genes

Figure 3.5 (next page). ***ezh2***^{sa1199} **hypomorph allele bypasses early lethality with mild defects.** (A-B) Live confocal imaging of wildtype and *ezh2*$^{sa1199/sa1199}$ 6 dpf *Tg(sp7:eGFP)* (green) larvae, from an *ezh2*$^{+/sa1199}$ incross of adults that had been extensively outcrossed to remove linked mutations, stained with alizarin red (magenta). BSRs (red arrowheads) and op (yellow arrowhead) are indistinguishable between homozygous mutants and wildtype clutchmates. Scale bar = 50 µm. (C) Immunoblots on whole cell lysates from 3-day post amputation caudal fin regenerates using Ezh2, H3K27me3, and pan-histone H3 antibodies showing reduced, in size and abundance, Ezh2 in *ezh2*$^{sa1199/sa1199}$ adults. Blue arrow indicating wildtype Ezh2 size, while green arrow points to slightly smaller Ezh2 protein translated from *ezh2*^{sa1199} transcripts. (D) Survival table of adult fish from an *ezh2*$^{+/sa1199}$ incross. (E-G) 5-month-old wildtype and *ezh2*$^{sa1199/sa1199}$ clutchmates. Arrows pointing to anal and pelvic fins. Arrowhead pointing to lower jaw. Scale bar = 5 mm. (H-I) Alizarin red (red) staining of adult (H) *ezh2*$^{+/sa1199}$ and (I) transheterozygous clutchmates at 4 months post fertilization. Arrowhead highlighting loss of precaudal vertebrae identity in *ezh2*$^{sa1199/-}$ adults. Arrows showing decrease number of bony rays in anal and pelvic fins. Blue oval circumscribes reduced pelvic girdle. (J-K) In situ hybridization for *hoxa9b* (blue) in wildtype and *ezh2*$^{-/-}$ 48 hpf clutchmates. Blue bar indicates extent of *hoxa9b* expression in wildtype embryos. Red bar shows mild anterior expansion of *hoxa9b* expression in homozygous mutants. Dotted vertical line demarcates anterior boundary of *hoxa9b* expression. (L-M) Confocal imaging of live ezh2$^{+/sa1199}$ and ezh2$^{sa1199/-}$ 6 dpf *Tg(sp7:eGFP)* (green) larvae stained with alizarin red (magenta). Scale bar = 50 µm. (N) Scatterplot showing consistent reduction in BSR3 length of *ezh2*$^{sa1199/-}$ larvae compared to wildtype clutchmates at 6 dpf. Statistical significance determined by two tailed Student's *t*-test. **** = P-value <0.0001.

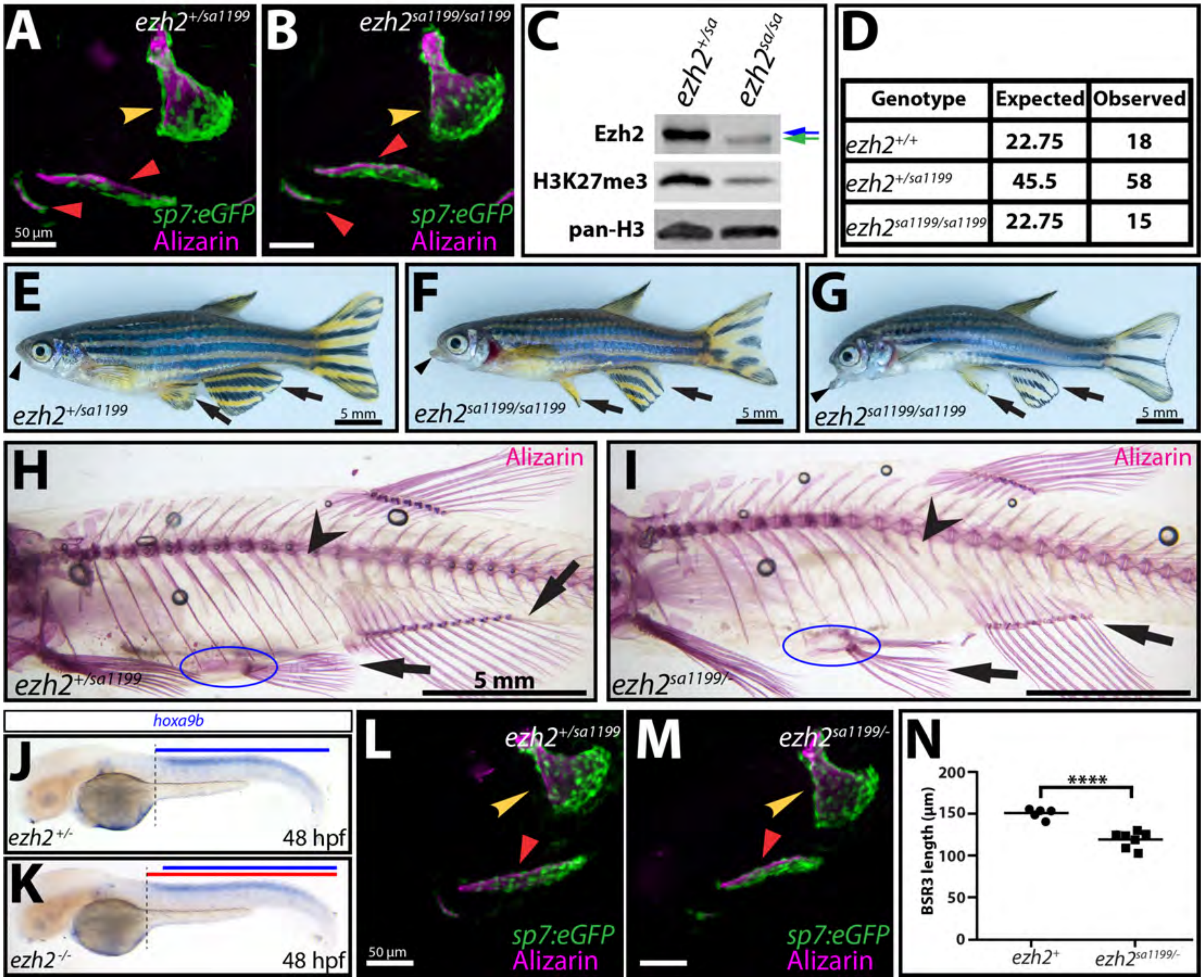

Genotype	**Expected**	**Observed**
ezh2$^{+/+}$	**22.75**	**18**
ezh2$^{+/sa1199}$	**45.5**	**58**
ezh2$^{sa1199/sa1199}$	**22.75**	**15**

(Akasaka et al., 1996; Coré et al., 1997; Courel, Friesenhahn, & Lees, 2008; Isono et al., 2005; Katoh-Fukui et al., 1998; Suzuki et al., 2002; van der Lugt et al., 1994) and in an *Eed* hypomorph (Shumacher, Faust, & Magnuson, 1996). These homeotic phenotypes are often accompanied with anterior misexpression of posterior hox genes. Zebrafish *rnf2* (PRC1 subunit) mutants (van der Velden et al., 2012) and $MZezh2^{hu5670/hu5670}$ (Rougeot et al., 2019; San et al., 2016) exhibit anterior expansion of the posterior hox gene, *hoxa9b*. Accordingly, RNA in situ hybridization experiments showed modest anterior expansion of *hoxa9b* in $ezh2^{-/-}$ embryos (Fig. 3.5J-K).

We reasoned since *ezh2* transheterozygous adults had more severe defects than $ezh2^{sa1199/sa1199}$ fish, they likewise would present with more severe developmental defects. We stained 6 dpf $ezh2^{sa1199/-}$; *Tg(sp7:eGFP)* and wildtype clutchmates with alizarin red, finding shortened BSR3s in the transheterozygotes (Fig. 3.5L, M). Likewise, $ezh2^{sa1199/-}$; *Tg(sp7:eGFP)* larvae consistently had slightly smaller opercles with moderately wider OP necks than wildtype larvae (Fig. 3.5L-N). We took advantage of $ezh2^{sa1199/-}$ survivors to assess late larval cranial calcification. Wildtype three-week post fertilization larvae showed extensive alizarin red-labeled mineralization of the cranium, in stark contrast to near absent alizarin staining in transheterozygotes (Fig. S3.5D-E). Reduced calcification is consistent with fewer craniofacial dermal osteoblasts observed in zygotic *ezh2*-null larvae.

The additional axial skeleton and fin patterning defects in adults and exacerbated craniofacial defects at 6 dpf of *ezh2* transheterozygotes further demonstrate that $ezh2^{sa1199}$ is a hypomorph. This allele allows for investigation of post larval roles of Ezh2 and affords a second vertebrate model to study mechanisms of Polycomb maintenance of segmented Hox gene expression.

Major Ezh2/PRC2 pleiotropic organogenesis functions are concentrated immediately after maternal/zygotic transition

Maternal zygotic *ezh2* null progeny generated by germline transplantations have poorly formed liver, pancreas, brain, and eyes, and a "stringy heart", dying around two dpf (San et al., 2016). Since *ezh2*$^{sa1199/sa1199}$ fish survived to adulthood with only mild defects, we hypothesized that *ezh2*^{sa1199}, while maintaining enough function to facilitate mostly normal development, may generate maternal zygotic mutants manifesting phenotypes similar to those previously described.

We crossed *ezh2*$^{sa1199/sa1199}$ females to *ezh2*$^{+/-}$ males and reared offspring until 6 dpf (Fig. 3.6, Fig. S3.6). Many defects in these *ezh2* maternal-zygotic mutants (hereafter referred to as *M*^{sa1199}*Zezh2*$^{sa1199/-}$) corresponded with previous findings (San et al., 2016). Consistently, we also found zygotic wildtype Ezh2 was sufficient to fully rescue maternal zygotic mutant defects (Fig. 3.6, Fig. S3.6). Defects first manifested at two dpf, unlike null maternal-zygotic mutants that exhibited defects as early as one dpf. *M*^{sa1199}*Zezh2*$^{sa1199/-}$ embryos had decreased body length and reduced yolk extension at two dpf. About 25 percent of mutants had heart edemas at 48 hpf, with all showing edemas by 56 hpf (Fig. S3.6A-C). By 72 hpf, *M*^{sa1199}*Zezh2*$^{sa1199/-}$ embryos exhibited extreme cardiac edema associated with greatly elongated hearts lacking distinct atrium and ventricle chambers, similar to the stringy heart described in null maternal zygotic mutants (San et al., 2016)

(Fig. 3.6C-D). The eyes were notably smaller. From four dpf to 6 dpf, edema spread to the rest of the body cavity and additional defects became more apparent. The intestinal bulb was absent and there was no clear swim bladder (Fig. S3.6D-G). *M*^{sa1199}*Zezh2*$^{sa1199/-}$ intestinal cells appeared compact instead of adopting their regular long columnar shape and organization. Similar to the heart, the liver was elongated and lost its bilateral configuration (Fig. S3.6H-J). The pancreas appeared small and underdeveloped (Fig. S3.6H-J). Skeletal muscle fibers were wavy in appearance, which was not described in previous maternal zygotic mutants presumably because complete maternal zygotic *ezh2*-null fish die before this defect could be observed (Fig. S3.6E, G).

Figure 3.6 (next page). *ezh2*^{sa1199} is sufficiently defective to cause maternal-zygotic defects. (A-B) Wholemount DIC images of three dpf siblings from a ♀ *ezh2*$^{sa1199/sa1199}$ x ♂ *ezh2*$^{+/-}$ cross. Zygotic wildtype *ezh2* rescues (A) defects present in maternal-zygotic mutants (B). Arrow points to severe cardiac edema. Black arrowhead indicating absent yolk extension. Magenta arrowheads point to position of ceratohyal cartilage. White dashed ovals encircle eyes. Scale bar is 500 µm. (C-D) Magnified DIC images of hearts from animals in (A) and (B). Hearts are outlined in dashed white line. (C) *ezh2*$^{+/sa1199}$ have well-defined atrium and ventricle (abbreviated with "A" and "V", respectively) compared to (D) *M*$^{sa1199/sa1199}$ zygotic transheterozygotes that present with extended hearts, lacking distinct chamber identity. Scale bar is 250 µm. (E) Immunoblot using Ezh2, H3K27me3, and pan-histone H3 antibodies on whole cell lysates from pooled maternal *ezh2* mutant clutchmates at three dpf. (F-N) Flat mounts of alizarin red (red, ossification-osteoblast derived) and alcian blue (blue, cartilage- chondrocyte derived) stained skeletal elements from maternal-zygotic *ezh2* mutants and wildtype clutchmates at 6 dpf. Pharyngeal arch 1 and 2 derived elements developed normally in zygotic wildtype larvae (F, I). Transheterozygous clutchmates (G, H, J, K) presented with multiple fusions of cartilaginous elements and lacked nearly all ossification. Black arrows point to BSRs. Black arrowhead points to opercle. Asterisks denote lost osteoblast derived elements. Red arrows point to fusions between chondrocyte derived elements. Magenta arrowhead points to ectopic growth of anterior process of ceratohyal. Abbreviations: Mk, Meckel's cartilage; pq, palatoquadrate; ptp, pterygoid process; hs, hyosymplectic; ch, ceratohyal. Scale bar is 100 µm. (L-N) Ceratobranchial 4 and 5 and pharyngeal teeth of wildtype and maternal-zygotic mutant clutchmates. Red arrowhead points to pharyngeal teeth, which poorly form in mutant larvae (M-N). Abbreviations: cb, ceratobranchial. Scale bar is 100 µm.

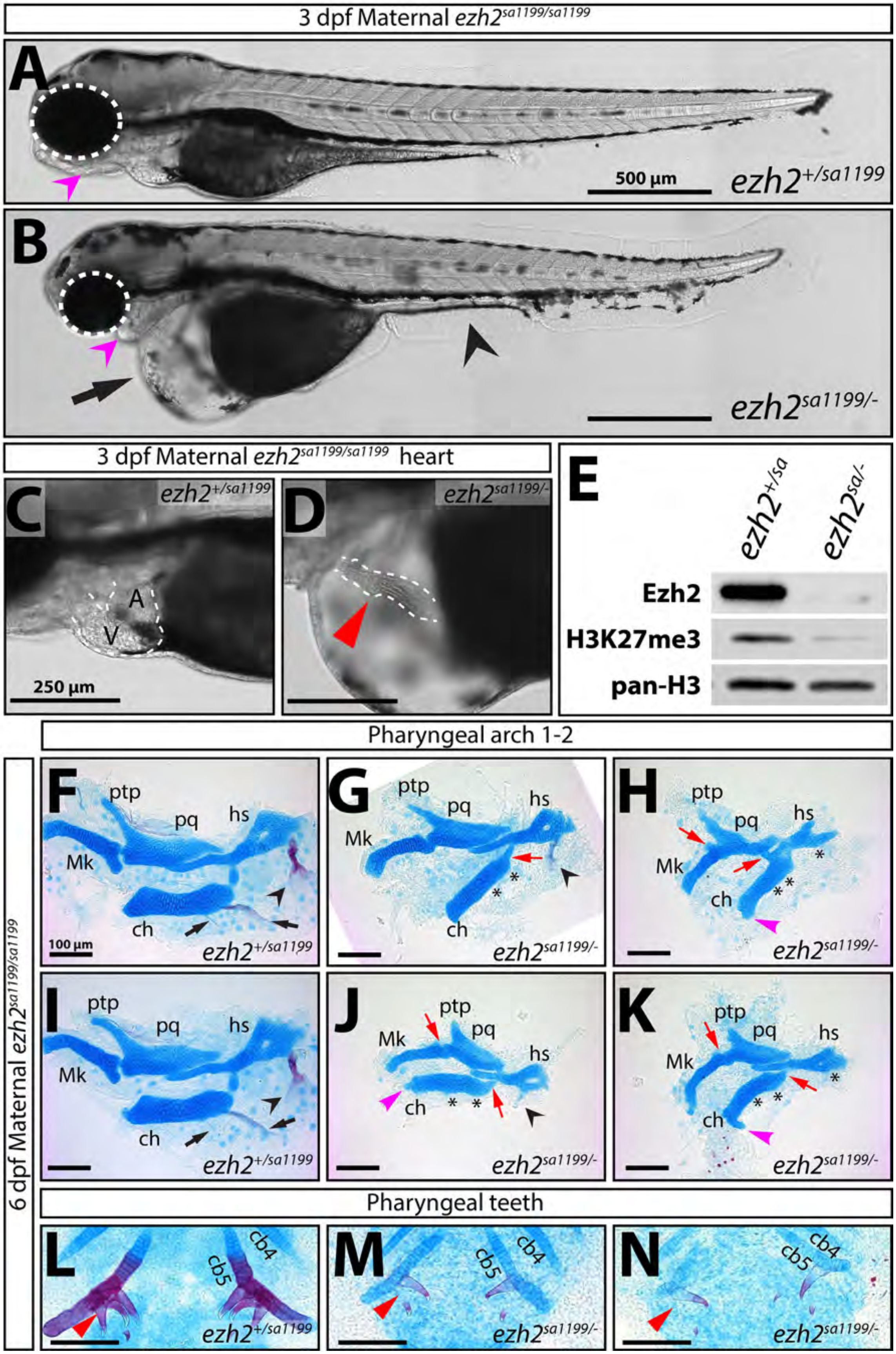
3 dpf Maternal $ezh2^{sa1199/sa1199}$
A
500 µm
$ezh2^{+/sa1199}$
B
$ezh2^{sa1199/-}$
3 dpf Maternal $ezh2^{sa1199/sa1199}$ heart
C
$ezh2^{+/sa1199}$
A
V
250 µm
D
$ezh2^{sa1199/-}$
E
$ezh2^{+/sa}$
$ezh2^{sa/-}$
Ezh2
H3K27me3
pan-H3
Pharyngeal arch 1-2
6 dpf Maternal $ezh2^{sa1199/sa1199}$
F
ptp
pq
hs
Mk
ch
100 µm
$ezh2^{+/sa1199}$
G
ptp
pq
hs
Mk
ch
$ezh2^{sa1199/-}$
H
ptp
pq
hs
Mk
ch
$ezh2^{sa1199/-}$
I
ptp
pq
hs
Mk
ch
$ezh2^{+/sa1199}$
J
ptp
Mk
pq
hs
ch
$ezh2^{sa1199/-}$
K
ptp
pq
hs
Mk
ch
$ezh2^{sa1199/-}$
Pharyngeal teeth
L
cb4
cb5
$ezh2^{+/sa1199}$
M
cb5
cb4
$ezh2^{sa1199/-}$
N
cb4
cb5
$ezh2^{sa1199/-}$

$M^{sa1199}Zezh2^{sa1199/-}$ embryos have similar pleiotropic organogenesis defects less severe than those of $MZezh2^{hu5670/hu5670}$ embryos but more severe than $ezh2^{-/-}$ larvae. We detected low levels of Ezh2 in whole cell lysates of 3 dpf $M^{sa1199}Zezh2^{sa1199/-}$ larvae at a slightly lower molecular weight than zygotic wildtype clutchmates (Fig. 3.6E). Correspondingly, there is a substantial decrease in H3K27me3 (Fig. 3.6E). Residual Ezh2^{sa1199} protein and activity likely results in less severe defects of $M^{sa1199}Zezh2^{sa1199/-}$ larvae compared to *MZezh2*-nulls. In comparison, Ezh2 is undetectable and H3K27me3 is decreased in zygotic *ezh2*-nulls at 6 dpf (Fig. 3.1K), yet they only present with mild defects (Fig. 3.1M). This, along with the absence of phenotypes in $M^{sa1199}Zezh2^{+/sa1199}$ larvae (Fig. 3.6, Fig. S3.6) highlight PRC2's most critical functions are immediately after zygotic genome activation.

$M^{sa1199}Zezh2^{sa1199/-}$ embryos developed an abnormally shaped head. In addition to smaller eyes, the mouth protruded less and the ceratohyal and ceratobranchial elements were shifted more ventral and caudal than in $M^{sa1199}Zezh2^{+/sa1199}$ clutchmates (Fig. 3.6A-B, Fig. S3.6D-G), suggesting additional craniofacial defects not observed in $ezh2^{-/-}$ larvae. We stained 6 dpf larvae from $ezh2^{sa1199/sa1199}$ female to $ezh2^{+/-}$ male crosses with alcian blue and alizarin red to observe cartilaginous and calcified elements, respectively. Maternal mutant but zygotic heterozygotes resembled wildtype animals with no defects in pharyngeal arch one and two derived elements (Fig. 3.6F, I). In contrast, $M^{sa1199}Zezh2^{sa1199/-}$ fish had little alizarin red staining. Their BSRs were completely absent and opercles were missing or diminished (Fig. 3.6G-H, J-K). Osteoblast derived pharyngeal teeth were also underdeveloped (Fig. 3.6L-N, Fig. S3.7A-D).

Unlike zygotic $ezh2^{-/-}$ larvae that lacked defects in the cartilaginous skeleton, $M^{sa1199}Zezh2^{sa1199/-}$ fish presented with fusions between many mandibular and hyoid elements. The pterygoid process of the palatoquadrate did not extend, giving it a short stubby appearance. The ceratohyal had abnormal growth where it articulated with the basihyal (Fig. 3.6G-H, J-K). In addition, the anterior end of the basihyal did not form its typical fan-like shape (Fig. S3.7A-D). We earlier described how zygotic loss of Ezh2 results in misshapen bones because of loss of pre-osteoblast progenitor characteristics. However, the profound decrease in calcified elements and cartilaginous fusions in $M^{sa1199}Zezh2^{sa1199/-}$ embryos suggests either more extensive progenitor cell depletion or that drastic reduction in maternal Ezh2 additionally disrupts osteoblast and chondrocyte specification.

The residual H3K27me3 in 3 dpf $M^{sa1199}Zezh2^{sa1199/-}$ embryos detected by Western blot could reflect remaining activity of the truncated $Ezh2^{sa1199}$ protein or Ezh1. We immunostained 3 dpf larval maternal-zygotic mutants and zygotic wildtype clutchmates with antibodies against H3K27me3 as well as MF20 (Myosin heavy chain) and pan-cadherin to accentuate changes in tissue organization. We examined gut, eye, skeletal muscle, spinal cord, chondrocytes and heart (Fig. S3.8). H3K27me3 was absent in all observed tissues. Combined with our genetic studies, this result underscore several key conclusions: 1) the $ezh2^{sa1199}$ allele is a near null at the level of protein activity, 2) Ezh1 provides little H3K27me3 activity up to 3 dpf and is unable to even minimally replace zygotic Ezh2 when maternal Ezh2 is also missing, 3) minimal – undetectable – PRC2 activity and H3K27me3 is required for body plan and expansion, but not initial establishment, of most organs, and 4) once past a critical window for PRC2 function that can be provided by maternal Ezh2, a minute amount of Ezh2-provided PRC2 and resulting bulk H3K27me3 are sufficient for near normal development to adulthood.

DISCUSSION

We comprehensively explore genetic contributions of zebrafish Ezh2 and Ezh1 H3K27me3 methyltransferases to reveal core vertebrate PRC2 roles and strengthen the framework for zebrafish PcG research. We show Ezh2 uniquely provides major PRC2-activities during embryogenesis with only minor, redundant and non-compensatory contributions by non-maternally deposited Ezh1. Ezh1 is not required for viability or fertility despite progressively supplanting Ezh2 expression after embryogenesis. Our study further confirms PRC2 roles become essential only after gastrulation and body plan establishment. Further, either maternal or zygotic Ezh2 can provide early embryonic PRC2 function. Therefore, PRC2-driven H3K27me3 landscapes appear particularly important immediately after zygotic genome activation. Nonetheless, PRC2 is dispensable for gastrulation and body plan establishment, consistent with the onset of detectable H3K27me3 after ZGA (Lindeman et al., 2010; Murphy et al., 2018; Vastenhouw et al., 2010; Zhang et al., 2014) and a maintenance rather than instructive role for PcG-mediated repression in cell fate determination.

We show how abnormally sized and shaped dermal bone craniofacial skeletal elements in *ezh2* zygotic nulls originate from reduced proliferation and disrupted migration of progenitor osteoblasts, which otherwise are specified normally and can differentiate into bone-producing cells. These observations support the emerging general concept that PRC2 maintains progenitor states for organ size and homeostasis. We correct misconceptions about the *ezh2*^{sa1199} allele by showing how its predicted nonsense and null lesion instead produces a severe hypomorph due to faint internal translation initiation. Finally, we produce an *ezh2* allelic series revealing additional Ezh2-PRC2 organogenesis roles and uncovering axial skeletal homeotic transformations upon zebrafish PcG disruption.

Ezh1 is dispensable for zebrafish development and cannot substitute for Ezh2/PRC2

We confirm reports *ezh2* is maternally deposited and highly expressed throughout the first five days of zebrafish development (Chrispijn et al., 2018; San et al., 2018, 2016; Sun et al., 2008; White et al., 2017). *ezh2* expression then progressively decreases through larval development. In contrast, *ezh1* is not maternally contributed. Contrasting one report (Völkel et al., 2019), we and others did not detect *ezh1* transcripts before zygotic genome activation (Chrispijn et al., 2018; San et al., 2018, 2016; Sun et al., 2008; White et al., 2017). Zygotic *ezh1* expression steadily increases from one to five dpf, exceeding *ezh2* expression by 4 dpf (Chrispijn et al., 2018; San et al., 2018, 2016; Sun et al., 2008; White et al., 2017). These *ezh2* and *ezh1* expression profiles are consistent with Ezh2 serving as the primary H3K27me3 methyltransferase in progenitor and highly proliferative cells whereas Ezh1 typically assumes the H3K27me3 maintenance role in mature cell populations (Ezhkova et al., 2009; Raphael Margueron et al., 2008).

While *ezh2*$^{-/-}$ fish die around two weeks post fertilization, *ezh1*$^{-/-}$ animals are viable and fertile, consistent with mouse and previous zebrafish studies (Ezhkova et al., 2011; Völkel et al., 2019). Ezh1 therefore does not have notable, unique developmental roles. Ezh2 may substitute for Ezh1 at later life stages in spite of its relatively lower expression. In contrast, embryonic lethality of *ezh2* single homozygous mutants shows that Ezh1 cannot fully accommodate PRC2 functions (San et al., 2016). We now show that *ezh1; ezh2* double mutants have nearly identical phenotypes as *ezh2* single mutants, including in near absence of maternal *ezh2*. This could reflect distinct *ezh1* and *ezh2* temporal expression patterns. *ezh2* always co-expresses with *ezh1* while *ezh1* only coincides with *ezh2* after one dpf. Alternatively, Ezh1/PRC2 and Ezh2/PRC2 may have distinct biochemical activities. Ezh1 and Ezh2 are equally capable of depositing H3K27me1 (Lavarone et al., 2019; C.-H. Lee, Holder, et al., 2018). However, Ezh2 is a superior H3K27me2/3 methyltransferase, especially in the presence of cofactors and allosteric activators (Lavarone et al., 2019; C.-H. Lee, Holder, et al., 2018; C.-H. Lee, Yu, et al., 2018). Further, Ezh2/PRC2 complexes may have unique ability to catalyze spreading of H3K27me3 marks across broad chromatin domains from nucleating centers (Lavarone et al., 2019).

ezh2^{sa1199} **is a hypomorph useful for maternal studies and uncovering additional PRC2 roles**

Recent publications using *ezh2*^{sa1199} arrived at opposite conclusions about the allele’s nature. Zhong and colleagues define and use this allele as a null to investigate hematopoiesis and clock gene expression (Zhong et al., 2018). In complete contrast, San et al. conclude the same allele is not a loss of function and further state this allele produces no phenotype (San et al., 2019). Zhong et al. assumed the *ezh2*^{sa1199} allele is a null based on immunoblots. However, their studies present phenotypes caused by an uncharacterized linked mutation in the Sanger Project line. San et al., like us, isolated *ezh2*^{sa199} away from the linked mutation (San et al., 2019). However, in contrast to their findings, we show *ezh2*^{sa1199}, while not a null, produces little Ezh2 protein or activity. Combined with a null allele, *ezh2*^{sa1199} reveals new Ezh2/PRC2-dependent phenotypes. Therefore, *ezh2*^{sa1199} is a severe and useful hypomorph.

ezh2^{sa1199} homozygous females are fertile, enabling easy studies of maternal Ezh2 during embryogenesis. When crossed to *ezh2*$^{+/-}$ males, offspring exhibit phenotypes similar to maternal-zygotic *ezh2* mutants described in previous work, albeit with a range of expressivity and surviving up to 6 dpf. Maternal *ezh2*$^{sa1199/sa1199}$ mutants enabled us to evaluate organ development at later time points than the complete maternal-zygotic *ezh2*-nulls generated by San et al (San et al., 2016). As described, we also found zygotic wildtype Ezh2 completely rescues maternal-zygotic mutant defects, suggesting PRC2 function is completely dispensable before maternal-to-zygotic transition. Consistently, ChIP-Seq studies find only low levels of H3K27me3 prior to zygotic genome activation (Lindeman et al., 2010; Murphy et al., 2018; Vastenhouw et al., 2010; Zhang et al., 2014).

***ezh2*^{sa1199} exemplifies how predicted null point mutations can instead produce hypomorphs through internal translation initiation**

Rigorous reverse genetics, including in zebrafish, requires characterizing mutations as null vs. partial loss-of-function alleles. Occasionally, sequence-predicted amorphs with early nonsense or frameshift mutations don't produce expected null phenotypic effects. These discrepancies can originate from misguided assumptions about gene function (for example, artifacts from uncontrolled morpholino studies (Lawson, 2016), compensatory mechanisms upregulating related genes (El-Brolosy et al., 2019; El-Brolosy & Stainier, 2017; Rossi et al., 2015; Williams et al., 2018), or from translation re-initiation or codon skipping). However, only a few examples have definitively shown such hypothesized mechanisms in action.

We explored if either our *ezh1* or *ezh2* alleles, both NMD-subject, could be compensated by transcriptional adaptation (El-Brolosy et al., 2019). Notably, Völkel et al. suggested upregulated *ezh2* compensates for *MZezh1* loss of function. However, embryonic *ezh2* transcript levels already are much higher than *ezh1* with largely overlapping, broad expression patterns. Regardless, our *ezh1*^{b1394} allele did not promote *ezh2* transcriptional adaptation in zygotic or maternal-zygotic *ezh1* mutants. Reciprocally, our *ezh2*^{b1392} allele, which produces undetectable amounts of Ezh2 protein and PRC2 activity and matches phenotypes of other reported *ezh2* presumptive null alleles, did not upregulate *ezh1*. Interestingly, zygotic *ezh1*$^{-/-}$ 6 dpf larvae had elevated Ezh2 protein. However, this is likely due to increased Ezh2 incorporation into stable PRC2 complexes in absence of competing Ezh1 (Montgomery et al., 2005; Pasini et al., 2004; X. Shen et al., 2008).

Unlike *ezh2*^{b1392} and other *ezh2* null alleles, *ezh2*^{sa1199} behaves as a hypomorph even though it has a nonsense mutation at codon 18. We show how *ezh2*^{sa1199} produces minimal but functional protein by weak translational initiation at methionine-24, which is upstream of Ezh2's essential WD40 binding domain and catalytic SET domain. The very small amount of truncated Ezh2 produced by *ezh2*^{sa1199} is sufficient to fulfill much of Ezh2/PRC2's embryonic roles. Therefore, *ezh2*^{sa1199} allele exemplifies how translational machinery can bypass early termination signals to convert expected null alleles into hypomorphs without severe phenotypes and that do not generate compensation given insufficient protein loss-of-function feedback. Relatedly, the allele provides a design framework to intentionally produce valuable hypomorphs. As a Sanger project allele that was mistakenly associated with a phenotype from a linked mutation (Zhong et al., 2018), *ezh2*^{sa1199} also highlights the need to thoroughly validate mutants from non-specific mutagenesis resources.

PRC2 has conserved roles in craniofacial bone formation and skeletal patterning

Mouse conditional knockout models disrupting PRC2 show analogous craniofacial defects to those we describe here. Schwarz and colleagues showed conditional ablation of *Ezh2* in cranial neural crest cells using *Wnt1:Cre* causes severe craniofacial defects, including lack of calcification, a poorly formed styloid process, and missing hyoid bone (Schwarz et al., 2014). Both are BA2/PA2 derived bones like BSRs and OPs of fish. In addition, Ferguson et al. found decreased bony matrix of calvarial bones using *Pdgfra:CreER* to delete *Ezh2* in cranial mesenchymal stem cells (Ferguson et al., 2018). Similar to our findings, they noted fewer sp7/OSX^{+} cells. However, instead of a smaller osteoblast pool due to decreased proliferation as in our studies, they find that osteoblast progenitors are formed but fail to fully differentiate. Nevertheless, these studies and ours suggest cranial neural crest cell derived osteoblasts are sensitive to Ezh2 loss.

The PcG famously represses *Hox* genes to maintain Hox codes corresponding to body segment identities. Many PRC1 but few PRC2 mutants have been characterized with axial skeleton homeotic transformations. This discrepancy may reflect lethality before skeletal patterning upon complete loss of any of the three core subunits of PRC2 (Eed, Suz12, Ezh2). Only an *Eed* hypomorph has been reported *a priori* to cause posterior transformations of the axial skeleton (Shumacher et al., 1996). Our ability to produce viable but near null *ezh2* transheterozygote zebrafish enables investigating how Ezh2 contributes to axial skeletal and appendage development in another vertebrate. Similar to the murine *Eed* hypomorph, our zebrafish *ezh2* hypomorphs have posterior vertebrae transformations with the posterior pre-caudal vertebrae assuming a caudal identity characterized by rib loss. Correspondingly, mutations in *Jmjd3/KDM6A,* an H3K27me3 demethylase, cause anterior homeotic transformations and gain a rib (Naruse et al., 2017). We also see changes in appendage morphology and in some cases, entirely missing pelvic fins. Numerous links of *Hox* genes to appendage patterning (Jain et al., 2018; Minguillon et al., 2012; Nakamura et al., 2016) suggest misexpression of *hox* genes could account for these phenotypes as well.

Early Developmental Roles of PRC2

San et al. showed *MZezh2*-null embryos form a regular body plan and many organs retain early specification markers (San et al., 2016). Our genetic studies combining *ezh1* and *ezh2* loss confirm the *MZezh2*-null phenotype represents the total loss of PRC2 from oocyte through embryonic lethality at 2 dpf. This genetic approach neatly complements a recent multi-omics study showing near loss of H3K27me3 in absence of maternal and zygotic Ezh2 but retained Ezh1(Rougeot et al., 2019). The surprisingly normal body plan of *MZezh2*$^{hu5670/hu5670}$ embryos underscores that PRC2 does not play central, instructive roles in earliest steps of embryogenesis including initial cell lineage specification or gastrulation. These PRC2's key functions seem concentrated during a narrow window of development succeeding zygotic genome activation. Either maternal or zygotic Ezh2 can support these PRC2 functions, underscored by the wildtype phenotype of *M*^{sa1199}*Zezh2*$^{+/sa1199}$ larvae compared to severe defects of *M*^{sa1199}*Zezh2*$^{sa1199/-}$ clutchmates.

ezh1$^{-/-}$*; ezh2*$^{-/-}$ double zygotic mutants develop remarkably well for lacking nearly all H3K27me3 by 6 dpf and are grossly identical to *ezh2*$^{-/-}$ larvae. We do observe slightly smaller BSR3s in *ezh1*$^{-/-}$*; ezh2*$^{-/-}$ larvae compared to loss of *ezh2* alone, supporting partial Ezh1/Ezh2 redundancy in promoting bone development. Nevertheless, Ezh1 is unable to rescue *ezh2* mutants. This inability may stem from a capacity of Ezh1/PRC2 to maintain but not initiate H3K27me3 marks. In support, we show Ezh1 can partially replace Ezh2/PRC2-deposited bulk H3K27me3 marks in zygotic but not maternal/zygotic *ezh2* mutants. Therefore, Ezh1/PRC2 is only capable of maintaining H3K27me3 marks already established by Ezh2/PRC2.

We show Ezh1 is the majorly expressed post-embryonic PRC2 H3K27me3 methyltransferase, corresponding to previous observation of relatively elevated Ezh1 in mature cells (Raphael Margueron et al., 2008). However, as in mice, *ezh1* loss does not overtly disrupt development or even fertility (Ezhkova et al., 2011). We also note *ezh2*$^{sa1199/-}$ zebrafish can develop to adulthood with almost complete loss of zygotic Ezh2/PRC2 activity. Together, we conclude once past a critical early embryonic window, core vertebrate PRC2's transcriptional maintenance roles are surprisingly superfluous, at least in a laboratory setting.

Zebrafish provide an attractive context to define PRC2's many conserved organogenesis roles. Potential studies include exploring if PRC2 has locus-specific vs. generalized activities and if common themes for its roles exist across organs. As mentioned, PRC2/H3K27me3 apparently is not required for most initial cell lineage specification, contrasting expectations from mouse knockout and ES cell studies. However, PRC2 may enable diversification of related cell types sharing a common lineage. For instance, craniofacial osteoblasts and chondrocytes originate from cranial neural crest cells and express Runx2 but are distinct cell types. Chondrocytes develop first, suggesting they represent a default state for osteochondroprogenitor cells with later instructions specifying osteoblast identity. In addition, fused cartilaginous elements in zebrafish *ezh2* mutants could result from inability to specify joint forming cells, another closely related cell type sharing a common progenitor (Nichols, Pan, Moens, & Kimmel, 2013). As such, PRC2 may canalize related cell types with few but influential differences in gene expression programs.

We describe how PRC2 is required for expansion of dermal bone pre-osteoblast populations and their migration. Further, we saw enhanced osteoblast maturation upon Ezh2 inhibition. Together, we conclude Ezh2/PRC2 maintains osteoblast progenitor characteristics, consistent with extensive links of PRC2 with progenitor state maintenance (Laugesen & Helin, 2014). In contrast, other studies more strongly link PRC2 to cell differentiation (Chamberlain et al., 2008; Ferrari et al., 2014; Lavarone et al., 2019; Pasini et al., 2007). We propose the varied in vivo PRC2 roles represent a generalized PRC2 function maintaining cell states – progenitor vs. differentiated – as well as cell identities. PRC2/H3K27me3 marks therefore establish cell state/fate transition barriers by repressing leaky transcription to maintain rather than instruct cell states and identities. PRC2 loss then manifests in differential phenotypes reflecting the particular gene regulatory networks most subject to transcriptional noise in a given context.

MATERIALS AND METHODS

Zebrafish

The University of Oregon Institutional Animal Care and Use Committee (IACUC) approved and monitored all zebrafish procedures following the guidelines and recommendations outlined by the Guide for the Care and Use of Laboratory Animals (National Academic Press). The following established lines were used in this study: *Tg(sp7:EGFP)b1212* (DeLaurier et al., 2010), *Tg(runx2b:GAL4)* (gift from Chuck Kimmel), *Tg(uas:E2CRIMSON)b1229* (Nichols et al., 2013), *Tg(fli1a:EGFP)y1* (Lawson & Weinstein, 2002), *ezh2*^{sa1199} (Kettleborough et al., 2013), *ezh2*^{b1392} (this study), and *ezh1*^{b1394} (this study).

CRISPR-Cas9 generation of mutant alleles

Generated CRISPR-Cas9 meditated mutations using methods previously described (Akerberg et al., 2017). Targeted sequences for guide RNAs were 5'- AATGGACTGGATCCGGAGCT -3' for *ezh1* and 5'- GTTCCACGCAAGGAGCTCAC -3' for *ezh2*.

Genotyping mutant alleles

Fish were genotyped by PCR using primers flanking the mutated region followed by restriction digest. CRISPR/Cas9 generated indels disrupted BspEI and SacI restriction sites in *ezh1* and *ezh2* mutant alleles, respectively. CRISPR mutant genotyping primers: *ezh1* 5'- GGCTGAATGTTTGTGGCTTTTTCACC -3', 5'- GGAAATGGCGAGGCAAAGCTGAC -3', *ezh2* 5'- GTAATCCATGGGCTAGTACAGC -3', 5'- CCCTTTCACTTTTAACACTGTGC -3'.

Primers used to genotype *ezh2*^{sa1199} introduced (base in bold and underlined of reverse primer) a BstUI restriction site in amplicons of the wildtype allele. Primers: *ezh2*^{sa1199} 5'- CATGGACATCTTTGGGTCCT -3', 5'- AGCCGCATGTACTCAGACTTCAC**G**C -3'

Skeletal staining

Alcian Blue and Alizarin Red staining of zebrafish larvae was performed as described (Walker & Kimmel, 2007) with subsequent imaging using a Leica DM4000B upright microscope (flat mount).

For live Alizarin Red staining, 6 dpf fish were placed in EM containing 0.005% Alizarin Red and 0.1x HEPES for 1 hour in the dark. Fish were rinsed for 15 min in EM and then anesthetized with tricaine and mounted in 1% low melt agarose containing tricaine and imaged using a Leica SD6000 spinning disk confocal microscope with a 20x objective.

Juvenile and Adult fish 3 weeks to 7 months old were euthanized with tricaine until opercle movement ceased for at least 10 min and then fixed in 2% PFA/PBS for 4 hours to overnight at room temperature. Fish were washed for 1 hour with 100 mM tris pH 7.5/ 25 mM $MgCl_2$ and then incubated overnight in 0.02% Alcian Blue/ 80% ethanol/ 100 mM tris pH 7.5, 25 mM $MgCl_2$. Samples were then washed with 80% ethanol/ 100 mM tris pH 7.5/ 25 mM $MgCl_2$ for one hour, 50% ethanol/ 100 mM tris pH 7.5 for one hour, 25% ethanol/ 100 mM tris pH 7.5 for one hour. 0.5% potassium hydroxide was used to bleach samples until eyes were light brown. Samples were washed with 35% saturated borate for one hour, and then cleared with 1% trypsin/ 35% sodium borate. Cleared samples were washed for one hour with 10% glycerol/ 0.5% KOH and stained with 0.02% Alizarin Red/ 10% glycerol/ 0.5% KOH overnight. The next day samples were washed with 50% glycerol/ 0.5% KOH for one hour. Samples were then washed overnight with fresh 50% glycerol/ 0.5% KOH . Fish were imaged with a Leica M165 FC stereomicroscope.

Immunoblot

Three dpf and 6 dpf larvae were bisected using the vent as a landmark. Anterior portions were stored in 15 µL RIPA buffer at -80^{o}C. Posterior ends were placed in 30 µl

50 mM NaOH and boiled at 95^{o}C for 20 minutes for genomic DNA. Genomic preps were neutralized with 7.5 μl 1 M Tris pH 7.5 and then used for genotyping. Samples stored in RIPA were pooled according to genotype and lysed using a Bioruptor on high for 5-10 minutes with 30 sec ON/OFF cycles. Individual fin regenerate samples were collected at 72 hours post amputation and placed in 40 μl RIPA buffer and dissociated by pipette. Once fin tissue was fairly disrupted, samples were placed in Bioruptor for 5 minutes on high for 5 minutes with 30 sec ON/OFF cycles for further dissociation. Samples were centrifuged at 14,000 RPM for 5 minutes. Supernatant was placed into a fresh tube and an aliquot was used to quantify by Bradford assay.

Samples were boiled for 10 min at 95^{o}C with 3 μL of 6x loading buffer (300mM Tris pH 6.8, 60% glycerol, 12% SDS, 0.6M DTT, 0.025% Bromophenol blue), iced for 5 min, and loaded on either a 10% or 15% Tris/Glycine gel and ran in running buffer (25 mM Tris, 144 mM Glycine, 0.1% SDS). Protein was transferred to PVDF membrane in transfer buffer (25 mM Tris, 192 mM Glycine, 20% Methanol) for 2-3 hours. Membrane was rinsed in Tris Buffered Saline containing 0.1% tween-20 (TBST) and blocked in either 5% Bovine Serum Albumin (BSA), or 10 % dry milk in TBST for at least one hour. Blocked membranes were incubated with primary antibodies diluted in blocking solution, Rabbit anti- Ezh2 1:1000 (Cell Signaling Technologies), Rabbit anti-H3K27me3 1:2000 (Millipore), Rabbit anti- histone H3 1:10,000 (Abcam), overnight at 4^{o}C in anaerobic conditions. The next day membranes were rinsed three times with TBST followed by four washes for 10 minutes, and then incubated with HRP- conjugated secondary antibodies for two hours at room temperature. Wash steps were repeated. Immunoblots were developed with ECL (GE) and imaged using Li-COR Odyssey.

Time-lapse imaging

Offspring from an *ezh2*$^{+/-}$; *Tg(sp7:eGFP)* x *ezh2*$^{+/-}$ cross were anesthetized with 80 mg/l clove oil in embryo medium and then mounted in 0.5% low melt agarose dissolved in embryo medium containing clove oil in a glass bottom chamber. Mounted fish were then covered with EM containing clove oil. Fish were imaged every 20 min from 52 hpf to 3 dpf on a Leica SD6000 spinning disk confocal microscope outfitted with a heated stage set to 30^{o}C.

Quantitative reverse transcription polymerase chain reaction (qRT-PCR)

cDNA was synthesized using Maxima H Minus Reverse Transcriptase (Thermo Fisher) with Trizol-isolated RNA from pooled samples of three genotyped 48 hpf embryos, 6 dpf larvae, or individual 72 hpa fin regenerates. qRT-PCR was performed using KAPA SYBR FAST qPCR master mix reagents (Kapa Biosystems). Relative mRNA expression was normalized using *rpl8* to calculate ΔCTs (threshold cycles). Transcript levels were compared using a ΔΔCT approach. qPCR primer sequences: *rpl8* 5’- CCGAGACCAAGAAATCCAGA -3’, 5’- GAGGCCAGCAGTTTCTCTTG-3’, e*zh2* 5’- CTTGCGTGGAACCAGAGAG -3’, 5’- GCATTCACCAACTCCACAAA -3’, *ezh1* 5’- GAGCTGCTGAATGAAGAATGGTCC -3’, 5’- CCTCCACCATGAAGTTCTGCTG - 3’.

5-ethynl-2-deoxyuridine labeling

Fish were incubated with 0.1 mg/ml of 5-ethynl-2-deoxyuridine (EdU) (Thermo Fisher) in embryo media for 2 hours prior to harvest at 98 hpf. Harvested embryos were fixed with 4% PFA in PBS overnight at 4°C, then washed 3 x 10 min in PBS. Embryos were then dehydrated through a methanol series and stored at -20°C for at least 24 hours in 100% methanol.

Embryos were rehydrated into PBS containing 0.1% Tween-20 prior to performing EdU Click-It reactions (Thermo Fisher) as described by the manufacturer. Immunostaining was carried out after completing the Click-It reaction.

Whole mount immunofluorescence and imaging

Embryos and Larvae were euthanized with tricaine and placed on ice for 10 minutes at desired timepoint, fixed overnight at 4°C with 4%PFA in PBS containing 0.1% Tween-20 (PBST), then washed 3 times for 10 minutes. Samples were dehydrated into 100% methanol through a methanol series and stored at -20°C for at least 24 hrs.

Samples were rehydrated into PBST and then treated with 10 ug/ml proteinase K diluted in PBST for 30 minutes at room temperature. Samples were then fixed for 20 minutes at room temperature with 4% in PBST, washed 4 times for 10 minutes with PBST and then blocked for two hours in 10% normal goat serum/ 1% bovine serum albumin/ 1% DMSO/ 1X PBS/ 0.5% Triton X-100. Samples were incubated with chicken anti-GFP 1:1000 (Aves) and rabbit anti-DsRed 1:500 (Clontech/Takara) antibodies diluted in blocking solution overnight at $4^{o}C$. After incubation with primary antibodies, samples were washed four times for 15 minutes in PBS containing 0.5% Triton X-100. Alexa-conjugated secondary antibodies were diluted in blocking solution 1:1000 and incubated with samples for two hours at room temperature. Samples were washed two times for 15 minutes with PBSTx, then incubated with TO-PRO-3 (Thermo Fisher) diluted 1:2000 in PBS for 30 minutes. After three 10 minutes washes in PBS, samples were mounted in 1% low-melt agarose and imaged using a Leica SD6000 spinning disk confocal microscope.

Sectional Analysis

Larvae and embryos were collected and euthanized at desired timepoints and fixed with 4%PFA in PBST for either 3 hrs at room temperature or overnight at $4^{o}C$. Samples were washed 3 times for 10 minutes with PBST then dehydrated into 100% ethanol. Samples were stored in 100% ethanol overnight, washed twice in xylenes for 10 minutes and then embedded in paraffin. Samples were sectioned at 7 µm thickness.

Staining with hematoxylin and eosin (H+E) was performed using standard procedures (Ricca Chemical Company). Images were taken using a Leica DM4000B upright microscope.

For immunofluorescent staining, sections were de-paraffinized by washing in xylenes 2 times for 10 minutes. Sections were then rehydrated into milliQ water and washed with PBST for 5 minutes. Antigen retrieval was performed using 1 mM EDTA and 0.1% Tween-20 and pressure-cooked for 5 minutes. Samples were then rinsed three times with PBST and blocked with 10% non-fat dry milk in PBST for one hour at room temperature. Samples were incubated with primary antibodies diluted in blocking solution overnight at 4ºC. Primary antibodies were used at the following concentrations: H3K27me3 (Cell Signaling Technologies, clone C36B11) 1:1000; MF20, myosin heavy chain (Developmental Studies Hybridoma Bank) 1:250; Pan-Cadherin (Novus) 1:250. Slides were then rinsed 2 times followed by three 5 minutes washes in PBST. Sections were incubated in 0.5 M NaCl in PBST for 30 minutes and then rinsed two times with PBST. Samples then were incubated with Alexa-conjugated secondary antibodies (Invitrogen) diluted 1:1000 in block solution for one hour at room temperature. Slides were then rinsed twice and washed three times for 5 minutes with PBST, then incubated with Hoechst (Invitrogen) diluted 1:4000 in PBS, followed by two more 5-minute washes in PBS. Slides were mounted using SlowFade® Diamond (Thermo Fisher) and imaged using a Zeiss LSM 880 laser scanning confocal microscope.

Cell counting and morphometrics

Osteoblasts and cranial neural crest cells of immunostained samples were counted using Fiji (National Institute of Health). GFP-positive and DsRed-positive cells were located and counted through image stacks. BSR3 lengths were measured on alizarin red and alcian blue stained flat mounts or alizarin red stained *Tg(sp7:eGFP)* larvae using the measurement tool in Fiji.

Whole mount in situ hybridization

Digoxigenin-11-dUTP (Roche) labeled riboprobes were synthesized from PCR products amplified from larval cDNA. Reverse primers were fused with T7 transcription promotor sequence. *hoxa9b* primers are adapted from a previous study (van der Velden et al., 2012). Probes against *ezh1* and *ezh2* target 3' UTRs to prevent cross detection by paralog probes. Primers for riboprobe templates: *hoxa9b* 5'- CCCGTGGTCCAGCAGCAGTC -3', 5'- TAATACGACTCACTATAGTGCACTCACCACTCCCAACC -3', *ezh1* 5'- ACGACCCACAATACTTTGCACTTC -3', 5'- TAATACGACTCACTATAGGGTACATGTGACAGTATAACCTGAACC -3', *ezh2* 5'- CCATCTACCTCTCTGAACAAATGCCT -3', 5'- TAATACGACTCACTATAGGGCACCTTGTATTTGGAGGCAACAAC -3'. DNase treated probes were precipitated with LiCl and reconstituted in RNase free water. Whole-mount in situ hybridization was performed as previously described (Akerberg et al., 2017).

in vitro alkaline phosphatase assay

AB.9 cells (ATCC® CRL-2298™) (Paw & Zon, 1999) were seeded in six-well plates and cultured in Dulbecco's Modified Eagle's medium (DMEM) supplemented with fetal bovine serum (10%), 1X penicillin-streptomycin (Gibco) and either DMSO (0.1%) or 5 μM EPZ-6438 (Medchem express) diluted in DMSO. After two days, cells were rinsed twice with PBS and switched to incomplete differentiation medium (Minimum Essential Medium alpha, 0.1% Fatty acid free bovine serum albumin, 5 mM β-glycerophosphate, 50 μg/ml ascorbic acid, 100 nM dexamethasone) or complete differentiation medium (Incomplete differentiation medium + 100 ng/ml Insulin-like Growth Factor). DMSO or

EPZ-6438 was added when media was changed and once more 48 hours after media change. On day 6, media was aspirated, cells were washed once with PBS, and then fixed with 4% formaldehyde in PBS for 1 minute. Wash once with PBS and once more with PBS containing 0.1% Tween-20. Cells were washed once for 5 minutes in developing buffer (100 mM Tris pH 9.5, 100 mM NaCl, 10 mM $MgCl_2$) and then developed with fresh developing buffer supplemented with 225 ug/ml nitro blue tetrazolium (NBT) (Promega) and 175 ug/ml 5-bromo-4-chloro-3-indolyl-phosphate (BCIP) (Promega) in the dark. Reaction was stopped with three PBS rinses Cells were fixed with 4% PFA in PBS for 5 minutes at room temperature, then wash three times for 5 minutes. Samples were imaged using a Leica M165 FC stereomicroscope.

BRIDGE TO CHAPTER IV

Chapter III focused on developmental roles of Ezh1 and Ezh2. We found that Ezh2-containing PRC2 promotes osteoblast progenitor characteristics allowing for appropriate bone shape and size during development. Ezh1 has minimal roles during development but is partially redundant during bone growth. I identified an *ezh2* hypomorph allele we used to investigate roles of maternal Ezh2 during development. We corroborated findings that Ezh2 is expendable for initiation of the zebrafish body plan. Maternal or zygotic Ezh2 can fulfill developmental roles after zygotic genome activation. Ezh2 appears to support later developmental cell choices, such as distinguishing between closely related cells such as chondrocytes and osteoblasts. The hypomorph allele also enabled us to observe consequences in axial skeleton due to Hox gene misexpression. Chapter IV presents our investigation if PRC2 plays similar roles in progenitor maintenance and lineage specification during fin regeneration.

CHAPTER IV

INVESTIGATING POLYCOMB REPRESSIVE COMPLEX 2 DURING REGENERATION

AUTHOR CONTRIBUTIONS

Gabriel A. Yette, Astra L. Henner, Scott Stewart and Kryn Stankunas designed experiments. Gabriel A. Yette performed most experiments and prepared text and figures. Astra L. Henner performed *ezh1* RNAscope experiment.

INTRODUCTION

Unlike mammals, adult zebrafish flawlessly regenerate many tissues and organs including their bony fin appendages. The caudal fin contains 18 bony rays that upon amputation, robustly regenerate to the same length as their pre-damaged state. The source of restored tissue is the mature cells that remain after injury (Knopf et al., 2011; Sousa et al., 2011; Stewart & Stankunas, 2012; Tu & Johnson, 2011). Upon amputation, cells near the site of damage undergo limited de-differentiation and stay fate determined. Fully differentiated bone-producing osteoblasts downregulate mature genes, such as *sp7/osx*, and become more progenitor-like by re-activating osteoblast developmental genes, like *runx2a/b*. Wnt ligands, produced by distal-residing, de-differentiated intra-ray mesenchymal cells, maintain this proliferative progenitor state (Stewart et al., 2014; Wehner et al., 2014). The source of Wnt remains distal as the fin continues to grow outward. Proximal progenitor osteoblasts (pObs) become distanced from Wnt, upregulate maturation genes *bmp2b* and *sp7*, produce DKK1 to antagonize Wnt response, and transition to a differentiated state capable of bone production (Stewart et al., 2014). While

Wnt drives progenitor perdurance, how cells reprogram their gene expression profiles to transition between mature and de-differentiated states is less understood.

Histone modifications and chromatin structure influence gene expression during development and tissue homeostasis. Directed activity of histone and chromatin modifiers could be the key to osteoblast state changes. One modification with growing evidence as playing a role in regeneration is tri-methylation of lysine 27 of histone H3 (H3K27me3) (Ai et al., 2017; Ben-Yair et al., 2019; Dupret et al., 2017; Hamada et al., 2015; Stewart et al., 2009). H3K27me3 is associated with stably transcriptionally repressed regions of the genome and is variably deposited depending on cell type and state. The Ezh2 or Ezh1 histone methyltransferase component of Polycomb Repressive Complex 2 (PRC2) deposits H3K27me3 (Gökbuget & Blelloch, 2019; Scelfo et al., 2015; Yu et al., 2019). Ezh2 tends to be highly expressed in progenitor-like cells whereas Ezh1 appears to be the predominant methyltransferase in mature cells (Raphael Margueron et al., 2008). *Ezh2*-null mice die around gastrulation (O'Carroll et al., 2001) while *Ezh1* mutants are completely viable (Ezhkova et al., 2011). Similar deleterious effects are seen in Ezh2-deficient mouse ES cells that fail to form embryoid bodies, whereas Ezh1-nulls are still able to form embryoid bodies (Chamberlain et al., 2008; Ferrari et al., 2014; Lavarone et al., 2019). Taken together, Ezh2 is able to completely fulfill developmental and later roles of Ezh1. Conversely, Ezh1 cannot satisfy developmental needs in the absence of Ezh2. However, in mouse hair follicles and intestinal crypt cells Ezh2 and Ezh1 are completely redundant (Ezhkova et al., 2011; Koppens et al., 2016).

H3K27me3 was first implicated in regeneration with the identification of its demethylase, *kdm6bb/Jmjd3*, as highly upregulated during zebrafish caudal fin regeneration (Stewart et al., 2009). In contrast to Ezh2, Kdm6b/Jmjd3 removes H3K27me3 and is associated with gene activation (Cloos et al., 2008). Morpholino knockdown of *kdm6bb* resulted in decreased regeneration of larval zebrafish fin fold (Stewart et al., 2009). This same study found increased expression of *ezh2* and not *ezh1* during adult caudal fin regeneration. Treatment with the S-adenosyl methionine homocysteine hydrolase inhibitor, DZNEP, disrupts many methyltransferases, including Ezh2, and caused severely stunted fin regeneration (Stewart et al., 2009). A later study found impaired larval fin fold regeneration in *ezh2* mutants or the presence of an Ezh2-specific inhibitor, GSK126 (Dupret et al., 2017). Taken together, these studies point to a key role for H3K27me3 and its regulation during adult fin regeneration.

In contrast to mouse heart development, Ezh2 is expendable and Ezh1 is required for neonatal heart regeneration (Ahmed, Wang, & Delgado-Olguin, 2018; Ai et al., 2017). Induced expression of the dominant-negative oncohistone, H3.3K27M reduced PRC2 function and impaired zebrafish heart regeneration (Ben-Yair et al., 2019). Yet, a thorough investigation of overlapping and divergent roles of Ezh2 and Ezh1 during zebrafish bone regeneration has yet to be conducted.

Here, I use a combination of *ezh2* and *ezh1* loss-of-function alleles to assess requirement of PRC2 activity during zebrafish caudal fin regeneration. I describe Ezh2 expression during de-differentiation and re-differentiation stages of regeneration. Further, I assess osteoblast cell state specific H3K27me3 levels. Lastly, I show Ezh2/PRC2 activity has limited effects on caudal fin regeneration whereas predominantly Ezh1/PRC2, promotes robust fin skeletal regeneration .

RESULTS

Ezh2 is upregulated in de-differentiated populations during regeneration

Many cell types make up the regenerating fin (Tu & Johnson, 2011). While *ezh2* expression has previously been assayed during adult caudal fin and larval fin fold regeneration by RT-qPCR and RNA in situ hybridization, these studies lacked temporal and cellular resolution (Dupret et al., 2017; Stewart et al., 2009). To determine if increased Ezh2 expression is restricted by space and time, we immunostained regenerating fins from *Tg(sp7:eGFP)* fish (DeLaurier et al., 2010) at 24 hours post amputation (hpa) (Fig. 4.1) and 72 hpa (Fig. 4.2) with antibodies against Ezh2, Runx2 (pre-osteoblast marker), and sp7:eGFP (mature osteoblast marker). At 24 hpa (Fig 4.1), we observed three expression patterns defining sub-types or states of osteoblasts: Runx2^{+}/sp7^{+}/Ezh2^{+} cells, Runx2^{+}/sp7^{low}/Ezh2^{+} cells and Runx2^{low}/sp7^{+}/Ezh2^{low} cells. Consistent with previous reports, some Runx2^{+} cells were below the amputation plane and were still lining the bone, presumably prior to losing epithelial junctions and becoming mesenchymal (Stewart et al., 2014). Notably, these cells also expressed Ezh2, suggesting that osteoblasts must acquire Ezh2 and Runx2 before becoming fully mesenchymal. sp7:eGFP positive cells distal of the amputation plane are likely due to GFP perdurance long after the cells downregulated endogenous *sp7*. At 72 hpa (Fig 4.2), Ezh2 was most highly expressed in the distal Runx2^{+} osteoblasts and intra-ray mesenchymal cells. As osteoblasts acquired sp7 expression, there was a concurrent decrease in Ezh2. We observed lowest Ezh2 levels in proximal Runx2^{low}/sp7^{+} osteoblasts. These data suggest Ezh2 regulates gene expression in progenitor cells during regeneration.

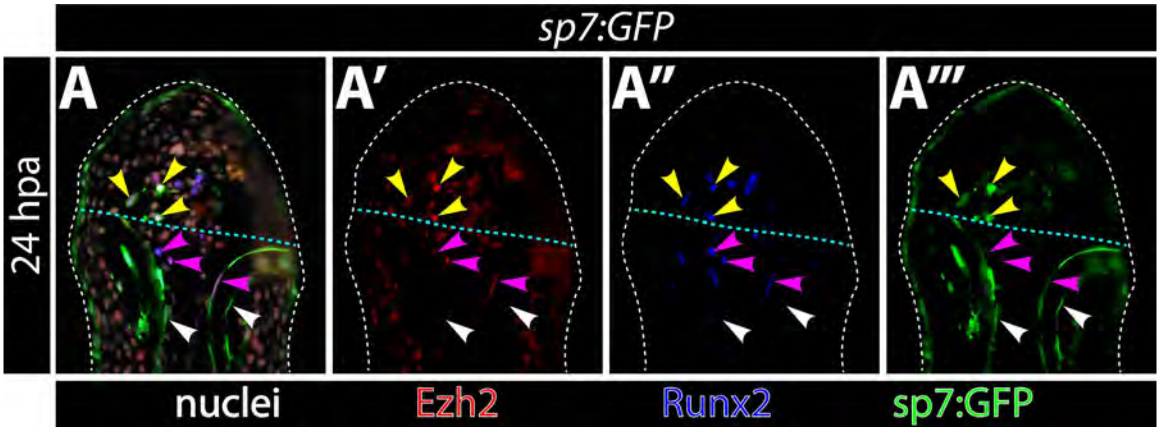

Figure 4.1. Ezh2 is upregulated in de-differentiating osteoblasts. Images of a sectioned *Tg(sp7:eGFP)* fin immunostained with antibodies to detect Ezh2 (red), Runx2 (blue), and GFP (green). Nuclei are in grey in the overlay (A). Tissue is outlined with white dashed line. White arrowheads point to Runx2^{low}/sp7:eGFP^{+}/Ezh2^{low} osteoblasts still lining the bone. Magenta arrowheads point to osteoblasts below the amputation plane (cyan dashed line) that have low sp7 expression, and high Ezh2 and Runx2 expression. One cell in this category is yet to become mesenchymal. Fully mesenchymal osteoblasts distal to the amputation site are Runx2^{+}/sp7:eGFP^{+}/Ezh2^{+} are identified with yellow arrowheads. GFP expression is likely due to protein perdurance and not current activity of the *sp7* promoter.

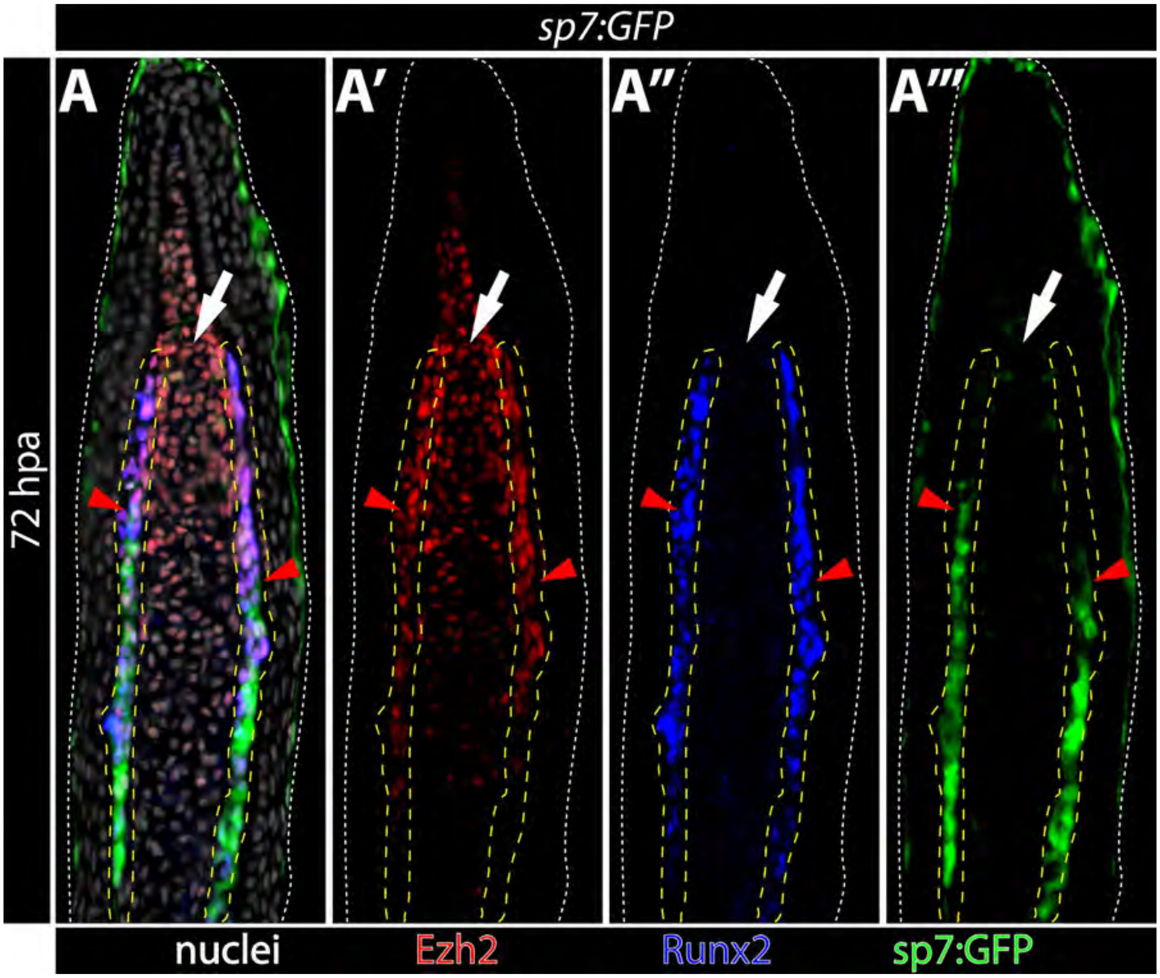

Figure 4.2. Ezh2 remains high in progenitor cells and is diminished in maturing populations. Sectioned bony fin ray from a *Tg(sp7:eGFP)* fish at 72 hpa immunostained for Ezh2 (red), Runx2 (blue), and GFP (green). Nuclei are in grey. Dashed white line outlines fin tissue. Yellow dashed lines outline osteoblast lineage. White arrow points to region of high Ezh2 expression in distal niche cells that are the same lineage as the intra-ray mesenchyme. Red arrowheads indicate differentiating osteoblasts that re-acquire sp7 expression and start to downregulate Ezh2.

H3K27me3 is lowest in transitional cells

H3K27me3 demethylases are also expressed distally during fin regeneration (Stewart et al., 2009). To assess if H3K27me3 levels reflected upregulated Ezh2 expression and ascertain if Kdm6 proteins actively opposed Ezh2 activity, we stained regenerating fins of *Tg(sp7:eGFP)* fish for H3K27me3, Runx2 and GFP at 72 hpa. Similar to Ezh2 expression, H3K27me3 was abundant in distal intra-ray mesenchymal cells and distal Runx2$^+$ osteoblasts (Fig. 4.3). Joint cells adjacent to distal pObs that express high levels of Runx2 and never acquire sp7 expression (Ando, Shibata, Hans, Brand, & Kawakami, 2017) also showed elevated H3K27me3. Joint cell-proximal differentiating osteoblasts that re-acquired sp7 expression showed lower levels of H3K27me3, mimicking their reduced Ezh2 expression. More proximal still, are sp7$^+$ Obs that, based on Ezh2 expression, we predicted to have low H3K27me3. Surprisingly, these cells had more H3K27me3 than further distal osteoblasts. Also inconsistent with Ezh2 expression, we observed the highest H3K27me3 abundance in the most distal epidermis and basal epidermis. H3K27me3 likely is further modulated in a loci-dependent manner by demethylases to produce the observed H3K27me3 patterns. Nevertheless, it is apparent that while bulk H3K27me3 levels do not completely mirror Ezh2 expression, they dynamically vary between osteoblast subtypes during regeneration.

Figure 4.3 (next page). Decreased H3K27me3 in transitioning cells could facilitate re-differentiation. Confocal images of a 72 hpa fin from a *Tg(sp7:eGFP)* fish stained for Runx2 (blue), GFP (green), H3K27me3 (red) and nuclei (grey). Tissue is outlined in orange dashed line. Yellow dashed line outlines some osteoblasts. White arrow points to distal niche cells with slightly elevated H3K27me3. Yellow arrow points to basal epidermal cells with very abundant H3K27me3. Runx2$^+$/sp7$^-$ osteoblasts have elevated H3K27me3 (white arrowheads) and some mature sp7$^+$ cells also have increased H3K27me3 (magenta arrowheads). Dashed boxes provide magnifications of osteoblasts in different cell states. White dashed box outlines Runx2$^+$/sp7$^-$ osteoblasts. Green dashed line boxes transitioning cells that have lower H3K27me3. Notably, there are osteoblasts at both ends of the green dashed box that have increased H3K27me3.

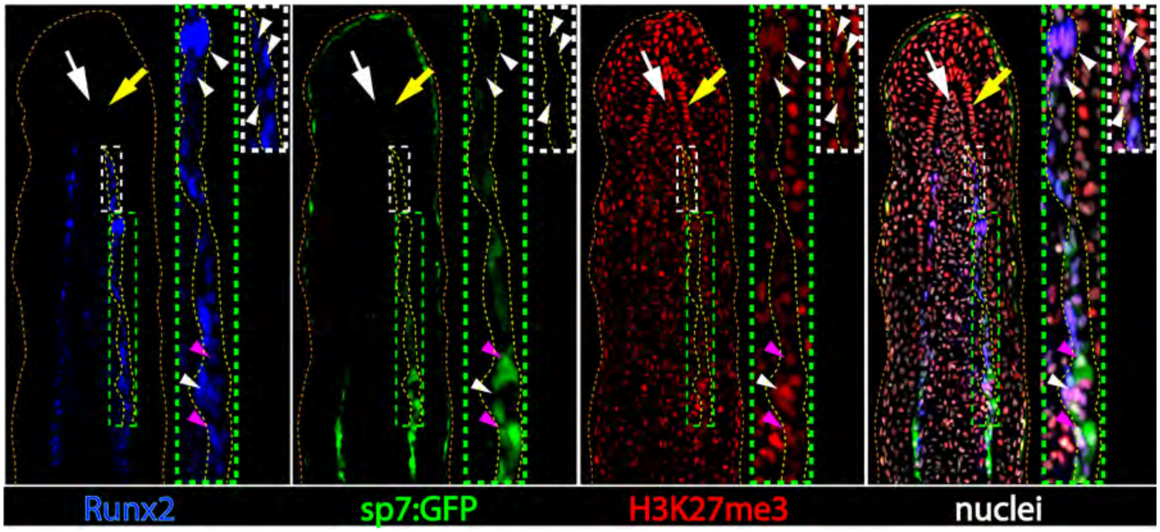

Ezh2 is not required for caudal fin bone regeneration.

We and others previously found that *ezh2*-null zebrafish die around 2 weeks post fertilization (Dupret et al., 2017; San et al., 2018), precluding adult regeneration experiments. Dupret and colleagues did see regeneration defects in larval *ezh2* mutant fish (Dupret et al., 2017). While larval regeneration appears to have similar mechanisms as adult caudal fin regeneration (Kawakami, Fukazawa, & Takeda, 2004), conclusions are limited since developmental cells tend to be more plastic and it is difficult to parse out what is a developmental defect versus a regeneration defect. In addition, the larval fin fold lacks the architecture of the adult fin.

We isolated a severe hypomorph *ezh2* allele, *ezh2*^{sa1199}, that bypasses early lethal phenotypes. We crossed heterozygous animals to *ezh2*$^{+/b1392}$ to generate transheterozygotes. Based on phenotypic analysis, *ezh2*$^{sa1199/b1392}$ animals had less PRC2 activity than *ezh2*$^{sa1199/sa1199}$ animals and still survived to adulthood (Fig. 3.5, Fig S3.5). We amputated caudal fins of transheterozygous fish to assess if regeneration can persist with greatly impaired Ezh2 function. Surprisingly, regeneration was seemingly unaffected by near complete loss of Ezh2 for 11 days (Fig. 4.4). There were no apparent defects in pOb generation as evident by regeneration occurring, or in Ob maturation as demonstrated by retained sp7:eGFP expression.

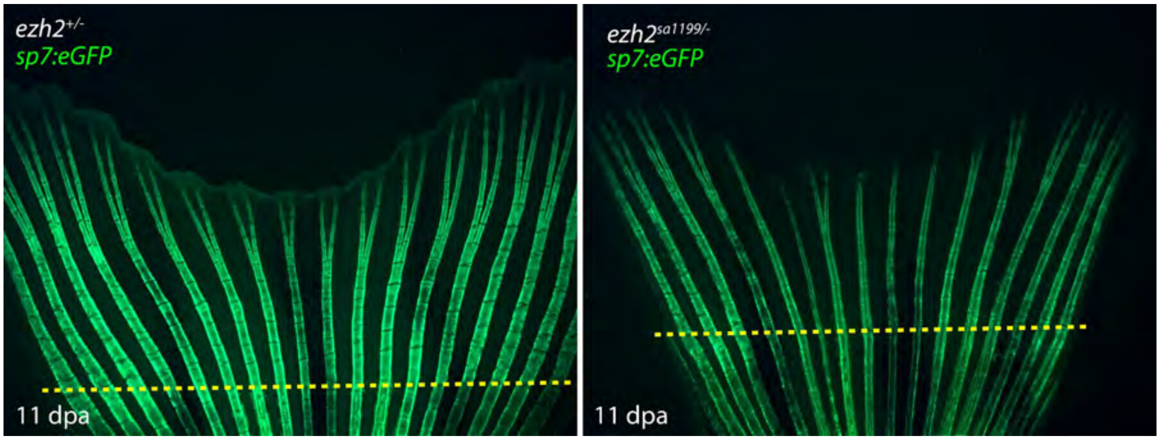

Figure 4.4. Ezh2 is dispensable for caudal fin regeneration. Live epifluorescent images of wildtype (left panel) and *ezh2*$^{sa1199/-}$ (right panel) clutchmate fins at 11 days post amputation. Yellow dashed line indicates amputation site. Since the fin regenerated it suggests pObs were maintained well enough for un-impinged outgrowth and sp7:eGFP expression (green) indicates that cells are able to differentiate.

We hypothesized there was enough residual PRC2 activity in *ezh2* transheterozygotes to facilitate regeneration. We stained regenerating 72 hpa fins from *ezh2*$^{sa1199/-}$; *Tg(sp7:eGFP)* and wildtype clutchmates with antibodies to detect H3K27me3, Zns-5 (entire osteoblast lineage), and GFP (Figure S4.1). Wildtype clutchmates showed similar H3K27me3 as previously described with more H3K27me3 in the most distal pObs, decreased H3K27me3 in transitioning Obs and increased tri-methylation in more mature osteoblasts. H3K27me3 was most abundant in distal epidermis and basal epidermal cells (Fig. S4.1 top panels). Ezh2 activity was drastically decreased in transheterozygous fish. H3K27me3 remained present in *ezh2* transheterozygous distal basal epidermal cells but was virtually absent in osteoblasts and intra-ray mesenchymal cells (Fig. S4.1 bottom panels). We conclude that bulk H3K27me3 dependent on Ezh2/PRC2 is not required for caudal fin regeneration.

Combinatorial decrease in Ezh2 and Ezh1 drive regeneration defects.

The dispensability of Ezh2 for fin regeneration is reminiscent of neonatal mouse heart regeneration. Cardiomyocyte-specific conditional *Ezh2* mouse mutants also show decreased H3K27me3 (Ahmed et al., 2018; Ai et al., 2017) but, like *ezh2*$^{sa1199/-}$ zebrafish caudal fins, heart regeneration is unaffected. In contrast, Ezh1 is dispensable for all mouse development but required for neonatal heart regeneration (Ai et al., 2017). Therefore, we hypothesized that Ezh1 likewise may play essential roles during zebrafish bone regeneration.

We first performed RNAscope to look at *ezh1* expression during regeneration. Our preliminary findings indicate *ezh1* expression was similar to that of Ezh2. *ezh1* was found in osteoblasts with seemingly slight distal enrichment. Intra-ray mesenchyme *ezh1* expression was also enriched at the distal end of the regenerate and there were a few basal epidermal cells with low expression (Fig S4.2).

To evaluate if Ezh1 has a role during regeneration we amputated fins of *ezh1*$^{b1394/b1394}$ adults and found they continue to robustly regenerate (Fig. 4.5B). Ezh2 is able to fulfill roles of Ezh1 and the two are completely redundant in mouse intestinal crypt and hair follicle homeostasis (Ezhkova et al., 2011; Koppens et al., 2016). We considered that Ezh2 may partially substitute for Ezh1 during regeneration. We crossed *ezh1*$^{+/-}$*;*

ezh2$^{sa1199/-}$ to *ezh1*$^{-/-}$; *ezh2*$^{+/-}$ animals to generate *ezh1*$^{-/-}$; *ezh2*$^{sa1199/-}$ adults to assess regeneration when PRC2 activity was nearly completely ablated. Unfortunately, we were unable to recover *ezh1*$^{-/-}$; *ezh2*$^{sa1199/-}$ adults (Table. S4.1). Thus, we carried out regeneration experiments in *ezh1*$^{-/-}$; *ezh2*$^{+/-}$ adults.

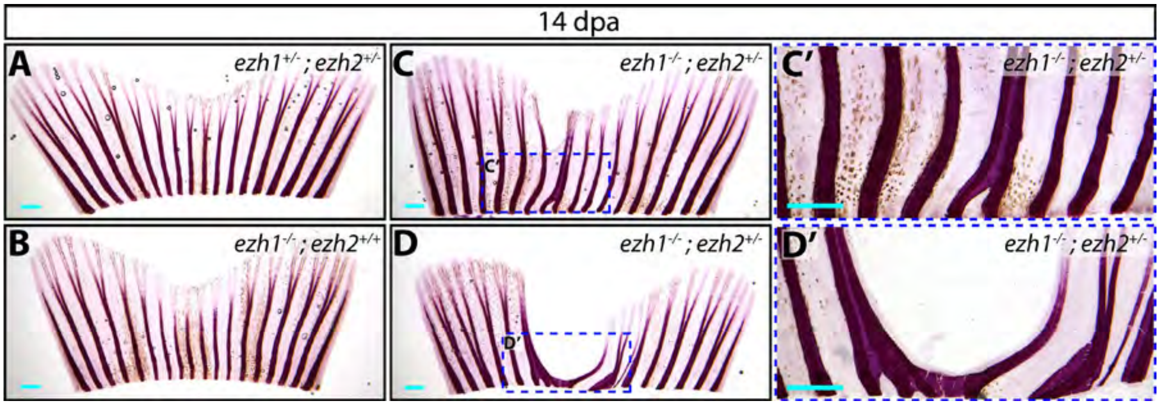

Figure 4.5. Loss of Ezh1 and decreased Ezh2 causes defects consistent with disorganized osteoblasts and maintenance failure during regeneration. (A-D') Alizarin red stained fins at 14 dpa from (A) *ezh1; ezh2* double heterozygous animals, (B) *ezh1*$^{-/-}$; *ezh2*$^{+/+}$ fish and (C-D') *ezh1*$^{-/-}$; *ezh2*$^{+/-}$ fish. (B) *ezh1* fish regenerate as well as (A) wildtype animals. Further loss of PRC2 activity (C-D') results in ray fusions and impaired fin outgrowth. Magnified inserts (C', D', boxed in blue dashed line) provided more detail of fusion events and decreased regeneration. Scale bars are 500 µm.

Caudal fins of *ezh1*$^{-/-}$; *ezh2*$^{+/-}$ adults developed normally (Fig. 4.6A). We amputated caudal fins of *Tg(sp7:eGFP)* fish and monitored regeneration over 7 days for regeneration defects. Peripheral (dorsal and ventral) rays largely regenerated normally, however central rays variably showed reduced regeneration and fusions between bony rays. At 72 hpa, sp7^{+} cells from two neighboring rays had merged together in *ezh1*$^{-/-}$; *ezh2*$^{+/-}$ animals (Fig 4.6B-B'). By 120 hpa, the fused rays appeared calcified together. Also, additional osteoblasts from neighboring ray appeared merged into common pools (Fig. 4.6C-C'). At 14 dpa we stained fins with alizarin red to assess calcification and structure of bony rays (Fig 4.5). *ezh1*$^{-/-}$; *ezh2*$^{+/-}$ osteoblasts still produced a calcified matrix. Interestingly, each hemiray acted independently of the other where one hemiray can fuse with an adjacent ray even if its opposing hemiray does not (Fig 4.5C-D'). The failure to outgrow is consistent with defects in pOb maintenance while bone fusions hint at cell disorganization. Taken together, we conclude that PRC2 is required to robustly restore the shape and size of regenerating fins.

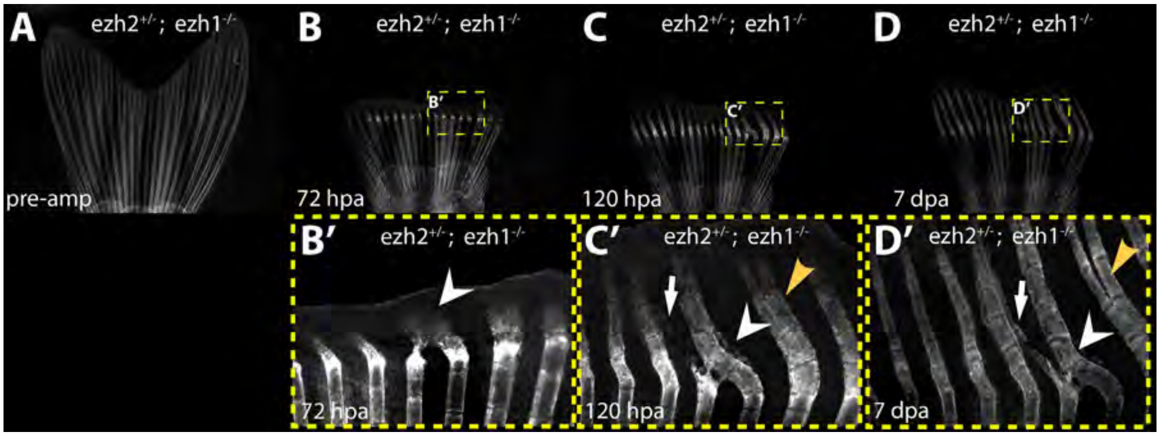

Figure 4.6. Osteoblast disorganization occurs early during regeneration. Live images of an *ezh1*$^{-/-}$; *ezh2*$^{+/-}$; *Tg(sp7:eGFP)* from (A) prior to amputation and (B-D') tracking bony ray formation over a week. Dashed yellow boxes provide (B', C', D') magnified views regeneration defects. White arrowhead points to a primary fusion event starting to form at 72 hpa (B-B'). At 120 hpa (C-C') a second fusion begins to occur (white arrow) and a ray branches before expected (yellow arrowhead). By 7 dpa (D-D') bone around these defects has formed.

DISCUSSION

This study explored requirement of Polycomb Repressive Complex 2 (PRC2) during regeneration. Previous studies implicated PRC2/H3K27me3 in mouse and zebrafish heart regeneration, zebrafish larval fin fold regeneration and adult caudal fin regeneration (Ai et al., 2017; Ben-Yair et al., 2019; Dupret et al., 2017; Stewart et al., 2009). However, earlier zebrafish tail regeneration studies lacked cellular resolution expression studies of the histone methyltransferase component of PRC2, Ezh2 and did not look at changes in

H3K27me3 in different cell types (Dupret et al., 2017; Stewart et al., 2009). We corroborate and expand on findings that Ezh2 is expressed during fin regeneration. We found Ezh2 has increased protein levels in distal progenitor cells of the osteoblast and intra-ray mesenchyme lineage. Osteoblasts and intra-ray mesenchymal cells also showed expression of *ezh1* transcripts, although less drastically enriched in distal tissues. *ezh1* was also expressed in some distal basal epidermal cells. H3K27me3 mostly mirrored Ezh2 and *ezh1* expression, but we were surprised to see higher levels of H3K27me3 in regions that had lower levels of Ezh2 or *ezh1*, such as in more differentiated proximal osteoblasts and distal basal epidermal cells. Increased Ezh2 expression suggested a key Ezh2/PRC2 role during regeneration. Yet, zebrafish retain the ability to regenerate caudal fins even when Ezh2/PRC2 function is greatly diminished. Lastly, $ezh1^{-/-}$; $ezh2^{+/-}$ fish develop caudal fins as wildtype fish would, but bony rays variably became stunted and disorganized during regeneration. Future studies will resolve whether this represents a unique Ezh1/PRC2 function or relatively high expression of Ezh1 over Ezh2 in a pertinent cell type.

H3K27me3 levels did not always match Ezh2 and *ezh1* expression. This is perhaps reflective of Kdm6 activity that has not been explored in extensive detail during regeneration. Also, of interest is increased H3K27me3 in both progenitor and mature osteoblasts. This is supportive of a model in which high H3K27me3 maintains distinct states – progenitor and differentiated – and decreased H3K27me3 lowers the barrier allowing for easier transition between states.

Ezh2 was expendable for caudal fin bone regeneration, as it is during mouse neonatal heart regeneration (Ahmed et al., 2018; Ai et al., 2017). Ezh1 is required for mouse heart regeneration but is dispensable for caudal fin regeneration when both copies of *ezh2* are intact. However, defects manifest during regeneration in *ezh1*$^{-/-}$*; ezh2*$^{+/-}$ fish. This suggests that Ezh1 plays a substantial role during regeneration that Ezh2 can fulfill until it too is diminished.

Abnormalities during regeneration consist of decreased bone outgrowth and fusions between bony rays. Reduced regeneration suggests failure to maintain osteoblast progenitors. The mechanism for progenitor osteoblasts depletion could come from internal and external factors. PRC2 promotes progenitor characteristics *in vitro* and during zebrafish development (Chapter III) and could be working similarly during regeneration. Ezh2 and *ezh1* are expressed in distal niche cells that secrete Wnt to maintain progenitor states. If PRC2 loss of function in these cells perturbs their existence or Wnt production, then it could result in loss of osteoblast progenitors as well. Fusion events also could be due to disorganized osteoblasts. It was recently described that *shha* expressing basal epidermal cells organized neighboring Runx2^{+} pObs at the distal end of regenerating fins (Armstrong, Henner, Stewart, & Stankunas, 2017). If this interaction is lost, or if basal epidermal cells themselves are disorganized then it could lead to muddled osteoblast movement.

One remarkable aspect about how zebrafish regenerate fins is that the many cell types that make up the fin remain lineage restricted when de-differentiated (Knopf et al., 2011; Sousa et al., 2011; Stewart & Stankunas, 2012; Tu & Johnson, 2011). If distal intra-ray Wnt producing cells fate switched to the osteoblast lineage, then we would predict quicker depletion of Wnt and consequently less pOb maintenance and stunted outgrowth as we see in *ezh1*$^{-/-}$*; ezh2*$^{+/-}$ fish. Loci-specific modulation of H3K27me3 could be the key to controlled de-differentiation without lineage switching. PRC2 deposits H3K27me3 to specify different cell types during development. Perhaps it is acting similarly during regeneration and loss of PRC2 activity lowers barriers that distinguish closely related cell types.

MATERIALS AND METHODS

Zebrafish

The University of Oregon Institutional Animal Care and Use Committee (IACUC) approved and monitored all zebrafish procedures following the guidelines and recommendations outlined by the Guide for the Care and Use of Laboratory Animals (National Academic Press). The following established lines were used in this study: *Tg(sp7:EGFP)b1212* (DeLaurier et al., 2010), *ezh2*^{sa1199} (Kettleborough et al., 2013), *ezh2*^{b1392} (Chapter III), and *ezh1*^{b1394} (Chapter III).

Immunostaining

Regenerating fins were collected at desired timepoints and fixed with 4%PFA in PBST overnight at 4°C. Samples were washed 3 times for 10 minutes with PBST then dehydrated into 100% ethanol. Samples were stored in 100% ethanol overnight, washed twice in xylenes for 10 minutes and then embedded in paraffin. Samples were sectioned at 7 µm thickness.

For immunofluorescent staining, sections were de-paraffinized by washing in xylenes 2 times for 10 minutes. Sections were then rehydrated into milliQ water and washed with PBST for 5 minutes. Antigen retrieval was performed using 1 mM EDTA and 0.1% Tween-20 and pressure-cooking for 5 minutes. Samples were then rinsed three times with PBST and blocked with 10% non-fat dry milk in PBST for one hour at room temperature. Samples were incubated with primary antibodies diluted in blocking solution overnight at 4^{o}C. Primary antibodies were used at the following concentrations: H3K27me3 (Cell Signaling Technologies, clone C36B11) 1:1000; Runx2 (Santa Cruz Biotechnology , clone 27-K) 1:500; GFP (Aves) 1:1000, Ezh2 (Cell Signaling Technologies, clone D2C9) 1:1000, Zns-5 (Zebrafish International Resource Center) 1:50. Slides were then rinsed 2 times followed by three 5 minutes washes in PBST. Sections were incubated in 0.5 M NaCl in PBST for 30 minutes and then rinsed two times with PBST. Samples then were incubated with Alexa-conjugated secondary antibodies (Invitrogen) diluted 1:1000 in block solution for one hour at room temperature. Slides were then rinsed twice and washed three times for 5 minutes with PBST, then incubated with Hoechst (Invitrogen) diluted 1:4000 in PBS, followed by two more 5 minute washes in PBS. Slides were mounted using Fluoro-gel (Electron Microscopy Sciences) and imaged on a Leica DM4000B upright microscope or Zeiss LSM880 laser scanning confocal microscopes.

RNAscope

RNAscope probes to detect *ezh1* mRNA were designed and synthesized by ACD Bio. RNAscope was performed using the Multiplex Fluorescent kit (ACD Bio) according to manufacturer's recommendations on paraffin embedded fin sections with minor modifications. Nuclei were visualized by Hoechst staining (Thermo Fischer). Imaging used Zeiss LSM880 laser scanning confocal microscopes.

Genotyping *ezh2* and *ezh1* mutants.

Described previously in Chapter III

Fin regeneration assessment and alizarin red staining

Fish carrying the mature osteoblast reporter *Tg(sp7:eGFP)* were imaged prior and immediately after caudal fin amputation using a Leica M205 FA stereoscope. Caudal fins were imaged every 24 hours for one week and assessed for GFP expression and regeneration defects.

For alizarin red staining, caudal fins from *ezh1;ezh2* fish of the desired genotype were amputated, allowed to regenerate for two weeks, harvested and stained as previously described (Armstrong et al., 2017). Alizarin stained fins were imaged on a Leica M165 FC stereoscope.

CHAPTER V

CONCLUSIONS

Here, I describe how molecular signaling and epigenetic factors affect progenitor maintenance and ultimately organ size and shape. We used transcriptomics data to help characterize specialized cells occupying distinct regions of the regenerating fin. We also identified the cellular source of Wnt required for regeneration and demonstrated how this population determines correct amount of fin regenerative growth. Additionally, we implicated PRC2 in having developmentally contextual roles in fate determination, cell state stabilization, and progenitor maintenance.

In Chapter II, we show perdurance of a Wnt producing population dictates final length of a regenerating fin. Previous studies had already established that Wnt was required for caudal fin regeneration (Stewart et al., 2014; Stoick-Cooper et al., 2007; Wehner et al., 2014), but the notion that natural depletion of a Wnt source slows and eventually terminates regeneration is novel. A key finding in this work was identifying Dach as a molecular marker of the Wnt-producing population that we could use to follow these “niche” cells over the course of regeneration. In addition, we found that dorsal/ventral rays and proximal amputations produced a larger Dach$^+$ population and were less sensitive to Wnt inhibition than medial rays and distal amputations. Initial niche population size correlated with the amount of tissue that needed to be regenerated. Ultimately, we found that niche size is determined by ray volume and were able to derive a predictive mathematical model for fin regeneration. Our findings show that a regenerating fin may “know” when to stop regenerating based on its skeletal geometry rather than cell memories. Along with the novelty of the other findings in the chapter, this final observation is perhaps the most novel in directly contradicting prevailing models of positional identity. Our model is fully supported by our findings and it is an eloquent explanation for how a fin restores size after resection.

In Chapter III, I made key findings determining how Ezh2 promotes craniofacial bone development and axial skeleton pattern. I also made insights into how PRC2 instructs cell decisions. Unlike mouse zygotic *ezh2* mutants (O'Carroll et al., 2001), *ezh2*-null zebrafish remarkable survive for about two weeks post fertilization with few overt defects. I used CRISPR/Cas9 to make *ezh2* and *ezh1* mutants and evaluated how PRC2 contribute to craniofacial bone development. Using *in vitro* and *in vivo* assays I determined that Ezh2 promotes an osteoblast progenitor state. Ezh1 alone has indiscernible roles during development, although *ezh1; ezh2* double mutants present with slightly worse formed craniofacial bones suggesting some partial redundancy. I identified an *ezh2* hypomorph and showed how this allele produces low levels of functional protein and can produce loss of function phenotypes. Importantly, this allele was used to make inferences in the role of Ezh2 in cell fate decisions later in development. In addition, this allele was used to show homeotic transformations in the axial skeleton, the first in a vertebrate model due to *ezh2* mutation.

The work in Chapter IV evaluated potential PRC2 roles during regeneration. We found during our developmental studies that PRC2 promotes osteoblast states and plays a role in cell fate decisions. During regeneration, mature cells de-differentiate in a lineage restricted manner to produce osteoblasts that then must be maintained for regenerative outgrowth (Knopf et al., 2011; Sousa et al., 2011; Stewart et al., 2014; Stewart & Stankunas, 2012; Tu & Johnson, 2011; Wehner et al., 2014). If progenitor cells are not sustained or if cells change fate, fins would have reduced growth and potentially be malformed. We first identified expression patterns of Ezh2 at 24 hpa and 72 hpa, H3K27me3 abundance at 72 hpa, and *ezh1* expression at 96 hpa. Using mutants from Chapter III, we found that while Ezh2 is required for development, it is likely dispensable during regeneration. This was similarly true in regenerating neonatal mouse hearts (Ahmed et al., 2018; Ai et al., 2017). Conversely, Ezh1 is expendable during development but required for regeneration in mice (Ai et al., 2017). We found that *ezh1*$^{-/-}$; *ezh2*$^{+/-}$ adults develop fins normally, but manifest with defects consistent with loss of progenitors and fate switching during regeneration. Fins regularly regenerated with fusions between bony rays and reduced outgrowth. These defects could also be due to osteoblast organization failure due to flaws in osteoblast-basal epidermal cell interactions or the basal epidermal cells themselves.

These studies contribute valuable insights into understanding how organs develop the correct size and shape. It is intuitive that final organ size is dependent on number of cells, and for those cells to appropriately respond to cues. However, understanding how cells are allocated and coordinated to become an organ of the correct size is not as clear. Specific to fin regeneration, we identified the regenerative progenitor niche, how initial size of the niche is determined, and found that its gradual depletion reduces Wnt production and acts as a timer to end regeneration. With further investigation, our model could be applicable to other systems and organisms. This model disputes popular models of fin cells having distinct, cryptic positional identities that further must be restored during regeneration. What controls niche depletion is still a mystery that could be answered by investigating long-finned mutants. We found Ezh2 and *ezh1* are expressed in the niche and possibly could be maintaining Dach$^+$ cells. Determining what cell(s) are affected by PRC2 perturbations will help resolve how PRC2 contributes to robust regeneration.

APPENDIX

SUPPLEMENTAL MATERIAL

SUPPLEMENTAL FIGURES

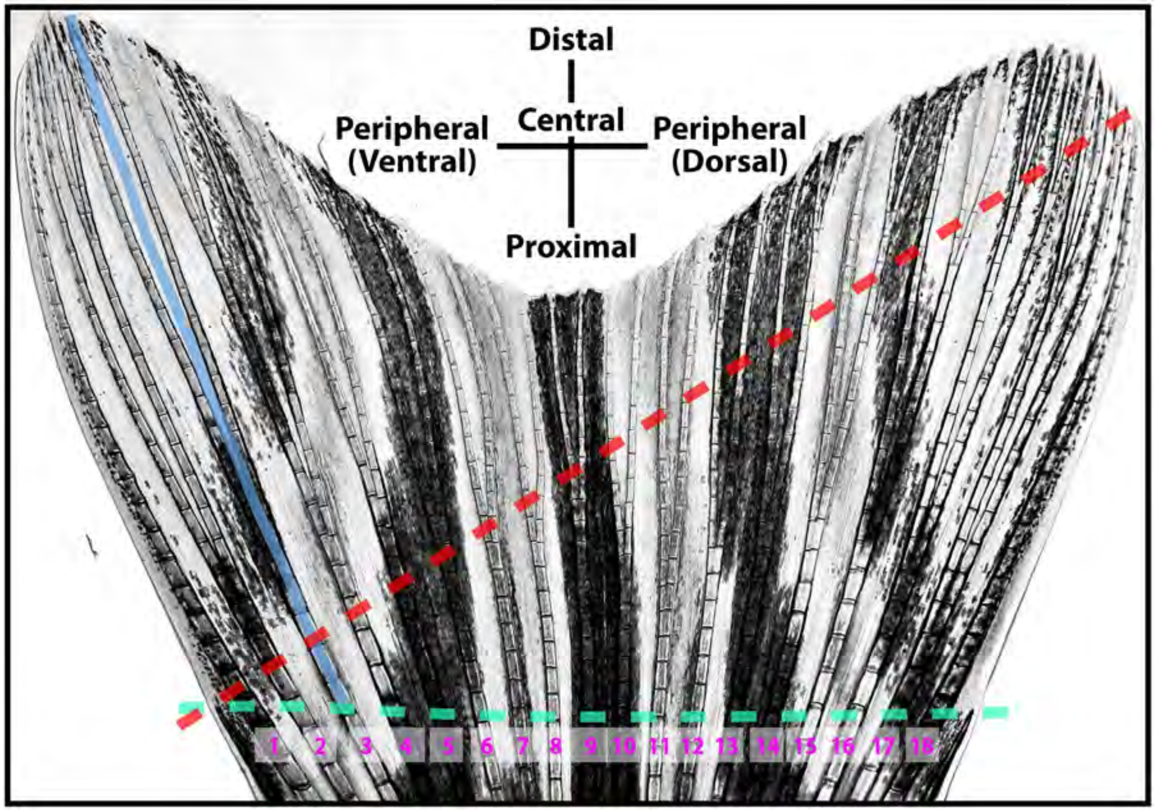

Supplemental Figure 2.1. A zebrafish caudal fin showing amputation positions and orientation/numbering conventions. A high resolution stitched differential interference contrast (DIC) image of an uninjured adult caudal fin. The dashed green line shows the standard proximal-distal amputation plane spanning between the tips of the un-numbered, truncated peripheral “mini-rays”. Diagonal fin amputations follow the dashed red line, starting from the tip of the ventral-most “mini-ray”, passing through ray 16’s second branch-point, and continuing straight through the dorsal edge. Length measurements (blue line) are from a real or theoretical amputation position to the fin’s tip. To accommodate branching, the line is drawn directly in between branches of a mother ray. The terms “central” and “peripheral” distinguish ray position relative to a fin’s center or either edge.

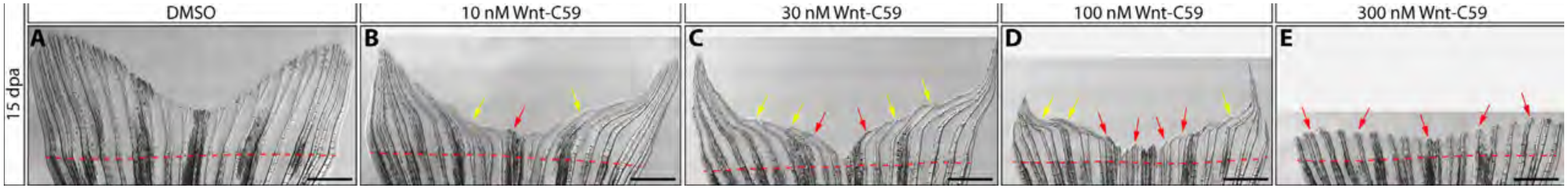

Supplemental Figure 2.2. Wnt production correlates with regenerative "demand". (A-E) Stitched differential interference contrast (DIC) images of regenerated caudal fins 15 days post amputation (dpa) with exposure to DMSO (A) or indicated concentrations of the Wnt-secretion inhibitor Wnt-C59 (B-E). Small molecule exposures began at 4 dpa until imaging at 15 dpa. Yellow and red arrows point to regions with reduced or failed regeneration after drug addition, respectively. The amputation plane is indicated with a dashed red line. Scale bars are 1 mm.

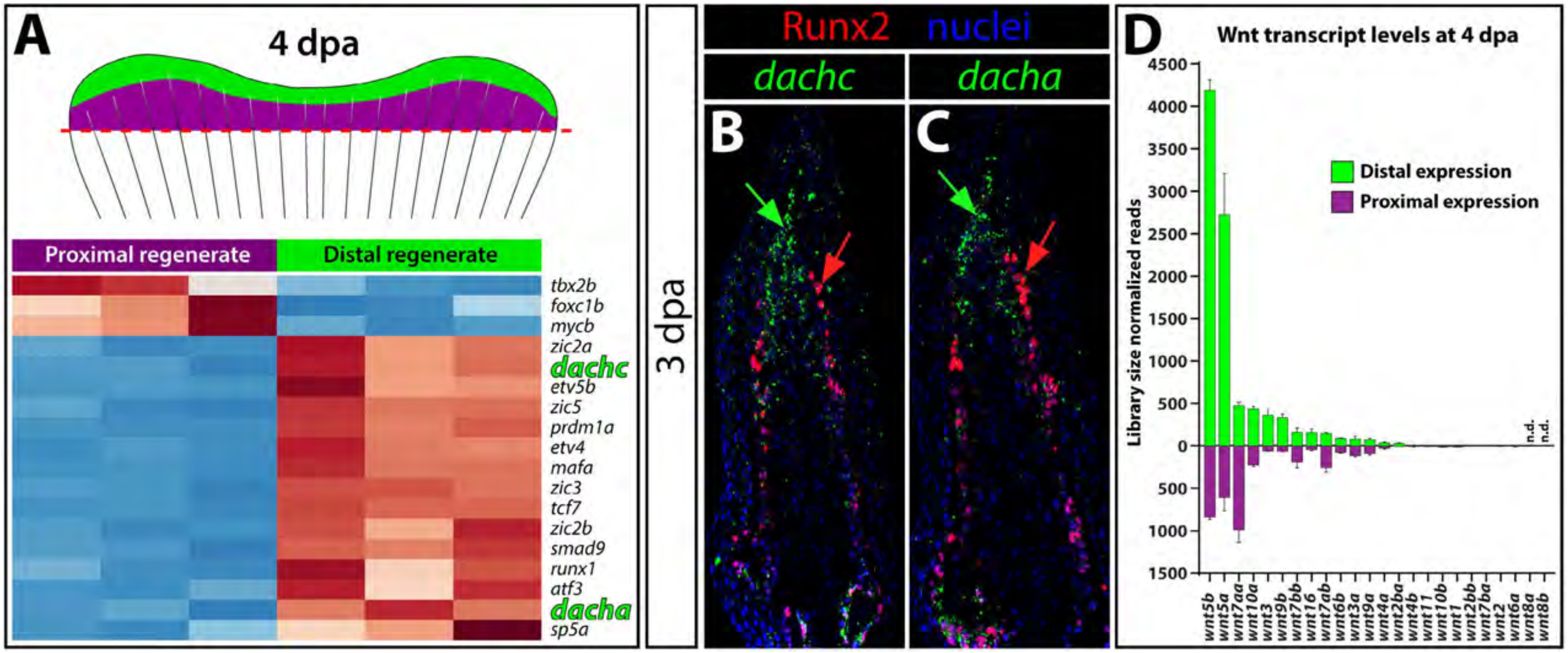

Supplemental Figure 2.3. *dacha* and *dachc* expression define the distal Wnt-producing niche. (A) RNA-Seq analysis comparing distal Wnt-expressing vs. proximal differentiating tissue from 4-day post-amputation (dpa) regenerating fin tissue. The heat map illustrates relative enrichment (red = higher, blue = lower) of differentially expressed transcriptional regulators ($p < 0.05$ and at least 3-fold difference) for each replicate. **(B-C)** In situ hybridization (in green) for *dachc* (B) and *dacha* (C) mRNAs, combined with immunostaining for Runx2 (red) on 3 dpa fin sections. Hoechst-stained nuclei are blue. Red arrows indicate Runx2-expressing osteoblasts that lack *dacha/c* expression. Green arrows point to the *dacha/c*-expressing distal niche. **(D)** Bar graph showing the library size-normalized transcript counts of all 24 zebrafish *wnt* genes in distal and proximal 4 dpa fin regenerate tissue. The genes are ordered by descending expression levels. *wnt5b* and *wnt5a* have the highest distal transcript levels and are distally enriched. Means of the three replicate pooled samples are shown. Error bars show one standard deviation.

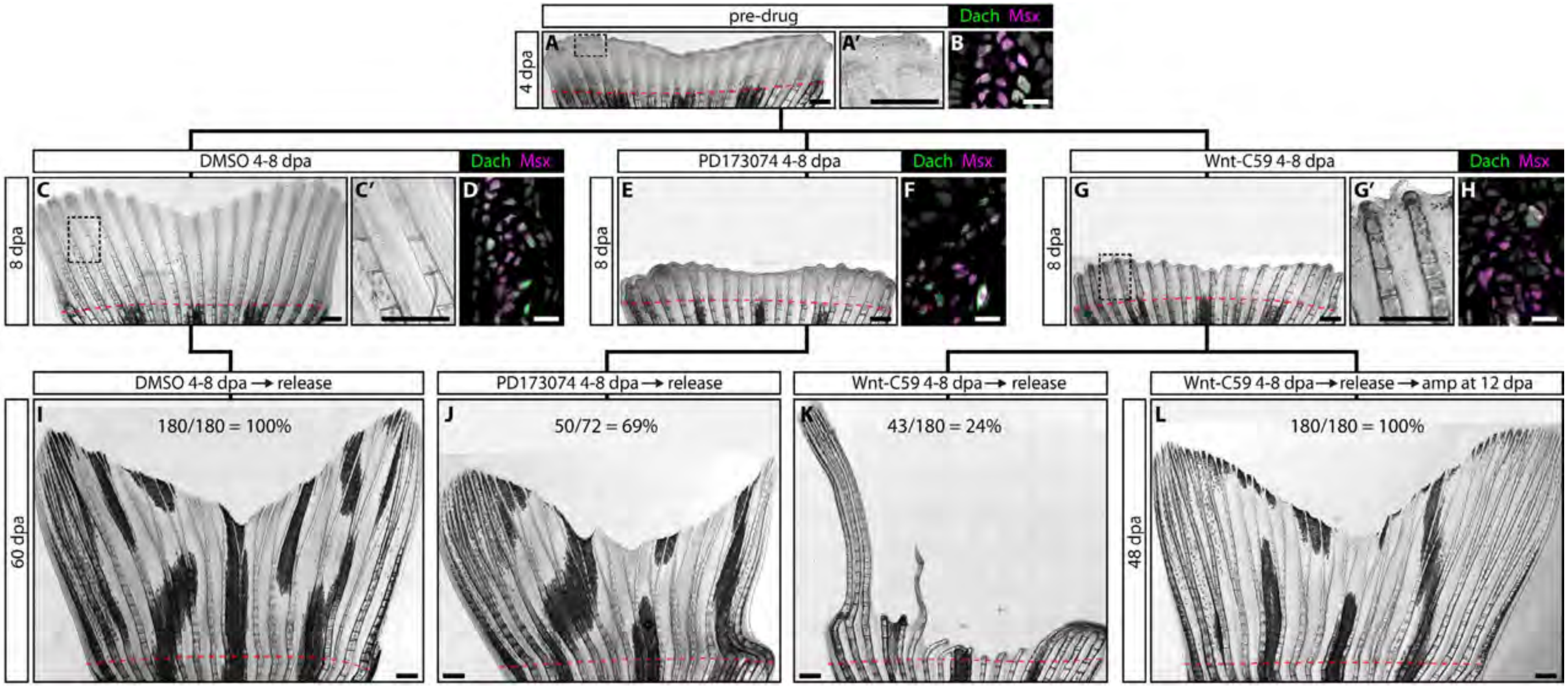

Supplemental Figure 2.4. Inhibition of Wnt signaling depletes the Dach$^+$ niche and irreversibly blocks regeneration. The black lines connecting figure panels establish a tree diagram showing the experimental workflow. Top row: caudal fins from clutchmate animals are resected and allowed to regenerate through 4 dpa. Middle row: At 4 dpa, animals are treated with DMSO, the FGFR inhibitor PD173074, or the Wnt secretion inhibitor Wnt-C59 until 8 dpa. Bottom row: Animals are then transferred to fish water and allowed to completely regenerate. For (L), fins are re-amputated at 12 dpa proximal to the original amputation site. Whole mount fin images use stitched differential interference contrast (DIC) microscopy. **(A)** A representative fin at 4 dpa. The region bound by the dashed box is shown at high magnification (A') to emphasize how distal tissue is undifferentiated. **(B)** A distal regenerate section from a 4 dpa fin immunostained with Dach (green) and Msx (magenta) antibodies. Niche cells express both transcription factors. **(C, C', E, G, G')** 8 dpa regenerated fins from DMSO (C, C'), PD173074 (E), and Wnt-C59 (G, G') exposed animals. FGF or Wnt inhibition prevents outgrowth past the 4 dpa time of drug addition. However, Wnt is not required for bone differentiation or joint formation (compare G' with A'). (**D, F, H**) 8 dpa sections immunostained with Dach (green) and Msx (magenta) antibodies. Dach-expressing niche cells persist upon FGFR inhibition but are lost when Wnt production is blocked. **(I-K)** Fin images at 60 dpa after treatment from 4-8 dpa with DMSO (I), PD173074 (J), or Wnt-C59 (K). Unlike FGFR inhibition, Wnt inhibition irreversibly blocks outgrowth. **(L)** A Wnt-C59 treated animal (from 4-8 dpa) subjected to a secondary amputation at 12 dpa and allowed to regenerate until 48 dpa. A secondary amputation effectively "resets" the outgrowth timer by establishing a new niche, allowing regeneration to resume. For (I-L), the number of rays that regenerated normally is shown for each treatment (n = 10 fish for each condition). A dashed red line indicates the amputation plane. Scale bars are 500 μm for whole mount images and 25 μm for immunostained sections.

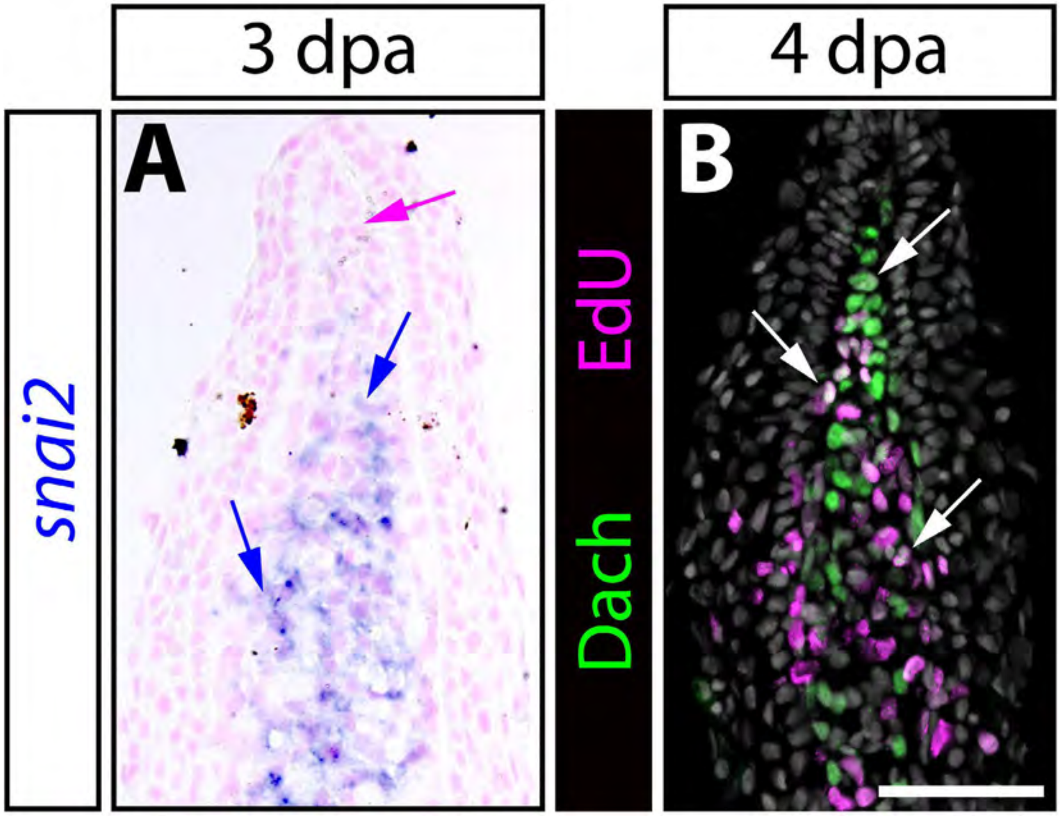

Supplemental Figure 2.5. Intra-ray mesenchymal cells down-regulate *snai2* when transitioning to a Dach$^+$ niche state that remains proliferative. (A) Visualization of *snai2* mRNA (in blue) by in situ hybridization on a 3 dpa fin section. The tissue is counterstained with Nuclear Fast Red. Blue arrows indicate *snai2*-expressing blastema mesenchyme. The magenta arrow highlights the *snai2*-negative niche. **(B)** Paraffin section of a 4 dpa regenerating caudal fin stained for EdU incorporation (four-hour EdU exposure; magenta) and Dachshund (Dach; green) expression. Nuclei are in grey. Scale bar is 50 μm. White arrows denote Edu$^+$/Dach$^+$ cells found throughout the niche population.

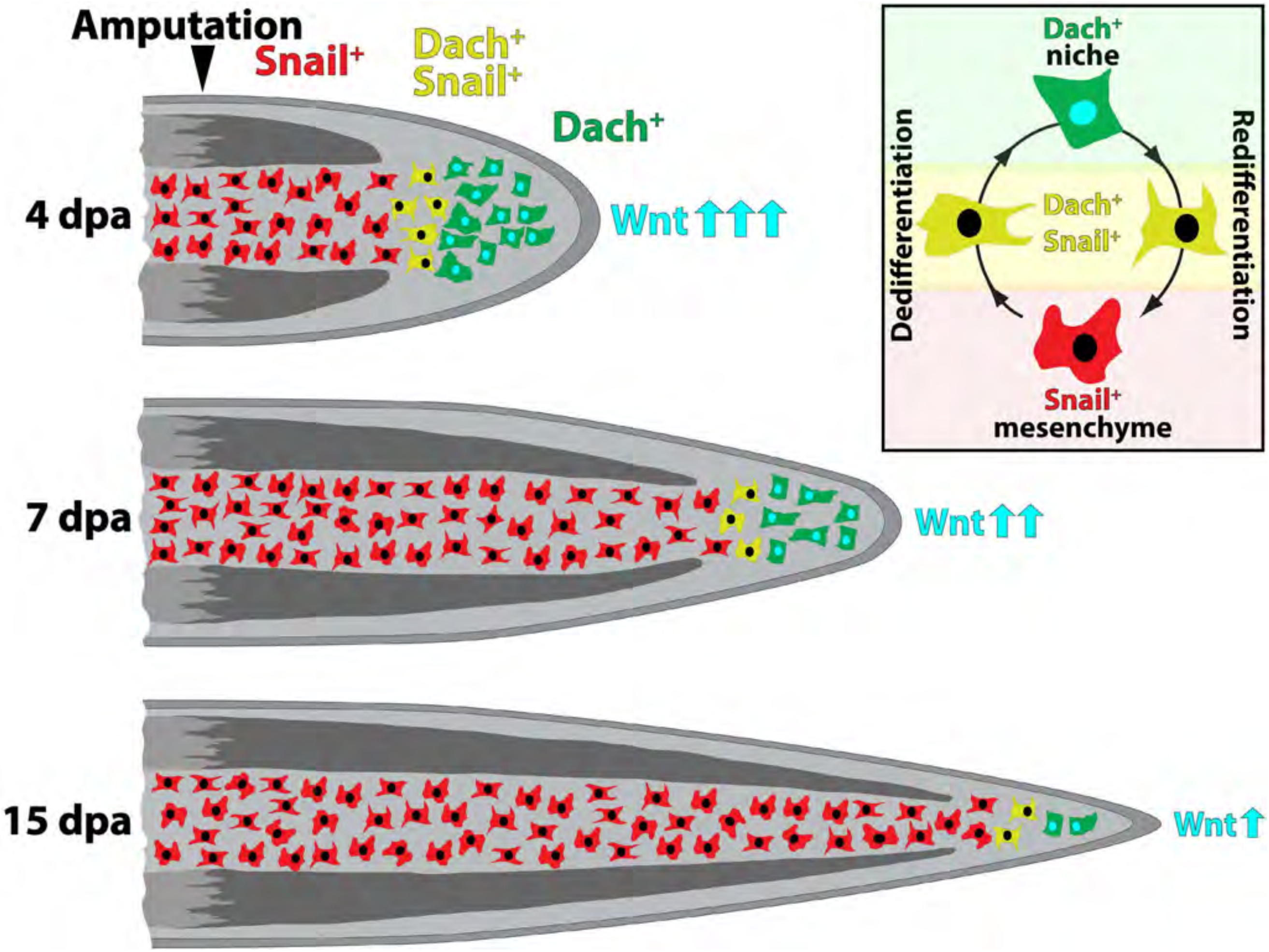

Supplemental Figure 2.6. Graphic depicting the progressive depletion of the Wnt-producing, Dach-defined niche population during fin regeneration. Dach$^+$ niche cells originate from Snail-expressing intra-ray mesenchyme released into the forming blastema upon injury. The size of the niche population, and therefore Wnt levels, decreases as the fin regenerates and niche cells transition back into a Snail$^+$ mesenchymal state.

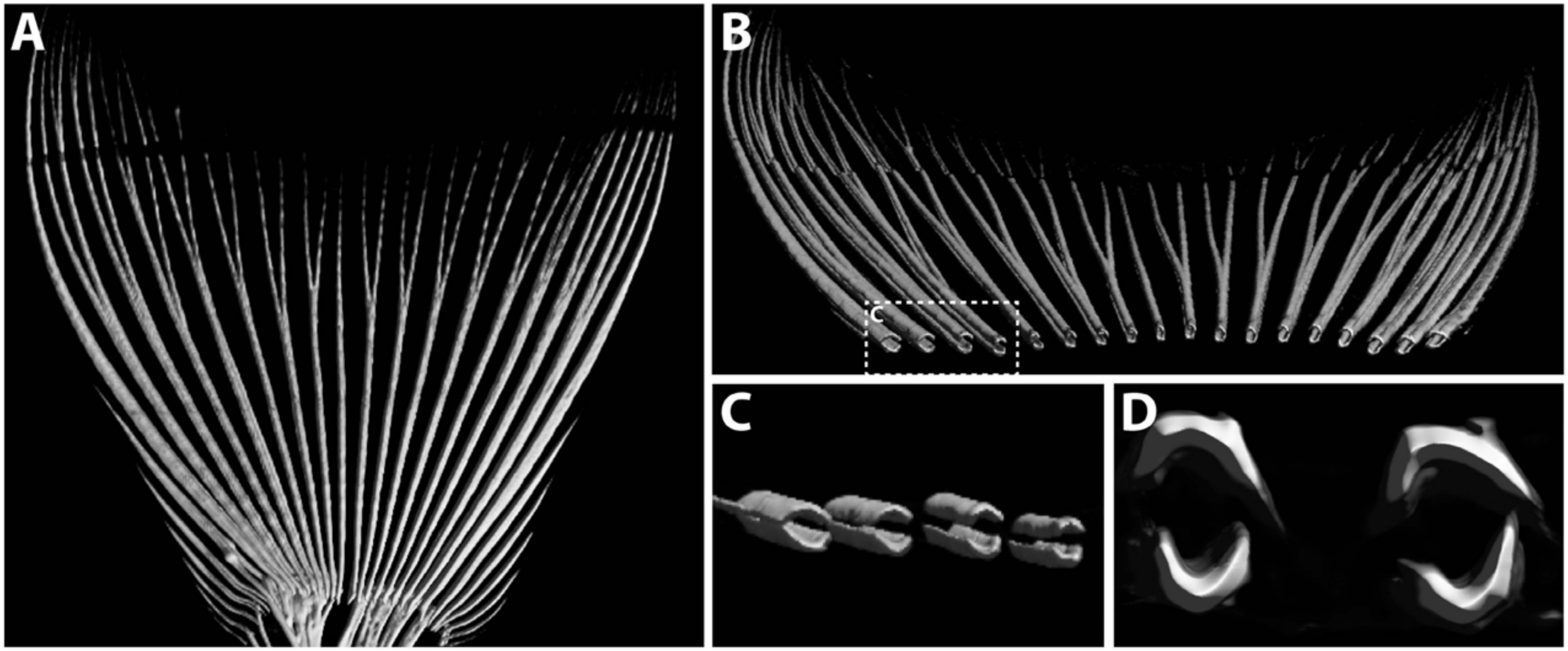

Supplemental Figure 2.7. Micro-CT analysis shows bony rays across the caudal fin are variably sized, tapered, and cylindrical. (A-C) 3-D micro-computed tomography images of an adult zebrafish caudal fin highlighting its (A) bony ray skeleton, (B) differentially sized and tapering rays, (C) the cylindrical shape of the intra-ray space between hemi-rays and (D) its approximately circular cross-sectional area.

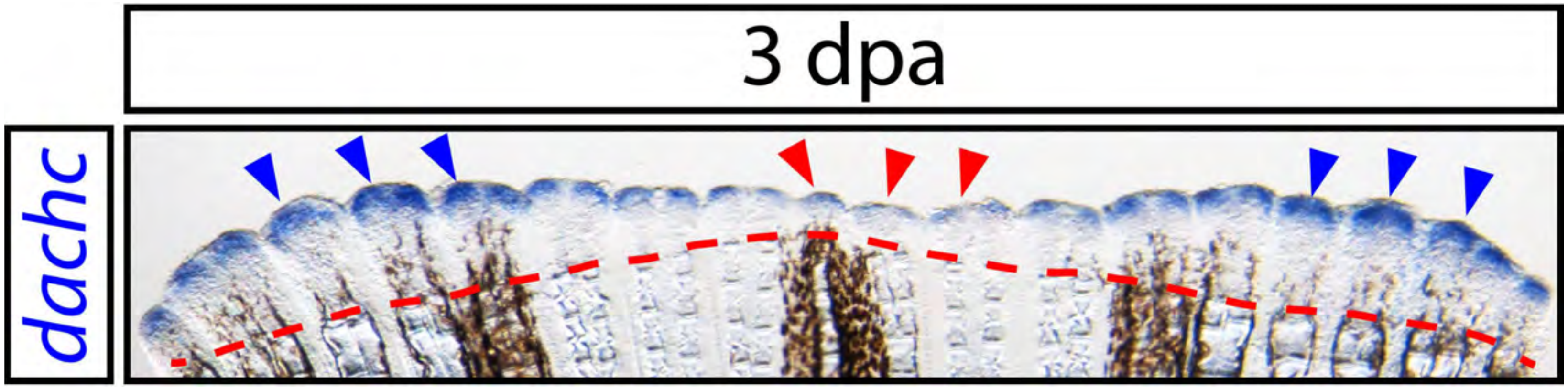

Supplemental Figure 2.8. Differential niche production across the dorsal-ventral axis during fin regeneration. Whole mount in situ hybridization on a 3 dpa fin using a *dachc* probe to visualize distal niche cells (in blue). Blue arrowheads indicate peripheral fin regions with pronounced and broad *dachc* expression indicative of robust niche cell pools. Red arrowheads point to central fin tissue with modest *dachc* signal due to relatively small niche cell populations. The dashed red line marks the amputation plane.

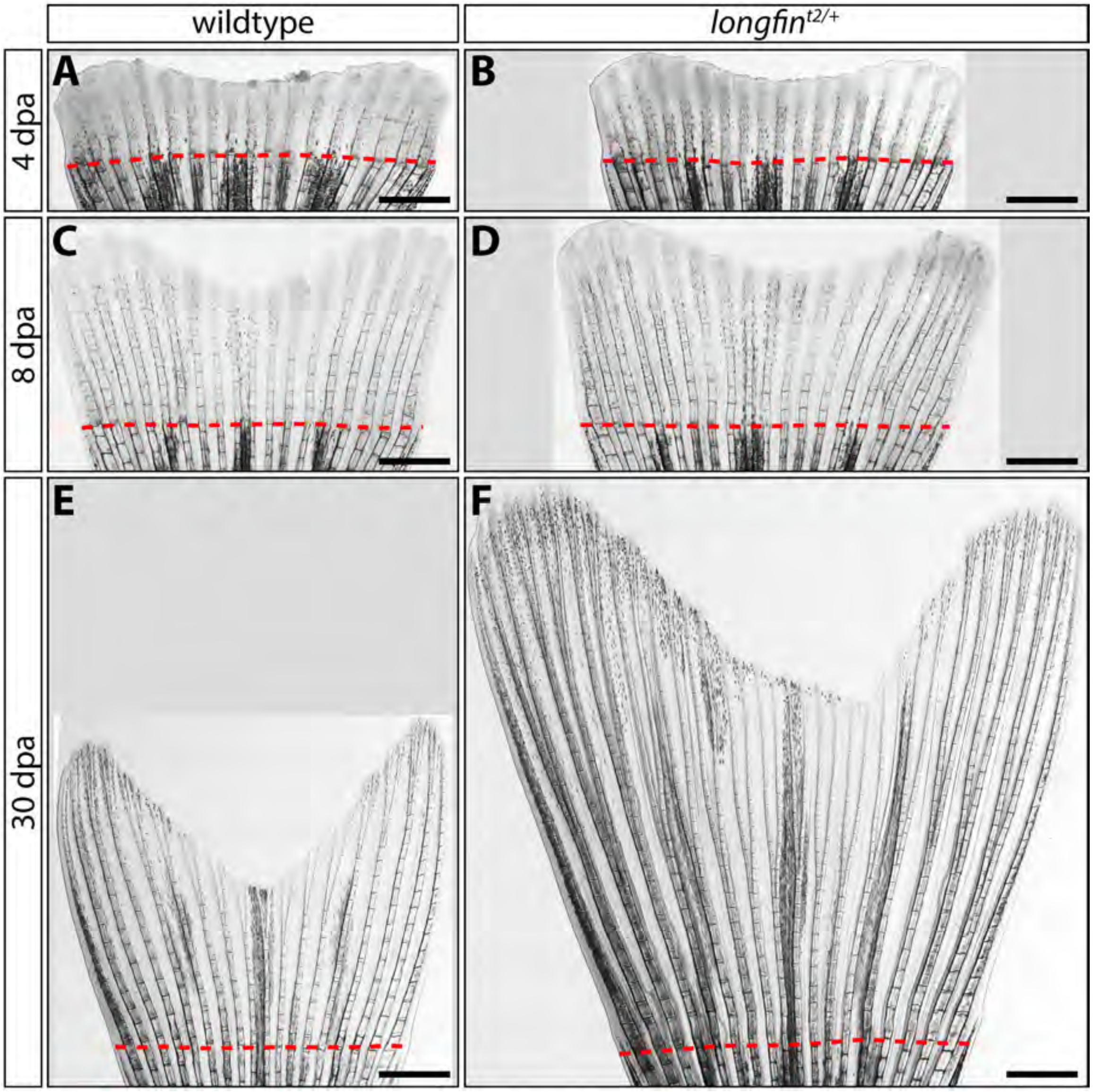

Supplemental Figure 2.9. Regenerative outgrowth of *longfin*$^{t2/+}$ caudal fins fails to decelerate. (A-F) Stitched differential interference contrast (DIC) microscope images of caudal fins from clutchmate wildtype and *longfin*$^{t2/+}$ animals at the indicated day post amputation (dpa). Outgrowth is similar through 8 dpa but persists in *longfin*$^{t2/+}$ fish, leading to exceptionally long fins by 30 dpa. Quantitative data for the entire time course ($n \geq 12$) is shown in Fig. 2.4. Dashed red lines highlight amputation planes. Scale bars represent 1 mm.

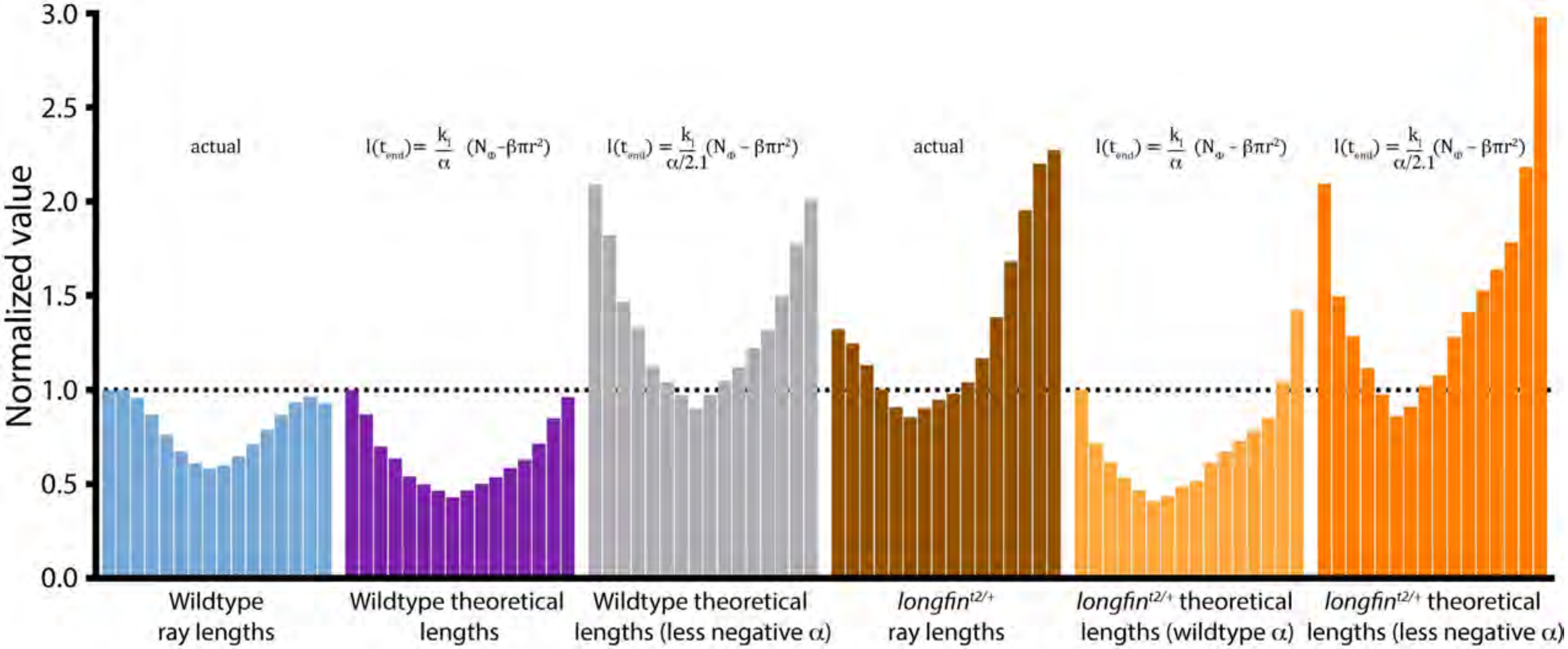

Supplemental Figure 2.10. *longfin* fin ray skeletal geometry and modeled regenerative outgrowth suggests *longfin* have deficient niche depletion – a broken "countdown timer". Each distinctly colored set of distributed bars represents actual ray lengths or theoretical regenerated ray lengths for the 16 central rays (from a fixed proximal-distal position). All ray lengths are normalized to the longest wildtype ray. Theoretical lengths are derived from the transpositional scaling equation, which predicts final length as a function of ray radius, with scaling parameters set to restore the widest wildtype ray to its actual length. The alpha parameter (α) then is increased by 2.1x (by dividing α, a negative number, by 2.1; empirically set by linear regression comparing wildtype and *longfin* ray area to length relationships) to model a decreased rate of niche depletion that would cause wildtype resected rays to theoretically regenerate to a *longfin*$^{t2/+}$ length. Applying this same increase in α but inputting *longfin*$^{t2/+}$ ray radii into the transpositional scaling formula successfully predicts *longfin*$^{t2/+}$ fin-resected fish would regenerate with a *longfin* phenotype.

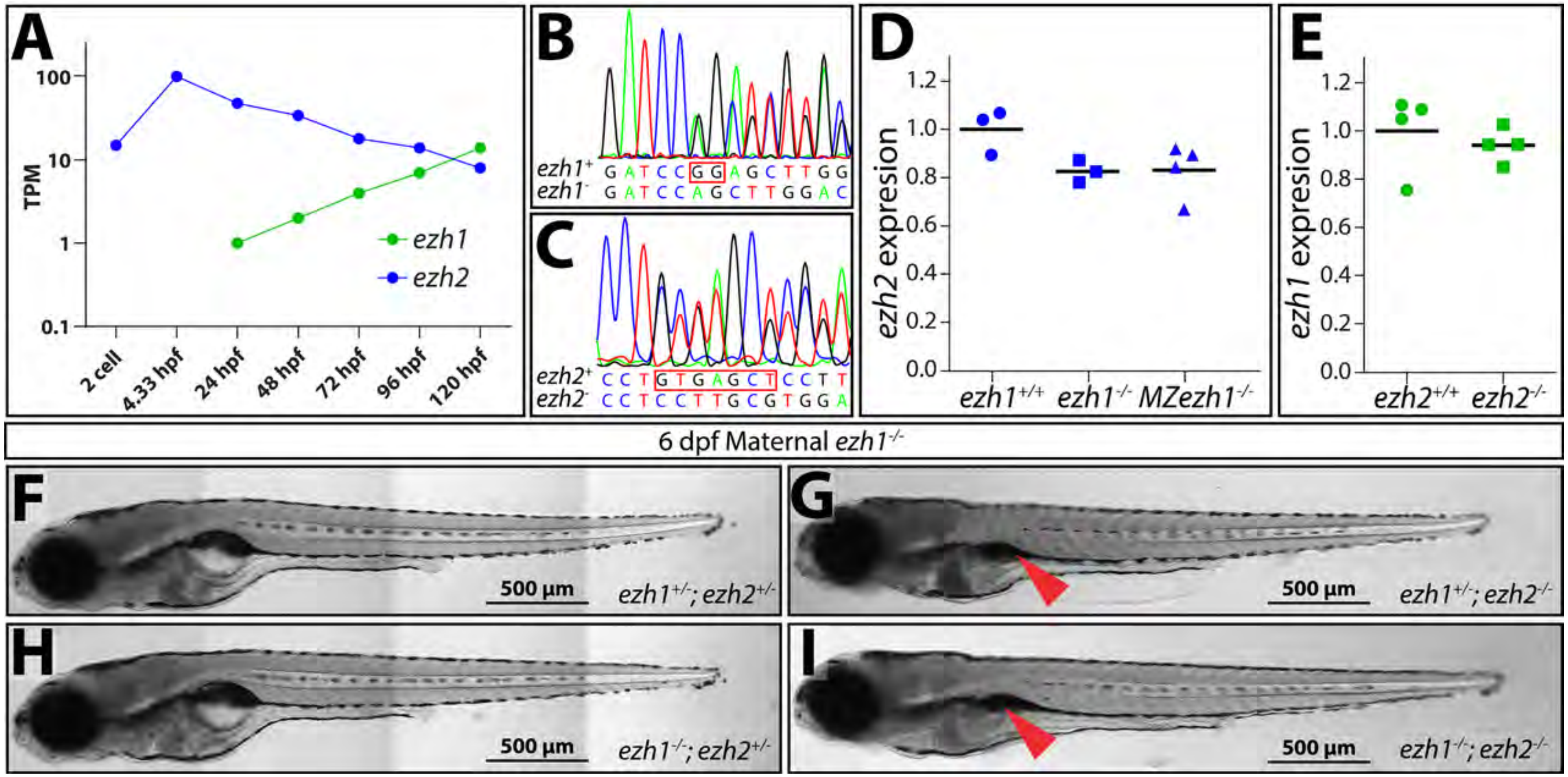

Figure S3.1. Maternal-zygotic *ezh1* mutants are viable and do not exacerbate overt *ezh2* defect. (A) Line graph, generated from mined RNAseq data (White et al., 2017), of *ezh1* (green) and *ezh2* (blue) expression in wildtype samples from 2-cell stage to 5 dpf. (B-C) Chromatograms of sequenced amplicons from an (B) *ezh1* heterozygous and an (C) *ezh2* heterozygous larvae surrounding the CRISPR/Cas9 generated mutations (boxed in red). (D) Scatterplot of qRT-PCR data comparing *ezh2* transcripts in 3 dpf wildtype, $ezh1^{-/-}$ clutchmates, and $MZezh1^{-/-}$ larvae. (E) Scatterplot showing a lack of genetic compensation by *ezh1* in *ezh2* homozygous mutants as assayed by qRT-PCR. (F-I) Whole mount differential interference contrast (DIC) microscopy images of 6 dpf maternal *ezh1* mutant siblings. Red arrowhead indicating under-inflated swim bladder of $ezh2^{-/-}$ larvae. Scale bar = 500 µm.

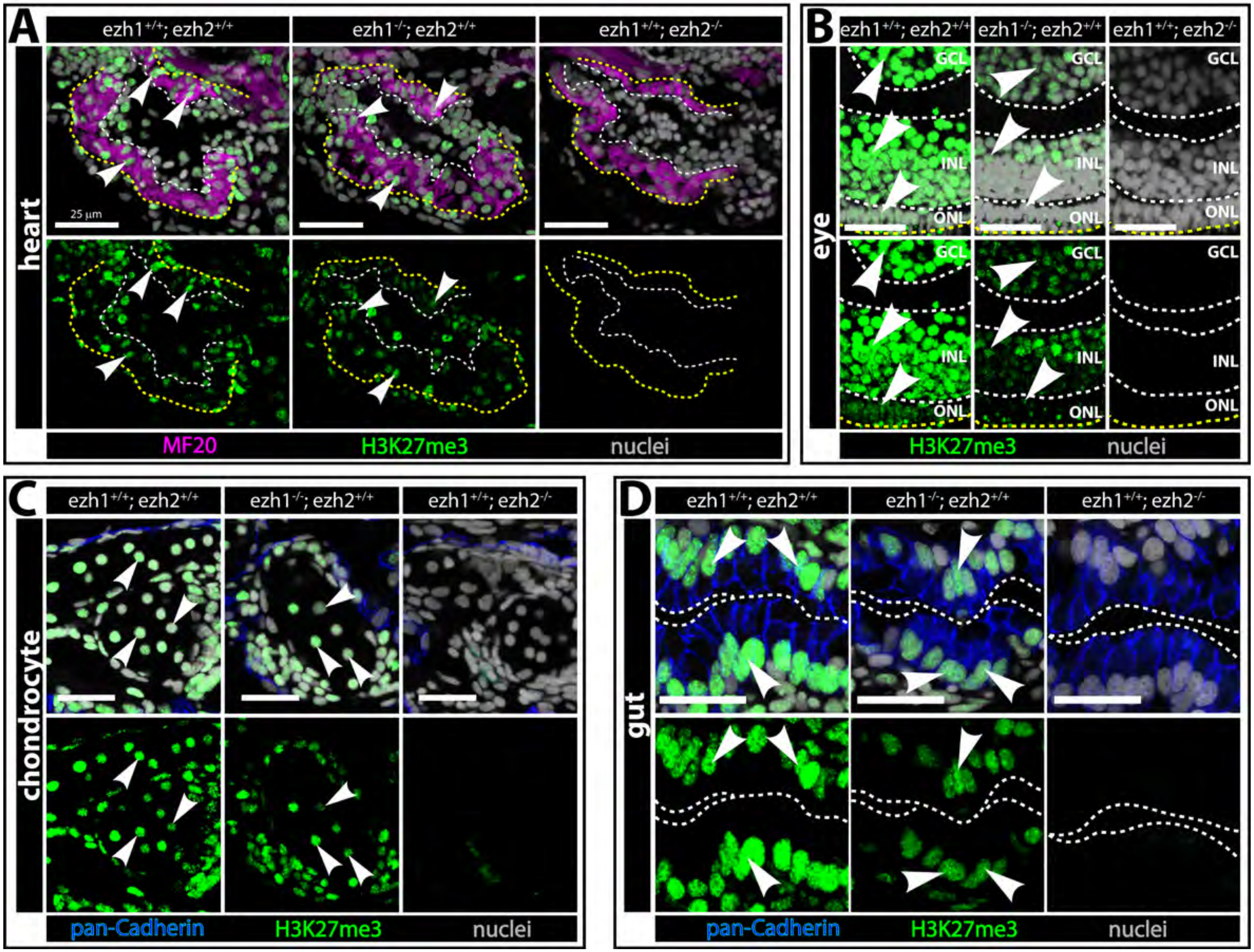
A
ezh1+/+; ezh2+/+
ezh1-/-; ezh2+/+
ezh1+/+; ezh2-/-
heart
25 µm
MF20
H3K27me3
nuclei
B
ezh1+/+; ezh2+/+
ezh1-/-; ezh2+/+
ezh1+/+; ezh2-/-
eye
GCL
INL
ONL
H3K27me3
nuclei
C
ezh1+/+; ezh2+/+
ezh1-/-; ezh2+/+
ezh1+/+; ezh2-/-
chondrocyte
pan-Cadherin
H3K27me3
nuclei
D
ezh1+/+; ezh2+/+
ezh1-/-; ezh2+/+
ezh1+/+; ezh2-/-
gut
pan-Cadherin
H3K27me3
nuclei

Figure S3.2 (previous page). Ezh1 alone ineffectively maintains H3K27me3. Max projections of confocal images of sectioned (A) heart, (B) eye, (C) craniofacial chondrocyte and (D) gut from wildtype, *ezh1* and *ezh2* mutants at 6 dpf. Samples immunostained with antibodies to detect myosin heavy chain (MF20, magenta), H3K27me3 (green) and pan-cadherin (blue). (A) Heart ventricle outlined with dashed yellow line. Inside of cavity outlined in white. White arrowheads point to H3K27me3$^+$ cardiomyocytes. (B) White dashed lines separate ganglion cell layer (GCL), inner nuclear layer (INL) and outer nuclear layer (ONL) of the eye. Yellow dashed line outlines outer boundary of the eye. White arrowheads indicate H3K27me3$^+$ cells in each layer. (C) White arrowheads pointing to H3K27me3$^+$ chondrocytes of the lower jaw. (D) Dashed white line indicates the boundary between intestinal cells and intestinal lumen. White arrowheads point to H3K27me3$^+$ intestinal cells. Scalebars in all panels are 25 μm.

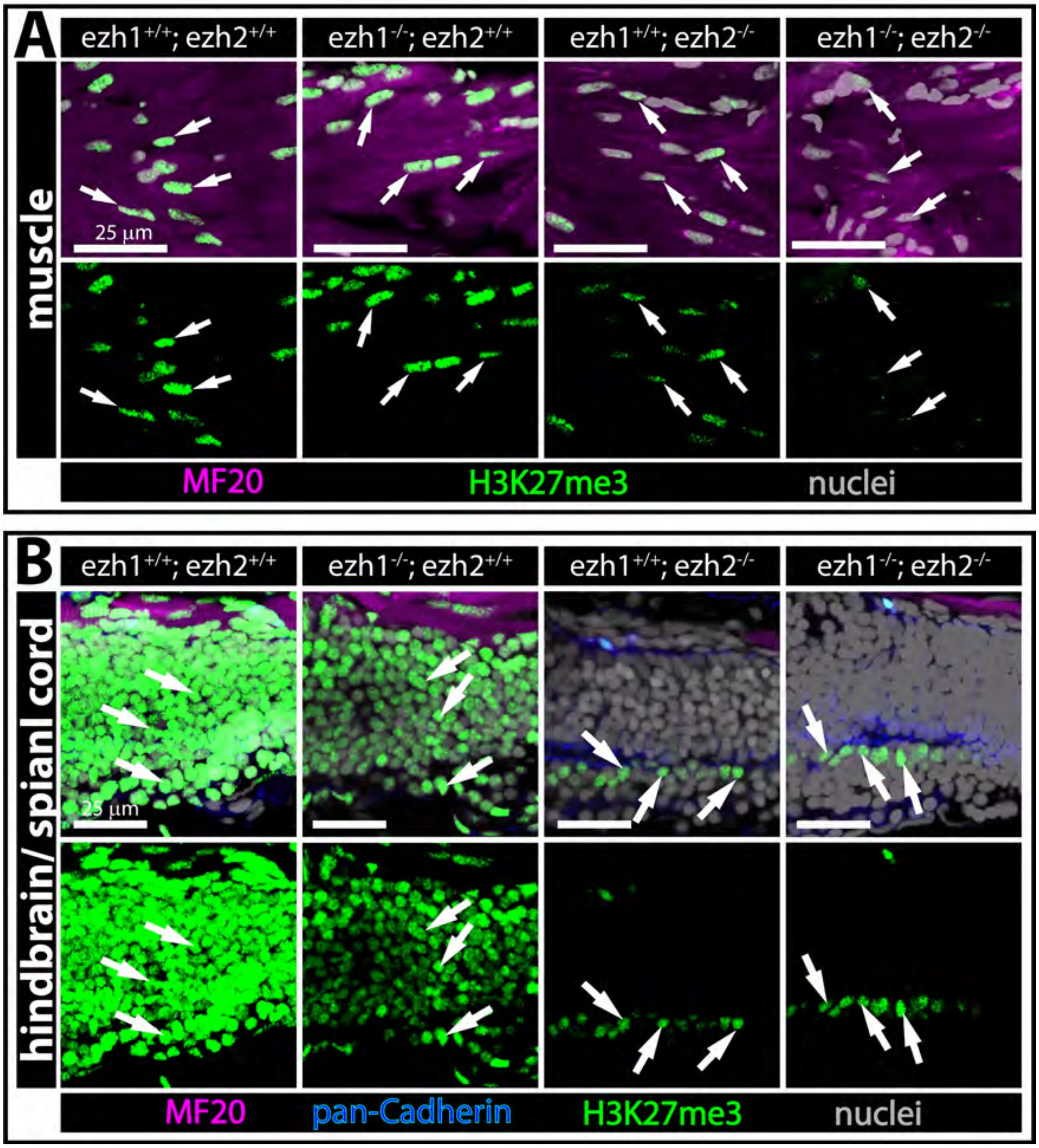

Fig S3.3 (previous page). Residual H3K27me3 is retained despite loss of zygotic H3K27me3 methyltransferases. Max projection confocal images of wildtype, *ezh1*, *ezh2*, and double mutant sectioned (A) skeletal muscle and (B) nervous system tissue at 6 dpf. (A) Some skeletal muscle (MF20, magenta) cells retain low levels of H3K27me3 (green) even in the absence of zygotic Ezh2 and Ezh1 (far right panels). Similarly, H3K27me3 (green) is detected in nervous tissue (B) of $ezh2^{-/-}$; $ezh1^{-/-}$ larvae. White arrows indicating H3K27me3^{+} cells. All scalebars are 25 µm.

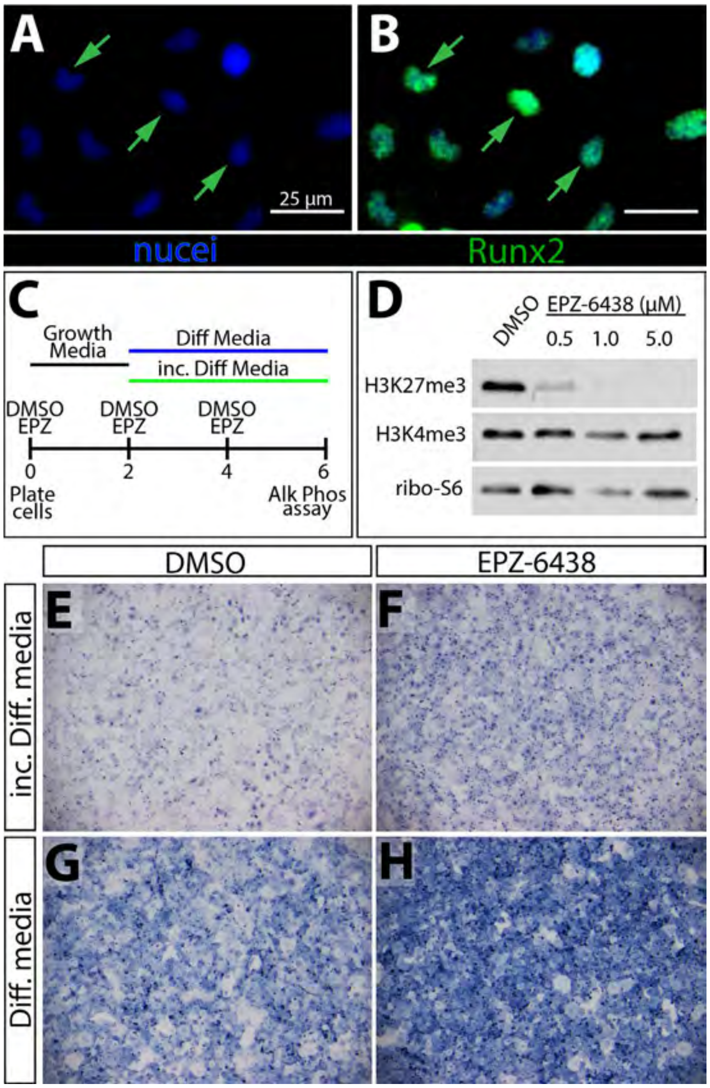

Figure S3.4. Ezh2 represses osteoblast maturation *in vitro*. (A-B) Immunofluorescent staining of AB9 cells using Runx2 (green) antibodies, confirming osteoblast identity. Green arrows point to examples of Runx2^{+} nuclei (blue). Scale bar is 25 µm (C) Diagram of treatment scheme to inhibit Ezh2 in AB9 cells using the small molecule EPZ-6438 (Tazemetostat). AB9 cells were plated and treated with either DMSO or EPZ-6438 for 48 hours in growth media. 48 hours after initial plating, cells were switched from growth medium to either incomplete or complete differentiation media and treated again with DMSO or drug. Drug was added once more at day 4 and then cells were assayed for alkaline phosphatase activity, indicator of osteoblast differentiation, at 6 days post plating. (D) Immunoblot on whole cell lysates from AB9 cells treated for four days with DMSO or different concentrations of EPZ-6438 using antibodies against H3K27me3, H3K4me3, and ribosomal protein S6 (loading). (E-H) AB9 cells treated with either DMSO or EPZ-6438 and differentiated in either incomplete or complete differentiation media and then assayed for alkaline phosphatase activity (blue) to test for osteoblast differentiation. Ezh2 inhibited cells more readily differentiated even incomplete differentiation medium conditions.

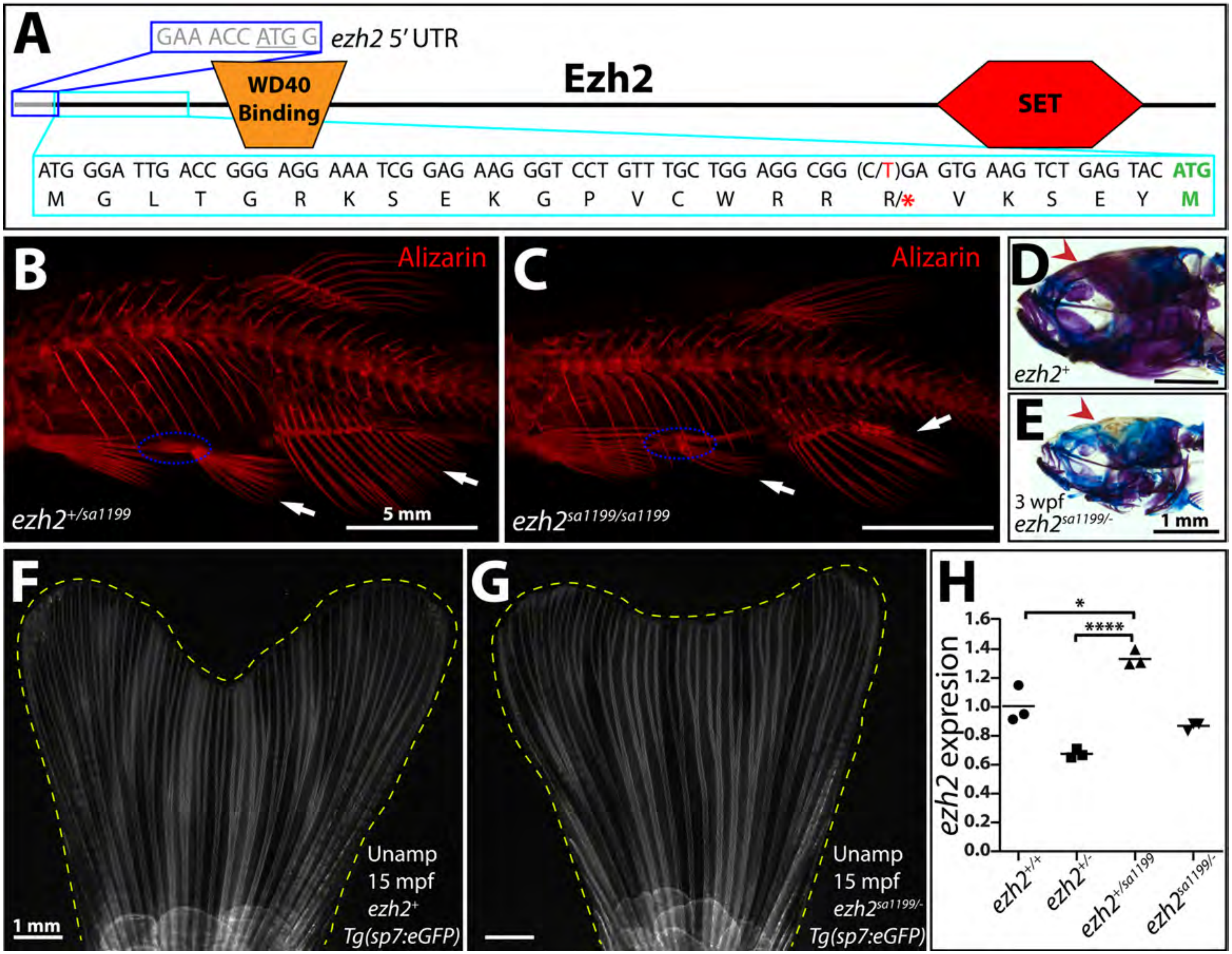
A
GAA ACC ATG G
ezh2 5′ UTR
Ezh2
WD40 Binding
SET
ATG GGA TTG ACC GGG AGG AAA TCG GAG AAG GGT CCT GTT TGC TGG AGG CGG (C/T)GA GTG AAG TCT GAG TAC ATG
M G L T G R K S E K G P V C W R R R/* V K S E Y M
B
Alizarin
ezh2+/sa1199
5 mm
C
Alizarin
ezh2sa1199/sa1199
D
ezh2+
E
3 wpf
ezh2sa1199/-
1 mm
F
1 mm
Unamp
15 mpf
ezh2+
Tg(sp7:eGFP)
G
Unamp
15 mpf
ezh2sa1199/-
Tg(sp7:eGFP)
H
ezh2 expresion
1.6
1.4
1.2
1.0
0.8
0.6
0.4
0.2
0.0
*
****
ezh2+/+
ezh2+/-
ezh2+/sa1199
ezh2sa1199/-

Figure S3.5 (previous page). *ezh2^{sa1199}* transcripts likely escape nonsense mediated decay and generate a truncated functional Ezh2 from a downstream translation start site. (A) Schematic of Ezh2. Grey and boxed in blue is Kozak sequence of *ezh2*. First 24 residues and codons are boxed in cyan. The *ezh2^{sa1199}* point mutation is 52C>T (red), resulting in R18stop (red asterisk). A potential downstream translation start site at M24 (bold, green) would generate a truncated protein containing all functional domains of Ezh2. (B-C) 5 month post fertilization *ezh2* wildtype and *ezh2$^{sa1199/sa1199}$* clutchmates stained with alizarin red (red). Adult *ezh2$^{sa1199/sa1199}$* (C) have fewer bony rays in pelvic and anal fins (white arrows) and have a reduced pelvic girdle (dashed blue oval). (D-E) Alcian blue (cartilage) and alizarin red (bone) stained heads of three-week old (D) wildtype and (E) transheterozygote clutchmates. Red arrowheads emphasize the lack of calcification of *ezh2$^{sa1199/-}$* cranium; a phenotype consistent with having fewer osteoblasts. (F-G) Wholemount live images of caudal fins from adult *Tg(sp7:eGFP)* (grey) wildtype (F) and *ezh2$^{sa1199/-}$* (G) clutchmates. Fins are outlined in yellow dashed line. (H) Scatter plot of *ezh2* expression obtained by qRT-PCR using cDNA from mRNA isolated from adult fin regenerates of clutchmates from an *ezh2$^{+/-}$* x *ezh2$^{+/sa1199}$* breeding. Expression normalized to *ezh2$^{+/+}$* samples after being normalized to *rpl8* (reference gene). Interestingly, fish with a copy of *ezh2^{sa1199}* have more *ezh2* transcripts than expected; potentially contributing to survivability of transheterozygous and *ezh2$^{sa1199/sa1199}$* fish. Statistical significance determined by Student's two-tailed *t*-test. * = P-value < 0.05, **** = P-value < 0.0001.

Figure S3.6 (next page). Maternal-zygotic *ezh2* mutants present with defects of numerous tissues. (A-G) Wholemount DIC images of maternal-zygotic *ezh2* mutants and wildtype clutchmates at (A-C) two dpf, (D-E) 4 dpf, and (F-G) 6 dpf. Black arrows point to edema that starts around the heart at two dpf (B) and progressively spreads throughout the body cavity with age (E, G). Black arrowheads indicating thinning of yolk extension at two dpf (B-C). Yellow arrowhead showing loss of bulbous morphology of the anterior intestine in mutants. Abnormal muscle appearance pointed at by red arrowheads. Dashed white ovals emphasize eye size. Magenta arrowheads point to abnormal position of ceratohyal cartilage in mutants (E, G). Scale bar = 500 µm. (H-J) Hemotoxin and eosin stained sections of 6 dpf siblings from a ♀ *ezh2$^{sa1199/sa1199}$* x ♂ *ezh2$^{+/-}$* cross. (H, J) Pancreatic tissue (outlined in blue dashed line, labeled with "P") and hepatic tissue (I, J, outlined in green dashed line, labeled with "L") are present in transheterozygous offspring. Blue arrow indicating lack of columnar shape of intestinal epithelial cells (J) compared to wildtype clutchmates (I). Scale bar is 100 µm.

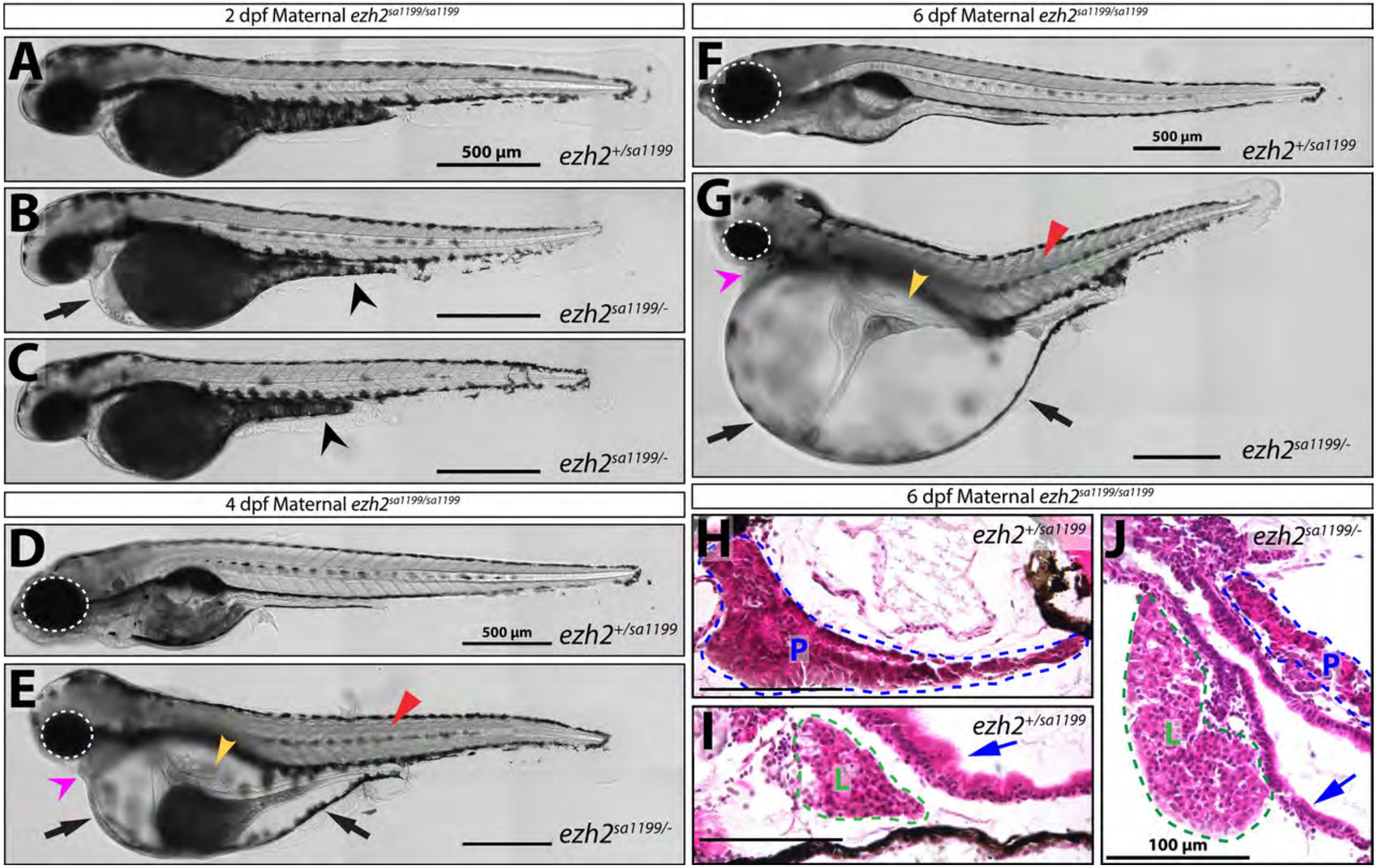
2 dpf Maternal $ezh2^{sa1199/sa1199}$
A
500 µm
$ezh2^{+/sa1199}$
B
$ezh2^{sa1199/-}$
C
$ezh2^{sa1199/-}$
4 dpf Maternal $ezh2^{sa1199/sa1199}$
D
500 µm
$ezh2^{+/sa1199}$
E
$ezh2^{sa1199/-}$
6 dpf Maternal $ezh2^{sa1199/sa1199}$
F
500 µm
$ezh2^{+/sa1199}$
G
$ezh2^{sa1199/-}$
6 dpf Maternal $ezh2^{sa1199/sa1199}$
H
$ezh2^{+/sa1199}$
P
I
$ezh2^{+/sa1199}$
L
J
$ezh2^{sa1199/-}$
P
L
100 µm

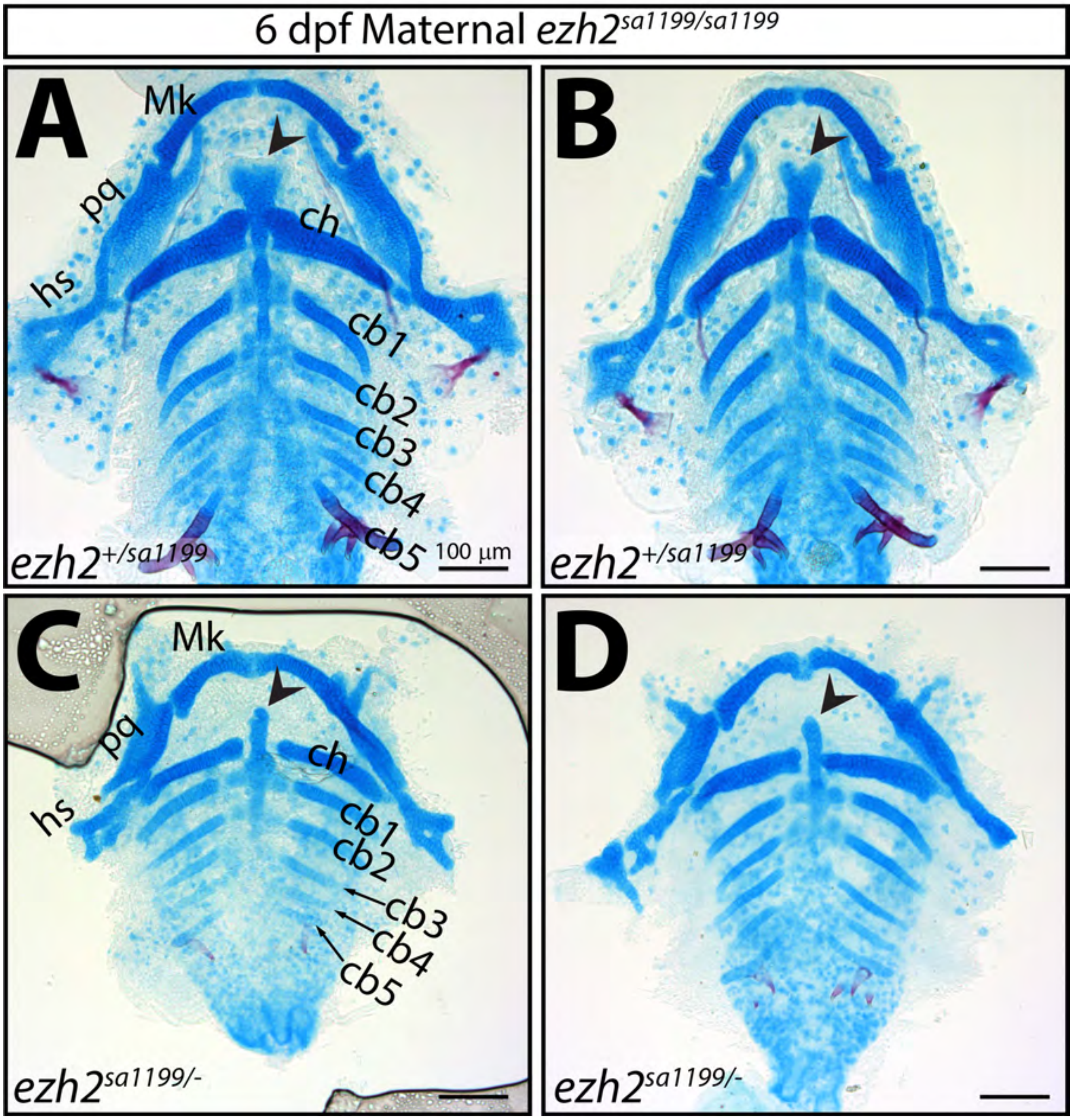

Figure S3.7. Maternal and zygotic Ezh2 promote skeletal shape and structure. (A-D) Flatmount ventral views of alcian blue (chondrocytes) and alizarin red (bone) stained viscerocranium from *Mezh2*$^{sa1199/sa1199}$ (A-B) *Zezh2*$^{+/sa1199}$ and (C-D) *Zezh2*$^{sa1199/-}$ clutchmates. Ceratobranchial cartilage is present yet diminished in maternal-zygotic mutants. Similarly, the basihyal (arrowhead) is smaller and fails to fan out in *M*^{sa1199}*Zezh2*$^{sa1199/-}$ (C-D) compared to wildtype siblings (A-B). Abbreviations: Mk, Meckel's cartilage; pq, palatoquadrate; hs, hyosymplectic; ch, ceratohyal; cb, ceratobranchial. Scale bar is 100 µm.

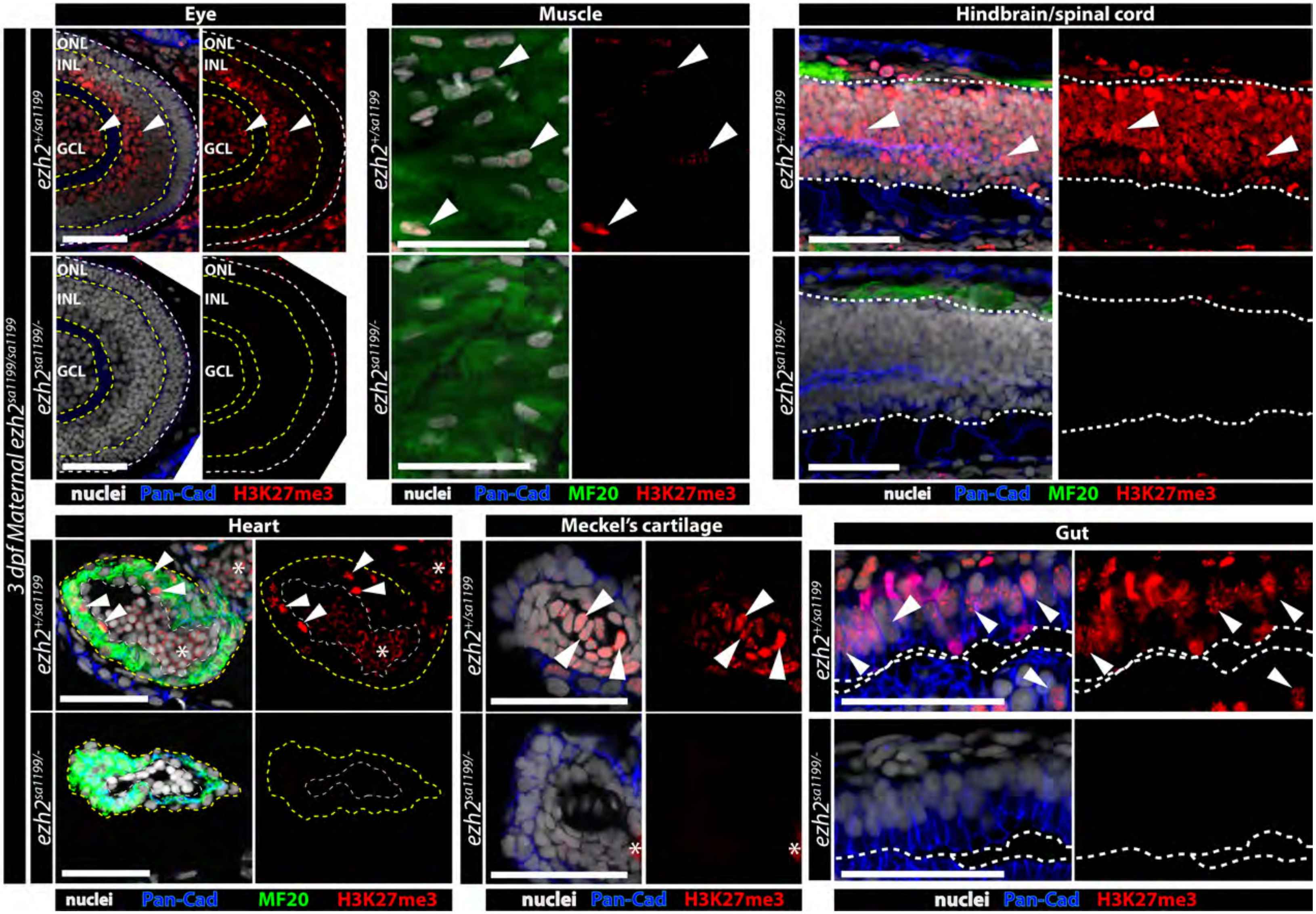
3 dpf Maternal ezh2sa1199/sa1199
Eye
ezh2+/sa1199
ezh2sa1199/-
ONL
INL
GCL
nuclei Pan-Cad H3K27me3
Muscle
nuclei Pan-Cad MF20 H3K27me3
Hindbrain/spinal cord
nuclei Pan-Cad MF20 H3K27me3
Heart
*
nuclei Pan-Cad MF20 H3K27me3
Meckel's cartilage
nuclei Pan-Cad H3K27me3
Gut
nuclei Pan-Cad H3K27me3

Figure S3.8 (previous page). H3K27me3 is virtually absent in $M^{sa1199}Z^{sa1199/-}$ animals. Confocal images of sectioned eye, muscle, nervous tissue, heart, chondrocytes and gut from maternal zygotic mutant and zygotic wildtype clutchmates at 3 dpf. Sections were stained for pan-Cadherin (blue), myosin heavy chain (MF20, green), and H3K27me3 (red). Outer boundary of eyes is outlined in white dashed line. Yellow dashed lines separate the outer nuclear layer (ONL), inner nuclear layer (INL) and ganglion cell layer (GCL) of the eye. White dashed line of nervous tissue outlines hindbrain/spinal cord. Heart ventricle is outlined in yellow dashed line. Inner cavity of the ventricle is outlined in white dashed line. Intestinal lumen is separated from intestinal cells by white dashed line. White arrowheads point to H3K27me3$^+$ cells. Asterisks mark autofluorescence. All scalebars are 50 µm.

Supplemental Movie 3.1. Expansion of the opercle osteoblast field, and not onset of osteoblast maturation, contributes to misshapen bones. Time-lapse imaging of wildtype (left) and *ezh2*$^{-/-}$ (right) clutchmates carrying the *Tg(sp7:eGFP)* reporter (grey) from 52 hpf until 72 hpf. GFP is detected ~55 hpf in both larvae. Scalebar is 50 µm.

Supplemental Movie 3.2. Ezh2 promotes osteoblast migration. Wildtype (left) and *ezh2*-null (right) clutchmates monitored from 76 hpf until 96 hpf for osteoblast maturation (sp7:eGFP, grey. Mild expression in the ectoderm) and migration. Branchiostegal ray 3 (BSR3) osteoblasts appear stagnant in *ezh2*$^{-/-}$ larvae compared to wildtype osteoblasts that expand along the anteroposterior axis. Scalebar is 50 µm.

Figure S4.1 (next page). H3K27me3 is nearly absent in transheterozygous fins. Immunostaining of wildtype (top panels) and *ezh2*$^{sa1199/-}$ (bottom panels) fins at 72 hpa. Sectioned tissue was stained for Zns5 (pan osteoblasts, blue), GFP (green) and H3K27me3 (red). Green arrowheads point to regions where osteoblasts concurrently gain sp7 expression and have decreased H3K27me3. Magenta arrowheads point to regions where maturing osteoblast acquire more H3K27me3 as they further re-differentiate. White arrows showing high H3K27me3 in wildtype basal epidermal cells and existent H3K27me3 in basal epidermal cells of transheterozygous fish. Black asterisks denote autofluorescence from red blood cells.

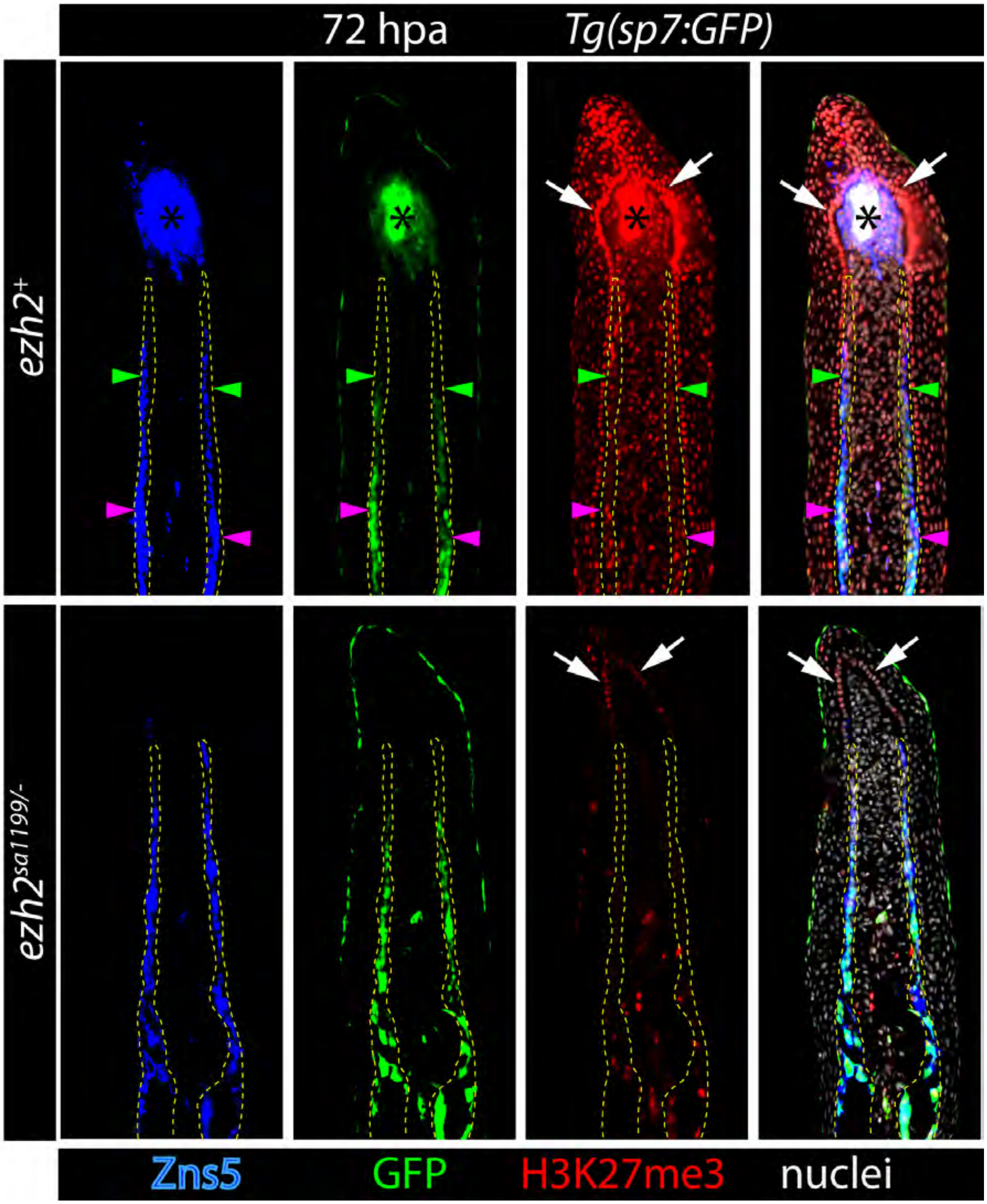
72 hpa
Tg(sp7:GFP)
ezh2⁺
ezh2^sa1199/-^
*
Zns5
GFP
H3K27me3
nuclei

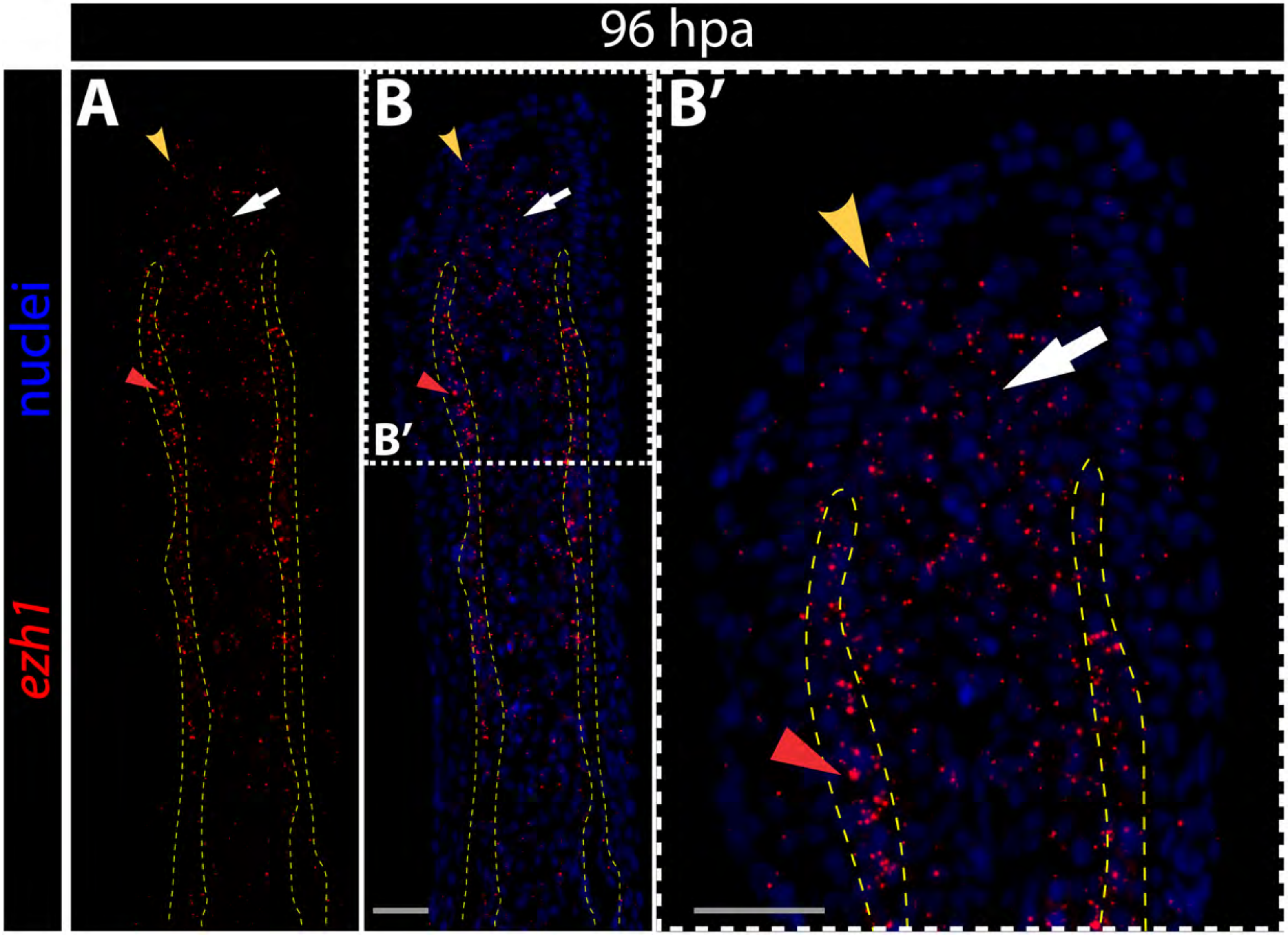
96 hpa
nuclei
ezh1
A
B
B′
B′

Figure S4.2 (previous page). *ezh1* is distally enriched in osteoblasts and distal niche cells. Stacked confocal images a of 96 hpa fin detecting (A) *ezh1* transcripts (red) with RNAscope. Nuclei are in blue. Osteoblasts are outlined in yellow dashed line. Red arrowhead points to distal osteoblasts enriched with *ezh1*. White arrow points to *ezh1* expressing distal niche cells. Basal epidermal cells with low *ezh1* expression are indicated with a yellow arrowhead. (B') White dashed line boxes show magnified distal fin regenerate. Scale bars are 25 μm.

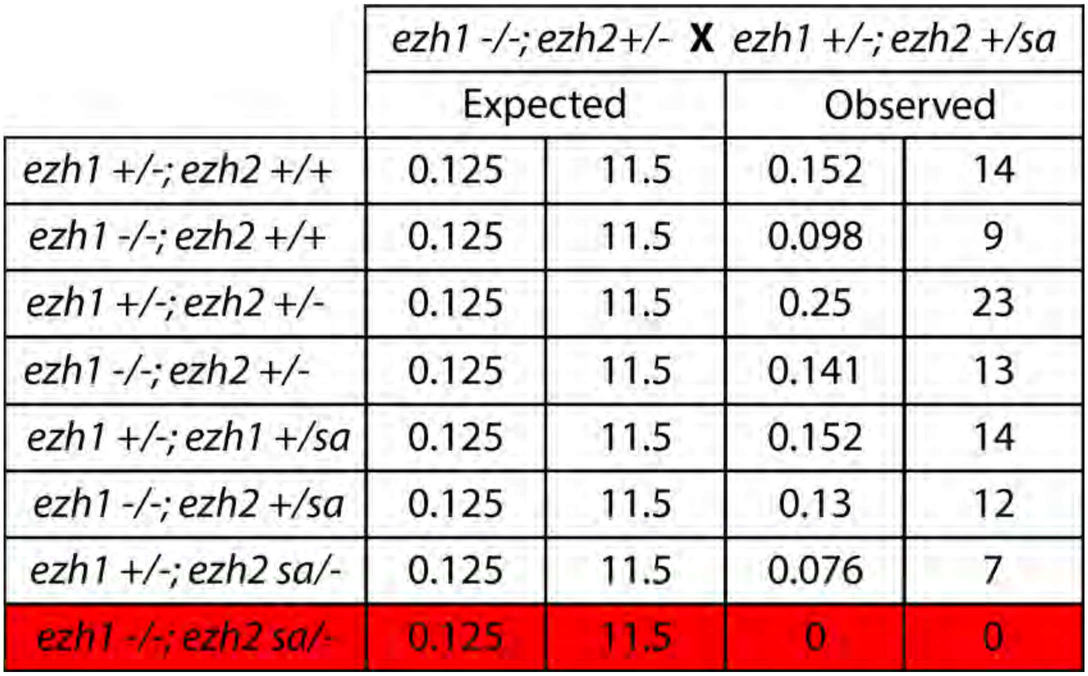

	ezh1 -/-; ezh2+/- **X** *ezh1 +/-; ezh2 +/sa*			
	Expected		Observed	
ezh1 +/-; ezh2 +/+	0.125	11.5	0.152	14
ezh1 -/-; ezh2 +/+	0.125	11.5	0.098	9
ezh1 +/-; ezh2 +/-	0.125	11.5	0.25	23
ezh1 -/-; ezh2 +/-	0.125	11.5	0.141	13
ezh1 +/-; ezh1 +/sa	0.125	11.5	0.152	14
ezh1 -/-; ezh2 +/sa	0.125	11.5	0.13	12
ezh1 +/-; ezh2 sa/-	0.125	11.5	0.076	7
ezh1 -/-; ezh2 sa/-	0.125	11.5	0	0

Table S4.1. *ezh1$^{-/-}$; ezh2$^{sa1199/-}$* fish do not survive to adulthood. Table of expected and observed outcomes from an *ezh1$^{-/-}$; ezh2$^{+/-}$* X *ezh1$^{-/-}$; ezh2$^{+/sa1199}$* breeding. Red highlights unobserved *ezh1$^{-/-}$; ezh2$^{sa1199/-}$* adults, suggesting redundancy between *ezh1* and *ezh2* and that PRC2 was too severely compromised for survival. *sa1199* is abbreviated as "sa".

REFERENCES CITED

Ahmed, A., Wang, T., & Delgado-Olguin, P. (2018). Ezh2 is not required for cardiac regeneration in neonatal mice. *PLOS ONE*, *13*(2), e0192238. https://doi.org/10.1371/journal.pone.0192238

Ai, S., Yu, X., Li, Y., Peng, Y., Li, C., Yue, Y., … He, A. (2017). Divergent Requirements for EZH1 in Heart Development Versus Regeneration. *Circulation Research*, *121*(2), 106–112. https://doi.org/10.1161/CIRCRESAHA.117.311212

Akasaka, T., Kanno, M., Balling, R., Mieza, M. A., Taniguchi, M., & Koseki, H. (1996). A role for mel-18, a Polycomb group-related vertebrate gene, during theanteroposterior specification of the axial skeleton. *Development (Cambridge, England)*, *122*(5), 1513–1522. Retrieved from http://www.ncbi.nlm.nih.gov/pubmed/8625838

Akerberg, A. A., Henner, A., Stewart, S., & Stankunas, K. (2017). Histone demethylases Kdm6ba and Kdm6bb redundantly promote cardiomyocyte proliferation during zebrafish heart ventricle maturation. *Developmental Biology*, *426*(1), 84–96. https://doi.org/10.1016/j.ydbio.2017.03.030

Anders, S., & Huber, W. (2010). Differential expression analysis for sequence count data. *Genome Biology*. https://doi.org/10.1186/gb-2010-11-10-r106

Anders, S., Pyl, P. T., & Huber, W. (2015). HTSeq--a Python framework to work with high-throughput sequencing data. *Bioinformatics (Oxford, England)*, *31*(2), 166–169. https://doi.org/10.1093/bioinformatics/btu638

Ando, K., Shibata, E., Hans, S., Brand, M., & Kawakami, A. (2017). Osteoblast Production by Reserved Progenitor Cells in Zebrafish Bone Regeneration and Maintenance. *Developmental Cell*, *43*(5), 643-650.e3. https://doi.org/10.1016/j.devcel.2017.10.015

Armstrong, B. E., Henner, A., Stewart, S., & Stankunas, K. Shh promotes direct interactions between epidermal cells and osteoblast progenitors to shape regenerated zebrafish bone. , 144 Development § (2017).

Ashburner, M., Ball, C. A., Blake, J. A., Botstein, D., Butler, H., Cherry, J. M., … Sherlock, G. (2000). Gene ontology: Tool for the unification of biology. *Nature Genetics*. https://doi.org/10.1038/75556

Azevedo, A. S., Grotek, B., Jacinto, A., Weidinger, G., & Saúde, L. (2011). The regenerative capacity of the zebrafish caudal fin is not affected by repeated amputations. *PLoS ONE*, *6*(7), e22820. https://doi.org/10.1371/journal.pone.0022820

Bae, W. K., Kang, K., Yu, J. H., Yoo, K. H., Factor, V. M., Kaji, K., … Hennighausen, L. (2015). The methyltransferases enhancer of zeste homolog (EZH) 1 and EZH2 control hepatocyte homeostasis and regeneration. *FASEB Journal : Official Publication of the Federation of American Societies for Experimental Biology, 29*(5), 1653–1662. https://doi.org/10.1096/fj.14-261537

Ben-Yair, R., Butty, V. L., Busby, M., Qiu, Y., Levine, S. S., Goren, A., … Burns, C. E. (2019). H3K27me3-mediated silencing of structural genes is required for zebrafish heart regeneration. *Development*, *146*(19), dev178632. https://doi.org/10.1242/dev.178632

Bernstein, B. E., Mikkelsen, T. S., Xie, X., Kamal, M., Huebert, D. J., Cuff, J., … Lander, E. S. (2006). A bivalent chromatin structure marks key developmental genes in embryonic stem cells. *Cell*, *125*(2), 315–326. https://doi.org/10.1016/j.cell.2006.02.041

Blake, J. A., Dolan, M., Drabkin, H., Hill, D. P., Ni, L., Sitnikov, D., … Westerfield, M. (2013). Gene ontology annotations and resources. *Nucleic Acids Research*. https://doi.org/10.1093/nar/gks1050

Boniface, E. J., Lu, J., Victoroff, T., Zhu, M., & Chen, W. (2009). FlEx-based transgenic reporter lines for visualization of Cre and Flp activity in live zebrafish. *Genesis*. https://doi.org/10.1002/dvg.20526

Brinkley, J. F., Fisher, S., Harris, M. P., Holmes, G., Hooper, J. E., Jabs, E. W., … Chai, Y. (2016). The FaceBase Consortium: a comprehensive resource for craniofacial researchers. *Development (Cambridge, England)*, *143*(14), 2677–2688. https://doi.org/10.1242/dev.135434

Broussonet, M. (1786). Observations sur la regeneration de quelques parties du corps des poissons. *Hist d. l'Acad Roy Des Sciences*, 684–688. Retrieved from http://ci.nii.ac.jp/naid/10027563171/en/

Carbon, S., Ireland, A., Mungall, C. J., Shu, S., Marshall, B., Lewis, S., … Gaudet, P. (2009). AmiGO: Online access to ontology and annotation data. *Bioinformatics*. https://doi.org/10.1093/bioinformatics/btn615

Chacón-Martínez, C. A., Koester, J., & Wickström, S. A. (2018). Signaling in the stem cell niche: Regulating cell fate, function and plasticity. *Development (Cambridge)*. https://doi.org/10.1242/dev165399

Chamberlain, S. J., Yee, D., & Magnuson, T. (2008). Polycomb repressive complex 2 is dispensable for maintenance of embryonic stem cell pluripotency. *Stem Cells (Dayton, Ohio), 26*(6), 1496–1505. https://doi.org/10.1634/stemcells.2008-0102

Chiacchiera, F., Rossi, A., Jammula, S., Zanotti, M., & Pasini, D. (2016). PRC2 preserves intestinal progenitors and restricts secretory lineage commitment. *The EMBO Journal*, *35*(21), 2301–2314. https://doi.org/10.15252/embj.201694550

Chrispijn, N. D., Andralojc, K. M., Castenmiller, C., & Kamminga, L. M. (2018). Gene expression profile of a selection of Polycomb Group genes during zebrafish embryonic and germ line development. *PloS One*, *13*(7), e0200316. https://doi.org/10.1371/journal.pone.0200316

Cloos, P. A. C., Christensen, J., Agger, K., & Helin, K. (2008, May 1). Erasing the methyl mark: Histone demethylases at the center of cellular differentiation and disease. *Genes and Development*, Vol. 22, pp. 1115–1140. https://doi.org/10.1101/gad.1652908

Coré, N., Bel, S., Gaunt, S. J., Aurrand-Lions, M., Pearce, J., Fisher, A., & Djabali, M. (1997). Altered cellular proliferation and mesoderm patterning in Polycomb-M33-deficient mice. *Development (Cambridge, England)*, *124*(3), 721–729. Retrieved from http://www.ncbi.nlm.nih.gov/pubmed/9043087

Courel, M., Friesenhahn, L., & Lees, J. A. (2008). E2f6 and Bmi1 cooperate in axial skeletal development. *Developmental Dynamics : An Official Publication of the American Association of Anatomists*, *237*(5), 1232–1242. https://doi.org/10.1002/dvdy.21516

Crump, J. G., Swartz, M. E., Eberhart, J. K., & Kimmel, C. B. (2006). Moz-dependent Hox expression controls segment-specific fate maps of skeletal precursors in the face. *Development (Cambridge, England)*, *133*(14), 2661–2669. https://doi.org/10.1242/dev.02435

Crump, J. G., Swartz, M. E., & Kimmel, C. B. (2004). An integrin-dependent role of pouch endoderm in hyoid cartilage development. *PLoS Biology*, *2*(9), E244. https://doi.org/10.1371/journal.pbio.0020244

de Both, N. J. (1970). The developmental potencies of the regeneration blastema of the axolotl limb. *Wilhelm Roux' Archiv Für Entwicklungsmechanik Der Organismen*. https://doi.org/10.1007/BF01380787

DeLaurier, A., Eames, B. F., Blanco-Sánchez, B., Peng, G., He, X., Swartz, M. E., … Kimmel, C. B. (2010). Zebrafish sp7:EGFP: a transgenic for studying otic vesicle formation, skeletogenesis, and bone regeneration. *Genesis (New York, N.Y. : 2000)*, *48*(8), 505–511. https://doi.org/10.1002/dvg.20639

Delgado-Olguín, P., Huang, Y., Li, X., Christodoulou, D., Seidman, C. E., Seidman, J. G., … Bruneau, B. G. (2012). Epigenetic repression of cardiac progenitor gene expression by Ezh2 is required for postnatal cardiac homeostasis. *Nature Genetics*, *44*(3), 343–347. https://doi.org/10.1038/ng.1068

Dudakovic, A., Camilleri, E. T., Riester, S. M., Paradise, C. R., Gluscevic, M., O'Toole, T. M., … van Wijnen, A. J. (2016). Enhancer of Zeste Homolog 2 Inhibition Stimulates Bone Formation and Mitigates Bone Loss Caused by Ovariectomy in Skeletally Mature Mice. *The Journal of Biological Chemistry*, *291*(47), 24594–24606. https://doi.org/10.1074/jbc.M116.740571

Dudakovic, A., Camilleri, E. T., Xu, F., Riester, S. M., McGee-Lawrence, M. E., Bradley, E. W., … van Wijnen, A. J. (2015). Epigenetic Control of Skeletal Development by the Histone Methyltransferase Ezh2. *The Journal of Biological Chemistry*, *290*(46), 27604–27617. https://doi.org/10.1074/jbc.M115.672345

Dupret, B., Völkel, P., Le Bourhis, X., & Angrand, P.-O. (2016). The Polycomb Group Protein Pcgf1 Is Dispensable in Zebrafish but Involved in Early Growth and Aging. *PloS One*, *11*(7), e0158700. https://doi.org/10.1371/journal.pone.0158700

Dupret, B., Völkel, P., Vennin, C., Toillon, R.-A. A., Le Bourhis, X., & Angrand, P.-O. O. (2017). The histone lysine methyltransferase Ezh2 is required for maintenance of the intestine integrity and for caudal fin regeneration in zebrafish. *Biochimica et Biophysica Acta. Gene Regulatory Mechanisms*, *1860*(10), 1079–1093. https://doi.org/10.1016/j.bbagrm.2017.08.011

Eames, B. F., DeLaurier, A., Ullmann, B., Huycke, T. R., Nichols, J. T., Dowd, J., … Kimmel, C. B. (2013). FishFace: interactive atlas of zebrafish craniofacial development at cellular resolution. *BMC Developmental Biology*, *13*, 23. https://doi.org/10.1186/1471-213X-13-23

El-Brolosy, M. A., Kontarakis, Z., Rossi, A., Kuenne, C., Günther, S., Fukuda, N., … Stainier, D. Y. R. (2019). Genetic compensation triggered by mutant mRNA degradation. *Nature*, *568*(7751), 193–197. https://doi.org/10.1038/s41586-019-1064-z

El-Brolosy, M. A., & Stainier, D. Y. R. (2017). Genetic compensation: A phenomenon in search of mechanisms. *PLoS Genetics*, *13*(7), e1006780. https://doi.org/10.1371/journal.pgen.1006780

Ertzer, R., Müller, F., Hadzhiev, Y., Rathnam, S., Fischer, N., Rastegar, S., & Strähle, U. (2007). Cooperation of sonic hedgehog enhancers in midline expression. *Developmental Biology*. https://doi.org/10.1016/j.ydbio.2006.11.004

Ezhkova, E., Lien, W.-H., Stokes, N., Pasolli, H. A., Silva, J. M., & Fuchs, E. (2011). EZH1 and EZH2 cogovern histone H3K27 trimethylation and are essential for hair follicle homeostasis and wound repair. *Genes & Development*, *25*(5), 485–498. https://doi.org/10.1101/gad.2019811

Ezhkova, E., Pasolli, H. A., Parker, J. S., Stokes, N., Su, I., Hannon, G., … Fuchs, E. (2009). Ezh2 orchestrates gene expression for the stepwise differentiation of tissue-specific stem cells. *Cell*, *136*(6), 1122–1135. https://doi.org/10.1016/j.cell.2008.12.043

Faust, C., Schumacher, A., Holdener, B., & Magnuson, T. (1995). The eed mutation disrupts anterior mesoderm production in mice. *Development (Cambridge, England)*, *121*(2), 273–285. Retrieved from http://www.ncbi.nlm.nih.gov/pubmed/7768172

Ferguson, J. W., Devarajan, M., & Atit, R. P. (2018). Stage-specific roles of Ezh2 and Retinoic acid signaling ensure calvarial bone lineage commitment. *Developmental Biology*, *443*(2), 173–187. https://doi.org/10.1016/j.ydbio.2018.09.014

Ferrari, K. J., Scelfo, A., Jammula, S., Cuomo, A., Barozzi, I., Stützer, A., … Pasini, D. (2014). Polycomb-dependent H3K27me1 and H3K27me2 regulate active transcription and enhancer fidelity. *Molecular Cell*, *53*(1), 49–62. https://doi.org/10.1016/j.molcel.2013.10.030

Gemberling, M., Bailey, T. J., Hyde, D. R., & Poss, K. D. (2013, November). The zebrafish as a model for complex tissue regeneration. *Trends in Genetics*, Vol. 29, pp. 611–620. https://doi.org/10.1016/j.tig.2013.07.003

Glicksman, M. A., & Brower, D. L. (1988). Misregulation of homeotic gene expression in Drosophila larvae resulting from mutations at the extra sex combs locus. *Developmental Biology*, *126*(2), 219–227. https://doi.org/10.1016/0012-1606(88)90132-7

Gökbuget, D., & Blelloch, R. (2019). Epigenetic control of transcriptional regulation in pluripotency and early differentiation. *Development*, *146*(19), dev164772. https://doi.org/10.1242/dev.164772

Haffter, P., Odenthal, J., Mullins, M. C., Lin, S., Farrell, M. J., Vogelsang, E., … Nüsslein-Volhard, C. (1996). Mutations affecting pigmentation and shape of the adult zebrafish. *Roux's Archives of Developmental Biology*. https://doi.org/10.1007/s004270050051

Hamada, Y., Bando, T., Nakamura, T., Ishimaru, Y., Mito, T., Noji, S., … Ohuchi, H. (2015). Leg regeneration is epigenetically regulated by histone H3K27 methylation in the cricket Gryllus bimaculatus. *Development (Cambridge, England)*, *142*(17), 2916–2927. https://doi.org/10.1242/dev.122598

Isono, K., Fujimura, Y., Shinga, J., Yamaki, M., O-Wang, J., Takihara, Y., … Koseki, H. (2005). Mammalian polyhomeotic homologues Phc2 and Phc1 act in synergy to mediate polycomb repression of Hox genes. *Molecular and Cellular Biology*, *25*(15), 6694–6706. https://doi.org/10.1128/MCB.25.15.6694-6706.2005

Jain, D., Nemec, S., Luxey, M., Gauthier, Y., Bemmo, A., Balsalobre, A., & Drouin, J. (2018). Regulatory integration of Hox factor activity with T-box factors in limb development. *Development (Cambridge, England)*, *145*(6), dev.159830. https://doi.org/10.1242/dev.159830

Katoh-Fukui, Y., Tsuchiya, R., Shiroishi, T., Nakahara, Y., Hashimoto, N., Noguchi, K., & Higashinakagawa, T. (1998). Male-to-female sex reversal in M33 mutant mice. *Nature*, *393*(6686), 688–692. https://doi.org/10.1038/31482

Kawakami, A., Fukazawa, T., & Takeda, H. (2004). Early fin primordia of zebrafish larvae regenerate by a similar growth control mechanism with adult regeneration. *Developmental Dynamics*, *231*(4), 693–699. https://doi.org/10.1002/dvdy.20181

Kettleborough, R. N. W., Busch-Nentwich, E. M., Harvey, S. A., Dooley, C. M., de Bruijn, E., van Eeden, F., … Stemple, D. L. (2013). A systematic genome-wide analysis of zebrafish protein-coding gene function. *Nature*, *496*(7446), 494–497. https://doi.org/10.1038/nature11992

Kim, D., Pertea, G., Trapnell, C., Pimentel, H., Kelley, R., & Salzberg, S. L. (2013). TopHat2: Accurate alignment of transcriptomes in the presence of insertions, deletions and gene fusions. *Genome Biology*, *14*(4), R36. https://doi.org/10.1186/gb-2013-14-4-r36

Knopf, F., Hammond, C., Chekuru, A., Kurth, T., Hans, S., Weber, C. W., … Weidinger, G. (2011). Bone regenerates via dedifferentiation of osteoblasts in the zebrafish fin. *Developmental Cell*. https://doi.org/10.1016/j.devcel.2011.04.014

Knutson, S. K., Warholic, N. M., Wigle, T. J., Klaus, C. R., Allain, C. J., Raimondi, A., … Keilhack, H. (2013). Durable tumor regression in genetically altered malignant rhabdoid tumors by inhibition of methyltransferase EZH2. *Proceedings of the National Academy of Sciences of the United States of America*, *110*(19), 7922–7927. https://doi.org/10.1073/pnas.1303800110

Koppens, M. A. J., Bounova, G., Gargiulo, G., Tanger, E., Janssen, H., Cornelissen-Steijger, P., … van Lohuizen, M. (2016). Deletion of Polycomb Repressive Complex 2 From Mouse Intestine Causes Loss of Stem Cells. *Gastroenterology*, *151*(4), 684-697.e12. https://doi.org/10.1053/j.gastro.2016.06.020

Kragl, M., Knapp, D., Nacu, E., Khattak, S., Maden, M., Epperlein, H. H., & Tanaka, E. M. (2009). Cells keep a memory of their tissue origin during axolotl limb regeneration. *Nature*. https://doi.org/10.1038/nature08152

Lamouille, S., Xu, J., & Derynck, R. (2014). Molecular mechanisms of epithelial-mesenchymal transition. *Nature Reviews. Molecular Cell Biology*, *15*(3), 178–196. https://doi.org/10.1038/nrm3758

Laue, K., Daujat, S., Crump, J. G., Plaster, N., Roehl, H. H., Tübingen 2000 Screen Consortium, … Hammerschmidt, M. (2008). The multidomain protein Brpf1 binds histones and is required for Hox gene expression and segmental identity. *Development (Cambridge, England)*, *135*(11), 1935–1946. https://doi.org/10.1242/dev.017160

Laugesen, A., & Helin, K. (2014). Chromatin repressive complexes in stem cells, development, and cancer. *Cell Stem Cell*, *14*(6), 735–751. https://doi.org/10.1016/j.stem.2014.05.006

Lavarone, E., Barbieri, C. M., & Pasini, D. (2019). Dissecting the role of H3K27 acetylation and methylation in PRC2 mediated control of cellular identity. *Nature Communications*, *10*(1), 1679. https://doi.org/10.1038/s41467-019-09624-w

Lawson, N. D. (2016). Reverse Genetics in Zebrafish: Mutants, Morphants, and Moving Forward. *Trends in Cell Biology*, Vol. 26, pp. 77–79. https://doi.org/10.1016/j.tcb.2015.11.005

Lawson, N. D., & Weinstein, B. M. (2002). In vivo imaging of embryonic vascular development using transgenic zebrafish. *Developmental Biology*, *248*(2), 307–318. https://doi.org/10.1006/dbio.2002.0711

Lee, C.-H., Holder, M., Grau, D., Saldaña-Meyer, R., Yu, J.-R., Ganai, R. A., … Armache, K.-J. (2018). Distinct Stimulatory Mechanisms Regulate the Catalytic Activity of Polycomb Repressive Complex 2. *Molecular Cell*, *70*(3), 435-448.e5. https://doi.org/10.1016/j.molcel.2018.03.019

Lee, C.-H., Yu, J.-R., Kumar, S., Jin, Y., LeRoy, G., Bhanu, N., … Reinberg, D. (2018). Allosteric Activation Dictates PRC2 Activity Independent of Its Recruitment to Chromatin. *Molecular Cell*, *70*(3), 422-434.e6. https://doi.org/10.1016/j.molcel.2018.03.020

Lee, Y., Grill, S., Sanchez, A., Murphy-Ryan, M., & Poss, K. D. (2005). Fgf signaling instructs position-dependent growth rate during zebrafish fin regeneration. *Development*. https://doi.org/10.1242/dev.02101

Lee, Y., Hami, D., De Val, S., Kagermeier-Schenk, B., Wills, A. A., Black, B. L., … Poss, K. D. (2009). Maintenance of blastemal proliferation by functionally diverse epidermis in regenerating zebrafish fins. *Developmental Biology*. https://doi.org/10.1016/j.ydbio.2009.05.545

Lewis, E. B. (1978). A gene complex controlling segmentation in Drosophila. *Nature, 276*(5688), 565–570. https://doi.org/10.1038/276565a0

Lindeman, L. C., Reiner, A. H., Mathavan, S., Aleström, P., & Collas, P. (2010). Tiling histone H3 lysine 4 and 27 methylation in zebrafish using high-density microarrays. *PloS One*, *5*(12), e15651. https://doi.org/10.1371/journal.pone.0015651

Lui, J. C., Garrison, P., Nguyen, Q., Ad, M., Keembiyehetty, C., Chen, W., … Baron, J. (2016). EZH1 and EZH2 promote skeletal growth by repressing inhibitors of chondrocyte proliferation and hypertrophy. *Nature Communications*, *7*, 13685. https://doi.org/10.1038/ncomms13685

Maderspacher, F., & Nüsslein-Volhard, C. (2003). Formation of the adult pigment pattern in zebrafish requires leopard and obelix dependent cell interactions. *Development*. https://doi.org/10.1242/dev.00519

Mardon, G., Solomon, N. M., & Rubin, G. M. (1994). dachshund encodes a nuclear protein required for normal eye and leg development in Drosophila. *Development*.

Margueron, Raphael, Li, G., Sarma, K., Blais, A., Zavadil, J., Woodcock, C. L., … Reinberg, D. (2008). Ezh1 and Ezh2 Maintain Repressive Chromatin through Different Mechanisms. *Molecular Cell*, *32*(4), 503–518. https://doi.org/10.1016/j.molcel.2008.11.004

Margueron, Raphaël, & Reinberg, D. (2011). The Polycomb complex PRC2 and its mark in life. *Nature*, *469*(7330), 343–349. https://doi.org/10.1038/nature09784

McCusker, C. D., Diaz-Castillo, C., Sosnik, J., Q. Phan, A., & Gardiner, D. M. (2016). Cartilage and bone cells do not participate in skeletal regeneration in Ambystoma mexicanum limbs. *Developmental Biology*. https://doi.org/10.1016/j.ydbio.2016.05.032

McLaughlin, K. A., & Levin, M. (2018). Bioelectric signaling in regeneration: Mechanisms of ionic controls of growth and form. *Developmental Biology*. https://doi.org/10.1016/j.ydbio.2017.08.032

Minguillon, C., Nishimoto, S., Wood, S., Vendrell, E., Gibson-Brown, J. J., & Logan, M. P. O. (2012). Hox genes regulate the onset of Tbx5 expression in the forelimb. *Development (Cambridge, England)*, *139*(17), 3180–3188. https://doi.org/10.1242/dev.084814

Minoux, M., Holwerda, S., Vitobello, A., Kitazawa, T., Kohler, H., Stadler, M. B., & Rijli, F. M. (2017). Gene bivalency at Polycomb domains regulates cranial neural crest positional identity. *Science (New York, N.Y.)*, *355*(6332), eaal2913. https://doi.org/10.1126/science.aal2913

Mirzamohammadi, F., Papaioannou, G., Inloes, J. B., Rankin, E. B., Xie, H., Schipani, E., … Kobayashi, T. (2016). Polycomb repressive complex 2 regulates skeletal growth by suppressing Wnt and TGF-β signalling. *Nature Communications*, *7*(1), 12047. https://doi.org/10.1038/ncomms12047

Mohammadi, M., Froum, S., Hamby, J. M., Schroeder, M. C., Panek, R. L., Lu, G. H., … Hubbard, S. R. (1998). Crystal structure of an angiogenesis inhibitor bound to the FGF receptor tyrosine kinase domain. *EMBO Journal*. https://doi.org/10.1093/emboj/17.20.5896

Montgomery, N. D., Yee, D., Chen, A., Kalantry, S., Chamberlain, S. J., Otte, A. P., & Magnuson, T. (2005). The murine polycomb group protein Eed is required for global histone H3 lysine-27 methylation. *Current Biology : CB*, *15*(10), 942–947. https://doi.org/10.1016/j.cub.2005.04.051

Morgan, T. H. (1900). Regeneration in teleosts. *Archiv Für Entwicklungsmechanik Der Organismen*. https://doi.org/10.1007/BF02156348

Morrison, S. J., & Spradling, A. C. (2008). Stem Cells and Niches: Mechanisms That Promote Stem Cell Maintenance throughout Life. *Cell*, *132*(4), 598–611. https://doi.org/10.1016/j.cell.2008.01.038

Murphy, P. J., Wu, S. F., James, C. R., Wike, C. L., & Cairns, B. R. (2018). Placeholder Nucleosomes Underlie Germline-to-Embryo DNA Methylation Reprogramming. *Cell*, *172*(5), 993-1006.e13. https://doi.org/10.1016/j.cell.2018.01.022

NABRIT, S. M. (1929). THE RÔLE OF THE FIN RAYS IN THE REGENERATION IN THE TAIL-FINS OF FISHES. *The Biological Bulletin*, *56*(4), 235–266. https://doi.org/10.2307/1536898

Nachtrab, G., Kikuchi, K., Tornini, V. A., & Poss, K. D. (2013). Transcriptional components of anteroposterior positional information during zebrafish fin regeneration. *Development (Cambridge)*. https://doi.org/10.1242/dev.098798

Nacu, E., Glausch, M., Le, H. Q., Damanik, F. F. R., Schuez, M., Knapp, D., … Tanaka, E. M. (2013). Connective tissue cells, but not muscle cells, are involved in establishing the proximo-distal outcome of limb regeneration in the axolotl. *Development (Cambridge)*. https://doi.org/10.1242/dev.081752

Nakamura, T., Gehrke, A. R., Lemberg, J., Szymaszek, J., & Shubin, N. H. (2016). Digits and fin rays share common developmental histories. *Nature*, *537*(7619), 225–228. https://doi.org/10.1038/nature19322

Naruse, C., Shibata, S., Tamura, M., Kawaguchi, T., Abe, K., Sugihara, K., … Asano, M. (2017). New insights into the role of Jmjd3 and Utx in axial skeletal formation in mice. *FASEB Journal : Official Publication of the Federation of American Societies for Experimental Biology*, *31*(6), 2252–2266. https://doi.org/10.1096/fj.201600642R

Nechiporuk, A., & Keating, M. T. (2002). A proliferation gradient between proximal and msxb-expressing distal blastema directs zebrafish fin regeneration. *Development*.

Nichols, J. T., Pan, L., Moens, C. B., & Kimmel, C. B. (2013). barx1 represses joints and promotes cartilage in the craniofacial skeleton. *Development (Cambridge, England)*, *140*(13), 2765–2775. https://doi.org/10.1242/dev.090639

O'Carroll, D., Erhardt, S., Pagani, M., Barton, S. C., Surani, M. A., & Jenuwein, T. (2001). The polycomb-group gene Ezh2 is required for early mouse development. *Molecular and Cellular Biology*, *21*(13), 4330–4336. https://doi.org/10.1128/MCB.21.13.4330-4336.2001

Pasini, D., Bracken, A. P., Hansen, J. B., Capillo, M., & Helin, K. (2007). The polycomb group protein Suz12 is required for embryonic stem cell differentiation. *Molecular and Cellular Biology*, *27*(10), 3769–3779. https://doi.org/10.1128/MCB.01432-06

Pasini, D., Bracken, A. P., Jensen, M. R., Lazzerini Denchi, E., & Helin, K. (2004). Suz12 is essential for mouse development and for EZH2 histone methyltransferase activity. *The EMBO Journal*, *23*(20), 4061–4071. https://doi.org/10.1038/sj.emboj.7600402

Paw, B. H., & Zon, L. I. (1999). Primary fibroblast cell culture. *Methods in Cell Biology*, *59*, 39–43. https://doi.org/10.1016/s0091-679x(08)61819-1

Poss, K. D., Shen, J., Nechiporuk, A., McMahon, G., Thisse, B., Thisse, C., & Keating, M. T. (2000). Roles for Fgf signaling during zebrafish fin regeneration. *Developmental Biology*. https://doi.org/10.1006/dbio.2000.9722

Proffitt, K. D., Madan, B., Ke, Z., Pendharkar, V., Ding, L., Lee, M. A., … Virshup, D. M. (2013). Pharmacological inhibition of the Wnt acyltransferase PORCN prevents growth of WNT-driven mammary cancer. *Cancer Research*. https://doi.org/10.1158/0008-5472.CAN-12-2258

Rabinowitz, J. S., Robitaille, A. M., Wang, Y., Ray, C. A., Thummel, R., Gu, H., … Moon, R. T. (2017). Transcriptomic, proteomic, and metabolomic landscape of positional memory in the caudal fin of zebrafish. *Proceedings of the National Academy of Sciences of the United States of America*. https://doi.org/10.1073/pnas.1620755114

Rolland-Lagan, A. G., Paquette, M., Tweedle, V., & Akimenko, M. A. (2012). Morphogen-based simulation model of ray growth and joint patterning during fin development and regeneration. *Development*. https://doi.org/10.1242/dev.073452

Rossi, A., Kontarakis, Z., Gerri, C., Nolte, H., Hölper, S., Krüger, M., & Stainier, D. Y. R. (2015). Genetic compensation induced by deleterious mutations but not gene knockdowns. *Nature*, *524*(7564), 230–233. https://doi.org/10.1038/nature14580

Rougeot, J., Chrispijn, N. D., Aben, M., Elurbe, D. M., Andralojc, K. M., Murphy, P. J., … Kamminga, L. M. (2019). Maintenance of spatial gene expression by Polycomb-mediated repression after formation of a vertebrate body plan. *Development*, *146*(19), dev178590. https://doi.org/10.1242/dev.178590

San, B., Aben, M., Elurbe, D. M., Voeltzke, K., den Broeder, M. J., Rougeot, J., … Kamminga, L. M. (2018). Genetic and epigenetic regulation of zebrafish intestinal development. *Epigenomes*, *2*(4), 19. https://doi.org/10.3390/epigenomes2040019

San, B., Chrispijn, N. D., Wittkopp, N., van Heeringen, S. J., Lagendijk, A. K., Aben, M., … Kamminga, L. M. (2016). Normal formation of a vertebrate body plan and loss of tissue maintenance in the absence of ezh2. *Scientific Reports*, *6*(1), 24658. https://doi.org/10.1038/srep24658

San, B., Rougeot, J., Voeltzke, K., van Vegchel, G., Aben, M., Andralojc, K. M., … Kamminga, L. M. (2019). The ezh2(sa1199) mutant zebrafish display no distinct phenotype. *PloS One*, *14*(1), e0210217. https://doi.org/10.1371/journal.pone.0210217

Scelfo, A., Piunti, A., & Pasini, D. (2015). The controversial role of the Polycomb group proteins in transcription and cancer: how much do we not understand Polycomb proteins? *The FEBS Journal*, *282*(9), 1703–1722. https://doi.org/10.1111/febs.13112

Schwarz, D., Varum, S., Zemke, M., Schöler, A., Baggiolini, A., Draganova, K., … Sommer, L. (2014). Ezh2 is required for neural crest-derived cartilage and bone formation. *Development (Cambridge, England)*, *141*(4), 867–877. https://doi.org/10.1242/dev.094342

Shen, W., & Mardon, G. (1997). Ectopic eye development in Drosophila induced by directed dachshund expression. *Development*.

Shen, X., Liu, Y., Hsu, Y.-J., Fujiwara, Y., Kim, J., Mao, X., … Orkin, S. H. (2008). EZH1 mediates methylation on histone H3 lysine 27 and complements EZH2 in maintaining stem cell identity and executing pluripotency. *Molecular Cell*, *32*(4), 491–502. https://doi.org/10.1016/j.molcel.2008.10.016

Shibata, E., Yokota, Y., Horita, N., Kudo, A., Abe, G., Kawakami, K., & Kawakami, A. (2016). Fgf signalling controls diverse aspects of fin regeneration. *Development (Cambridge)*. https://doi.org/10.1242/dev.140699

Shumacher, A., Faust, C., & Magnuson, T. (1996). Positional cloning of a global regulator of anterior-posterior patterning in mice. *Nature*, *383*(6597), 250–253. https://doi.org/10.1038/383250a0

Slifer, E. H. (1942). A mutant stock of Drosophila with extra sex-combs. *Journal of Experimental Zoology*, *90*(1), 31–40. https://doi.org/10.1002/jez.1400900103

Smith, A., Zhang, J., Guay, D., Quint, E., Johnson, A., & Akimenko, M. A. (2008). Gene expression analysis on sections of zebrafish regenerating fins reveals limitations in the whole-mount in situ hybridization method. *Developmental Dynamics*. https://doi.org/10.1002/dvdy.21417

Snitow, M. E., Li, S., Morley, M. P., Rathi, K., Lu, M. M., Kadzik, R. S., … Morrisey, E. E. (2015). Ezh2 represses the basal cell lineage during lung endoderm development. *Development (Cambridge, England)*, *142*(1), 108–117. https://doi.org/10.1242/dev.116947

Sousa, S., Afonso, N., Bensimon-Brito, A., Fonseca, M., Simões, M., Leon, J., … Jacinto, A. (2011). Differentiated skeletal cells contribute to blastema formation during zebrafish fin regeneration. *Development*. https://doi.org/10.1242/dev.064717

Stewart, S., Gomez, A. W., Armstrong, B. E., Henner, A., & Stankunas, K. (2014). Sequential and opposing activities of Wnt and BMP coordinate zebrafish bone regeneration. *Cell Reports*, *6*(3), 482–498. https://doi.org/10.1016/j.celrep.2014.01.010

Stewart, S., Le Bleu, H. K., Yette, G. A., Henner, A. L., Braunstein, J. A., Stankunas, K., … Stankunas, K. (2019). longfin causes cis-ectopic expression of the kcnh2a ether-a-go-go K+ channel to autonomously prolong fin outgrowth. *BioRxiv*, 790329. https://doi.org/10.1101/790329

Stewart, S., & Stankunas, K. (2012). Limited dedifferentiation provides replacement tissue during zebrafish fin regeneration. *Developmental Biology*, *365*(2), 339–349. https://doi.org/10.1016/j.ydbio.2012.02.031

Stewart, S., Tsun, Z. Y. Z.-Y., & Belmonte, J. C. I. (2009). A histone demethylase is necessary for regeneration in zebrafish. *Proceedings of the National Academy of Sciences of the United States of America*, *106*(47), 19889–19894. https://doi.org/10.1073/pnas.0904132106

Stoick-Cooper, C. L., Weidinger, G., Riehle, K. J., Hubbert, C., Major, M. B., Fausto, N., & Moon, R. T. (2007). Distinct Wnt signaling pathways have opposing roles in appendage regeneration. *Development*. https://doi.org/10.1242/dev.001123

Sun, X.-J., Xu, P.-F., Zhou, T., Hu, M., Fu, C.-T., Zhang, Y., … Chen, Z. (2008). Genome-wide survey and developmental expression mapping of zebrafish SET domain-containing genes. *PloS One*, *3*(1), e1499. https://doi.org/10.1371/journal.pone.0001499

Suzuki, M., Mizutani-Koseki, Y., Fujimura, Y.-I., Miyagishima, H., Kaneko, T., Takada, Y., … Koseki, H. (2002). Involvement of the Polycomb-group gene Ring1B in the specification of the anterior-posterior axis in mice. *Development (Cambridge, England)*, *129*(18), 4171–4183. Retrieved from http://www.ncbi.nlm.nih.gov/pubmed/12183370

Tien, C.-L. C.-L., Jones, A., Wang, H., Gerigk, M., Nozell, S., & Chang, C. (2015). Snail2/Slug cooperates with Polycomb repressive complex 2 (PRC2) to regulate neural crest development. *Development*, *142*(4), 722–731. https://doi.org/10.1242/dev.111997

Tornini, V. A., Puliafito, A., Slota, L. A., Thompson, J. D., Nachtrab, G., Kaushik, A. L., … Poss, K. D. (2016). Live Monitoring of Blastemal Cell Contributions during Appendage Regeneration. *Current Biology*. https://doi.org/10.1016/j.cub.2016.08.072

Tornini, V. A., Thompson, J. D., Allen, R. L., & Poss, K. D. (2017). Live fate-mapping of joint-associated fibroblasts visualizes expansion of cell contributions during zebrafish fin regeneration. *Development (Cambridge)*. https://doi.org/10.1242/dev.155655

Tu, S., & Johnson, S. L. (2011). Fate restriction in the growing and regenerating zebrafish fin. *Developmental Cell*. https://doi.org/10.1016/j.devcel.2011.04.013

van der Lugt, N. M., Domen, J., Linders, K., van Roon, M., Robanus-Maandag, E., te Riele, H., … van Lohuizen, M. (1994). Posterior transformation, neurological abnormalities, and severe hematopoietic defects in mice with a targeted deletion of the bmi-1 proto-oncogene. *Genes & Development*, *8*(7), 757–769. https://doi.org/10.1101/gad.8.7.757

van der Velden, Y. U., Wang, L., van Lohuizen, M., & Haramis, A.-P. G. (2012). The Polycomb group protein Ring1b is essential for pectoral fin development. *Development (Cambridge, England)*, *139*(12), 2210–2220. https://doi.org/10.1242/dev.077156 van Eeden, F. J., Granato, M., Schach, U., Brand, M., Furutani-Seiki, M., Haffter, P., … Nüsslein-Volhard, C. (1996). Genetic analysis of fin formation in the zebrafish, Danio rerio. *Development (Cambridge, England)*, *123*(1), 255–262. Retrieved from http://www.ncbi.nlm.nih.gov/pubmed/9007245

Vastenhouw, N. L., Zhang, Y., Woods, I. G., Imam, F., Regev, A., Liu, X. S., … Schier, A. F. (2010). Chromatin signature of embryonic pluripotency is established during genome activation. *Nature*, *464*(7290), 922–926. https://doi.org/10.1038/nature08866

Völkel, P., Bary, A., Raby, L., Chapart, A., Dupret, B., Le Bourhis, X., & Angrand, P.-O. (2019). Ezh1 arises from Ezh2 gene duplication but its function is not required for zebrafish development. *Scientific Reports*, *9*(1), 4319. https://doi.org/10.1038/s41598-019-40738-9

Walker, M. B., & Kimmel, C. B. (2007). A two-color acid-free cartilage and bone stain for zebrafish larvae. *Biotechnic & Histochemistry : Official Publication of the Biological Stain Commission*, *82*(1), 23–28. https://doi.org/10.1080/10520290701333558

Wehner, D., Cizelsky, W., Vasudevaro, M. D., Ozhan, G., Haase, C., Kagermeier-Schenk, B., … Weidinger, G. (2014). Wnt/β-catenin signaling defines organizing centers that orchestrate growth and differentiation of the regenerating zebrafish caudal fin. *Cell Reports*, *6*(3), 467–481. https://doi.org/10.1016/j.celrep.2013.12.036

Wehner, D., & Weidinger, G. (2015). Signaling networks organizing regenerative growth of the zebrafish fin. *Trends in Genetics*. https://doi.org/10.1016/j.tig.2015.03.012

Whitcomb, S. J., Basu, A., Allis, C. D., & Bernstein, E. (2007). Polycomb Group proteins: an evolutionary perspective. *Trends in Genetics : TIG*, *23*(10), 494–502. https://doi.org/10.1016/j.tig.2007.08.006

White, R. J., Collins, J. E., Sealy, I. M., Wali, N., Dooley, C. M., Digby, Z., … Busch-Nentwich, E. M. (2017). A high-resolution mRNA expression time course of embryonic development in zebrafish. *ELife*, *6*, e30860. https://doi.org/10.7554/eLife.30860

Williams, J. S., Hsu, J. Y., Rossi, C. C., & Artinger, K. B. (2018). Requirement of zebrafish pcdh10a and pcdh10b in melanocyte precursor migration. *Developmental Biology*, *444 Suppl*, S274–S286. https://doi.org/10.1016/j.ydbio.2018.03.022

Wolpert, L. (2016). Positional Information and Pattern Formation. In *Current Topics in Developmental Biology*. https://doi.org/10.1016/bs.ctdb.2015.11.008

Yamashita, Y. M., & Tumbar, T. (2014). Stem cells and their niche in homeostasis/regeneration and disease. *Molecular Biology of the Cell*. https://doi.org/10.1091/mbc.E13-11-0674

Yu, J.-R., Lee, C.-H., Oksuz, O., Stafford, J. M., & Reinberg, D. (2019). PRC2 is high maintenance. *Genes & Development*, *33*(15–16), 903–935. https://doi.org/10.1101/gad.325050.119

Zhang, Y., Vastenhouw, N. L., Feng, J., Fu, K., Wang, C., Ge, Y., … Liu, X. S. (2014). Canonical nucleosome organization at promoters forms during genome activation. *Genome Research*, *24*(2), 260–266. https://doi.org/10.1101/gr.157750.113

Zhong, Y., Ye, Q., Chen, C., Wang, M., & Wang, H. (2018). Ezh2 promotes clock function and hematopoiesis independent of histone methyltransferase activity in zebrafish. *Nucleic Acids Research*, *46*(7), 3382–3399. https://doi.org/10.1093/nar/gky101